10-25-2019 2:00 PM

Effect of Ion Implantation on the Mechanical Properties of the Grain and Grain Boundary Regions of Inconel X750

Maisaa Nezar Tawfeeq
The University of Western Ontario

Supervisor
Prof. Robert J. Klassen
The University of Western Ontario

Graduate Program in Mechanical and Materials Engineering
A thesis submitted in partial fulfillment of the requirements for the degree in Doctor of Philosophy

Recommended Citation

Tawfeeq, Maisaa Nezar, "Effect of Ion Implantation on the Mechanical Properties of the Grain and Grain Boundary Regions of Inconel X750" (2019). *Electronic Thesis and Dissertation Repository*. 6676.
https://ir.lib.uwo.ca/etd/6676

Abstract

Annulus gas spacers in CANada Deuterium Uranium (CANDU) nuclear reactors are made from the heat-treated Inconel X750 Nickel-based alloy. This alloy is designed to have high strength and creep resistance at elevated temperature. Unlike other reactor designs, the CANDU reactor has a high thermal neutron fluence, which results in an enhancement of the radiation damage and the internal production of helium and hydrogen. They are thus susceptible to microstructural instability and mechanical property degradation with time. Studies of ex-service spacers have indicated that they display intergranular embrittlement and lower ultimate tensile strength compared to nonirradiated Inconel X750. The primary degradation mechanism remains unclear, and thus provides the focus of the current investigation. Sole and sequential Ni^+ and He^+ ion irradiation, up to different doses and irradiation temperature, was used to simulate neutron irradiation and to explore the microstructural evolution and mechanical property degradation in X750. The discussion of the microstructural evolution is focused on the irradiation-induced defect clusters, formation of helium bubbles and the stability of strengthening precipitates γ'. Utilizing of focused ion beam (FIB) and transmission electron microscopy (TEM) to perform high resolution microstructure characterization was a major contribution of this work. The microstructure is correlated to the mechanical properties measured through nanoindentation hardness test on irradiated and nonirradiated material. Established theories were applied to assess the contribution of ion-induced defect clustering, γ' precipitate disordering state, and helium bubble accumulation to the hardness of the X750 alloy and was compared to the nanoindentation hardness results. This approach is unique to the literature since it demonstrates both the individual and the combined effects of the microstructural features on mechanical behavior. Furthermore, a novel approach was curried out to determine the effect of the misorientation angle, irradiation-induced crystallographic damage, and accumulated helium on the strength of a grain boundary in Inconel X750. Bending of notched cantilever micro-beams X750 in the nonirradiated condition and after irradiation with high energy Ni^+ and He^+ ions was implemented. Bending test results suggests that the grain boundary strength of X750 alloy is related to the grain boundary energy and decreases as the energy increases. Dispersed barrier hardening model along with Finite Element (FE) model were applied to analyze the bending test finding.

Keywords

Nickel superalloy, heavy ion irradiation, helium implantation, nanoindentation Hardness, micro-cantilever beam bending, grain boundary strength, sequential irradiation.

Summary for Lay Audience

Inconel X750 Nickel based super alloy is used in the core of CANDU (Canadian Deuterium Uranium) reactors as a fuel channel spacer (garter springs) to separate the hot pressure tube and the cold calandria tube. This alloy is mainly strengthened by a coherent precipitate know as γ'. Recently, it has been found that the spacers became very brittle after long exposure to neutron radiation and the embrittlement is characterized as intergranular failure. The current research involves nanoindentation hardness testing and micro-cantilever bending testing to assess the effects of irradiation on the hardening and onset of grain boundary embrittlement in the Inconel X750 spring spacers. The experiments are designed in such way to enable us to simulate the working condition of a CANDU reactor. The samples were irradiated solely and sequentially with heavy ions (Ni^+) to emulate neutron irradiation, and with helium ions (He^+) to simulate the helium produced from the transmutation reaction within the X750. The implantation was carried out at two temperatures 25°C and 200°C, to study the effect of implantation temperature on the mechanical properties of X750. Results show that low dose of sole implanted Ni^+ soften the alloy because of disordering the strengthening phase γ', as observed by Transmission Electron Microscopy (TEM). In contrast, He^+ implantation harden the material because of Helium babble formation. This observation was true for both implantation temperature. Sequential He^+/Ni^+ implantation results show that the softening and hardening mechanisms are operating in parallel and their effects are additive. To measure the grain boundary strength in irradiated and non-irradiated condition, a novel notched micro-cantilever beam bending test was performed. The cantilever micro-beams were notched along grain boundaries. Results show that He^+ implanted samples have the highest yield strength in compare to Ni^+ implanted and nonimplanted counterparts. Therefore, the intergranular embrittlement observed in the spacer alloy was attributed to the accumulation of helium bubbles in the grain boundaries. The obtained data will be beneficial to the operators of CANDU reactors since they will allow better life predictions to be made for existing spacers and will also be helpful for the design of the future nuclear reactors.

Co-Authorship Statement

This thesis in presented in integrated article format. Each chapter is based on the following published or submitted to journal articles:

Chapter 3:

Maisaa N. Tawfeeq, Robert J. Klassen "Ni^+ and He^+ Implantation Effects on the Hardness and Microstructure of Heat Treated Inconel X750", submitted to Journal of Nuclear Engineering and Radiation Science, August 2019.

Chapter 4:

Maisaa N. Tawfeeq, Robert J. Klassen, "Effect of sequential helium and nickel ion implantation on the nano-indentation hardness of Inconel X750", submitted to Journal of Nuclear Engineering and Radiation Science, August 2019.

Chapter 5:

Maisaa N. Tawfeeq, Robert J. Klassen, "Effect of ion implantation on the grain boundary strength of heat-treated Inconel X750", Journal of Nuclear Materials, Vol. 516, pp255-263, 2019.

In all above mentioned chapters, ion implantations of the Inconel X750 samples was performed by the assistance of Mr. Jack Hendriks at the Tandetron Ion Accelerator facilities at the University of Western Ontario. In chapter 4 and 5, TEM foils were prepared by Dr. T. Simpson of the University of Western Ontario Nanofabrication Laboratory, and TEM was used by the assistance of Dr. Carmen Andrei in Canadian Centre for Electron Microscopy- McMaster.

The experiments were designed and executed by Maisaa N. Tawfeeq. Also, data analysis, interpretation and writing the initial drafts of the manuscripts were performed by the candidate. Further data interpretation and editing of the manuscript were performed by Dr. Robert J. Klassen.

Acknowledgements

The work presented in this thesis would not have been possible without the help and cooperation of the people I would like to acknowledge here.

First of all, I am most grateful to my supervisor Professor Robert J. Klassen for his continuous guidance, support, motivation and ideas provided throughout my Ph.D. study at Western. Without his help, the successful competition of this thesis and the quality of work achieved would not have been possible. Professor Klassen is a great scientist as well as a great person, working under his supervision was such a great honor. I have learned more than knowledge from him in the past five years, his advice guided me not only in my research but also in my decision for my future life.

I would like to thank my past and present colleagues whom I worked with at our Nano Mechanical testing laboratory for their support, especially Dr. Vineet Bhakhri, Dr. Ariful Islam, Imran Khan, Aria Khalili, Feifei Nie, Heygaan Rajakumar and Mahdi Bagheripoor.

Special notes of thanks are due to Prof. Jeffrey Wood for allowing me using the optical microscopy in his laboratory, Dr. Todd Simpson of Western University's Nanofabrication Laboratory for preparing the TEM foils, Dr. Carmen Andrei and Mr. Chris Butcher from Canadian Centre for Electron Microscopy, McMaster University for helping me with the transmission electron microscopy (TEM) and electron back scattered diffraction (EBSD), Mr. Jack Hendrix of Western University's ion implantation facility for sample irradiation, Mr. Brad Knobe and Mr. Gary Good of Surface Science Western for helping me using their Secondary Ion Mass Spectrometry (SIMS) and scanning Electron Microscopy (SEM). Also, I sincerely thank many wonderful people in MME department, specially Ms. Joanna Blom for her kindness and advice.

I wish to thank the Natural Science and Engineering Research Council of Canada (NSERC), the University Network of Excellence in Nuclear Engineering (UNENE) and Ontario Graduate Scholarship (OGS) program who provided financial support for this research.

Last but not least, I express my gratitude to my friends and family for all the love, support, encouragement and prayers they have sent my way along this journey. To my parents, thank you for being my champions throughout my entire life. Your unconditional love and support have meant the world to me, I hope that I have made you proud. To my little girls, Lina and Ola, thank you for the patience you have shown during the past five years, you are my inspiration to achieve greatness. Without you, I would not be where I am today.

To My Beloved Parents and Daughters

List of Contents

List of Tables

List of Figures

List of Abbreviations

Abbreviations	**Definition**
APB	Antiphase Boundary
CANDU	Canadian Deuterium Uranium Reactor
CSL	Coincidental Site Lattice
dpa	Displacement per atom
EBSD	Electron Back Scattered Diffraction
EDX	Energy dispersive X-ray
FCC	Face Centered Cubic
FE	Finite Element
FIB	Focus Ion Beam
HT	Heat Treated
ISE	Indentation Size Effect
K-P	Kinchin-Pease
MD	Molecular Dynamics
NRT	Norgett-Robinson-Torrens
PKA	Primary Knock on Atom
SA	Solution Annealed
SEM	Scanning Electron Microscope
SFT	Stacking Fault Tetrahedron
SRIM	Stopping Range of Ions in Matter software
TEM	Transmission Electron Microscope
VDZ	Void Denoted Zones

List of Symbols

Symbols	**Definition**
T_{melt}	Melting temperature
E_d	Threshold displacement energy
E_c	Energy loss by electron stopping
T	PKA energy
T_{max}	Maximum PKA energy
E_k	Kinetic energy
Λ	Mass ratio
m	Mass of incident particle
M	Mass of stationary atom
θ_s	Scattering angle in a collision system
ν_d	Number of displaced atoms
T_{dam}	Energy dissipated in elastic collisions
ϕ	Ion fluence
D	Damage rate is in vacancy/ion/Å
N	Atomic density
θ	Misorientation angle
$\varphi_1, \Phi,\ \varphi_2$	Euler angles
g_i	Rotation matrix
M_{ij}	Misorientation rotation matrix
Σ	The degree of CSL
S^{GB}	Grain boundary sink strength

Symbols	**Definition**
H	Indentation hardness
σ_y	Yield stress
σ_c	Fracture stress
a	Crack length
ψ	Irradiation damage
C_{He}	Helium concentration
K	Mixing parameter
$\mathrm{D}_{\mathrm{mix}}$	Intermixing diffusion coefficient
T_{imp}	Implantation temperature
h	Indentation depth
h*	Characteristic depth
α	Obstacles strength
M	Taylor factor
b	Burger vector
μ	Elastic shear modulus
γ_{APB}	Antiphase boundary energy
ε	Elastic coherency strain
$\sigma_{y_{GB}}$	Grain boundary yield stress
ρ_d	Defect density
E_R	Reduced elastic modulus
E	Elastic modulus

Chapter 1

1 Introduction

1.1 Nickel-based super alloy in the reactor core

Nickel forms the main alloying element of a large class of materials called nickel-based superalloys. These superalloys have good mechanical strength and excellent creep and oxidation resistance properties at high temperatures [1]. Therefore, they are widely used in a variety of industrial applications including nuclear were they are used in in-core fasteners (bolts), spacers, and springs [2]. Exposure to neutrons can result in microstructural changes to Ni-based superalloys by two mechanisms; 1) neutron-induced atomic displacement, which causes the metal to become hardened and to lose ductility, and 2) neutron-induced helium accumulation via the $^{58}Ni(n,\gamma)^{56}Fe$ transmutation process, which causes the metal to become embrittled especially at the grain boundaries. The microstructural processes that affect irradiation hardening, and grain boundary embrittlement are of great interest to Canadian nuclear industry in that they affect the life expectancy of key Ni-alloy components found in CANDU nuclear reactors namely those made from the heat treated Inconel X750 superalloy.

1.2 Inconel X750 spacers in the CANDU reactor

The core of Canadian deuterium Uranium Reactor (CANDU) contains around four hundred horizontal fuel channels arranged inside a large cylindrical steel calandria vessel. Each fuel channel contains a hot pressure tube (operating at 260°C -310°C) surrounded by an insulating gas gap (CO_2) that separates it from a cold calandria tube (operating at 60°C to 70°C). Both tubes are made from zirconium alloys [3]. Helical garter spring spacers, made from the Ni-based Inconel X750 alloy, are stretched around the pressure tube at four locations along the tube to prevent it from touching the calandria tube (Figure 1.1). Contact between the tubes would lower the efficiency of the reactor by allowing heat transfer from the hot pressure tube to the cold calandria tube and may result in a safety issue involving hydride formation and cracking of the pressure tube.

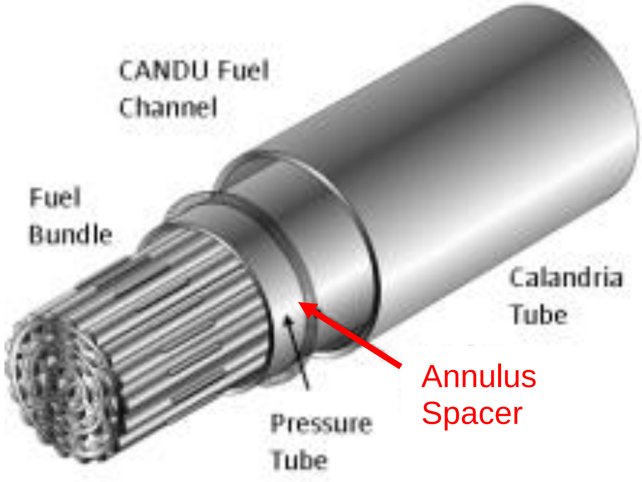

Figure 1.1: CANDU fuel channel with Inconel X-750 spacer coil highlighted [13]

1.3 Motivation

Examination of spacers removed from CANDU reactors have indicated that they exhibit embrittlement, and lower ultimate tensile strength, compared with unirradiated Inconel X750 material. The embrittlement is characterized by intergranular failure. Although spacers were never found to have failed in-service, upon handling for inspections for post irradiation examination experiments, they suddenly fractured as seen in Figure 1.2.

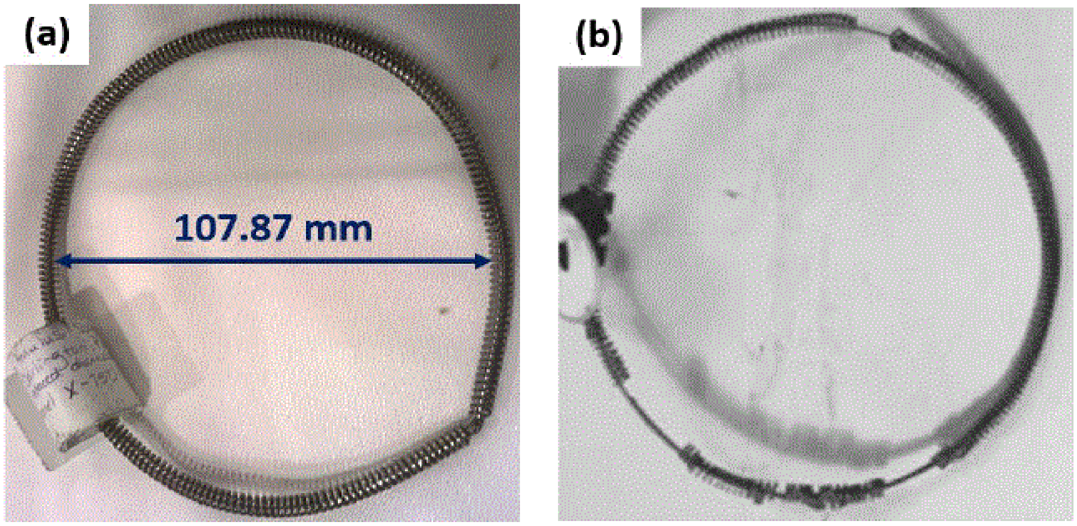

Figure 1.2: Inconel X-750 spacer (a) before service and (b) ex-service [12]

To date, the fundamental mechanisms underlying the irradiation-induced mechanical property degradation in X750 are not well known. Previous studies indicated that helium-induced bubble accumulation on grain boundaries may be important [2,4-6]. Other TEM-based studies of the microstructural stability of irradiated Inconel X750 indicate the correlation between irradiation doses, temperature, and helium concentration on the type of irradiation induced damage formed in the material [7-10]. While studies are still ongoing to understand the relationship of these mechanisms, experimental data to measure the effect of these mechanisms on the mechanical properties of Inconel X750 alloy are still insufficient. Also, not enough data exist to correlate the microstructural changes to the onset of decreased ductility and grain boundary embrittlement. Development of such a correlation remains the missing link that is necessary before accurate predictions of garter spring spacer lifetime can be made as a function of in-reactor location and irradiation history within a CANDU nuclear reactor core.

1.4 Research objectives

The aim of this study is to investigate the effect of helium accumulation and irradiation-induced crystallographic damage, applied by using He^+ and Ni^+ implantation at various temperatures, on the mechanical properties and the grain boundary strength of the Inconel X750 nickel base alloy. The objectives of this study are:

1. To investigate the effect of sole He^+ and Ni^+ implantation on the stability of γ’ strengthening phase through TEM observation.
2. To understand the effect of γ’ precipitate’s order state on the nano-indentation hardness of the ion-implanted Inconel X750 alloy.
3. To study the effect of Ni^+ and He^+ implantation on the grain boundary.
4. To explore the effect of sequential implantation (He^+/Ni^+) at different implantation temperature on the mechanical properties of Inconel X750.
5. To study the effect of sole- and sequential- Ni^+/He^+ implantation on the indentation depth dependence of the hardness of Inconel X750.

1.5 Structure of the thesis

This thesis is written in the integrated-article format as defined by the School of Graduate and Postdoctoral Studies at the University of Western Ontario. It contains 6 chapters, 4 of which contain detailed description of different investigations carried out in this research.

Chapter 2 of this thesis contains a review of published literature on the theories, mechanisms and techniques which were applied to achieve the objective of this study. Description of the radiation -induced damage and its general effect on the mechanical properties of metals, particularly Ni-based superalloys and FCC metals, are also included.

Chapter 3 presents the results of a study of the effect of sole He^+ and Ni^+ ion implantation, performed at 25°C, on the nanoindentation hardness of Inconel X750 in the solution annealed (SA) and the heat treated (HT) conditions. TEM/SEM analysis of the HT and SA X750 are presented to explore the effect of γ'-precipitate instability on the observed indentation hardness. A version of this chapter was submitted for publication to the Journal of Nuclear Engineering and Radiation Science [August 2019]. Portions of early preliminary results of this investigation were presented in the following conferences: (1) AccApp '17, 13th International Topical Meeting on Nuclear Applications of Accelerators, 2017- Québec- Canada, (2) 28th Canadian Materials Science Conference, 2016-Hamilton, Canada, and (3) UNENE R&d Workshop December 2015, Toronto-Canada.

Chapter 4 presents the result of a study of the effect of sequential He^+/Ni^+ implantation, performed at 25°C and 200°C, on the indentation hardness of heat treated Inconel X750. Existing model expressing the effect of helium accumulation, ion-induced atomic displacement, and local heating during ion implantation were applied to predict the observed results. The indentation hardness size effect was also studied for non-implanted, sole Ni^+ or He^+ - implanted and sequentially Ni^+/He^+ -implanted conditions. A version of this chapter was submitted to the Journal of Nuclear Engineering and Radiation Science [August 2019]. Portions of early preliminary results of this investigation were presented in the 12th CANDU owners Group Fuel Channel Seminar-May 2017, Ajax Convention Centre -Toronto-Canada.

Chapter 5 reports the effect of accumulated helium nano-bubbles and radiation-induced defects on the grain boundary strength of Inconel X750. This study involved both micro-cantilever beam bending test and FE modelling. A version of this chapter was also published in the Journal of Nuclear Materials [11]. Portions of early preliminary results of this investigation were presented in (1) AccApp '17, 13th International Topical Meeting on Nuclear Applications of Accelerators, 2017- Québec- Canada, and accepted in (2) NuMat 2018: The Nuclear Materials, Seattle, WA-USA.

Finally, general and specific conclusions drawn from the research along with recommendations for future research are presented in Chapter 6.

1.6 References

[1] M. A. Stopher, "The effects of neutron radiation on nickel-based alloys," Mater. Sci. Technol., vol. 33, no. 5, pp. 518–536, 2017.

[2] M. Griffiths, "The Effect of Irradiatoin on Ni-containing Components in CANDU Reactor Cores: A Review," AECL Nucl. Rev., vol. 2, no. 1, pp. 1–16, 2013.

[3] R. A. Holt, "In-reactor deformation of cold-worked Zr – 2.5 Nb pressure tubes," J. Nucl. Mater., vol. 372, pp. 182–214, 2008.

[4] C. D. Judge et al., "Intergranular fracture in irradiated Inconel X-750 containing very high concentrations of helium and hydrogen," J. Nucl. Mater., vol. 457, pp. 165–172, 2015.

[5] M. Griffiths et al., "Degradation of Ni-alloy Components in CANDU Reactor Cores," in 16th Int. Conference on Environmental Degradation of Materials in Nuclear Power Systems – Water Reactors, Asheville, North Carolina, USA,August 11-15, 2013.

[6] C. D. Judge et al., "Embrittlement of nickel alloys in a CANDU reactor environment," 25th Int. Symp. Radiat. Eff. Mater., vol. 1547, pp. 161–175, 2013.

[7] H. K. Zhang, Z. Yao, C. Judge, and M. Griffiths, “Microstructural evolution of CANDU spacer material Inconel X-750 under in situ ion irradiation,” J. Nucl. Mater., vol. 443, no. 1–3, pp. 49–58, 2013.

[8] H. K. Zhang, Z. Yao, M. R. Daymond, and M. A. Kirk, “Elevated temperature irradiation damage in CANDU spacer material Inconel X-750,” J. Nucl. Mater., vol. 445, no. 1–3, pp. 227–234, 2014.

[9] H. Zhang, Z. Yao, M. R. Daymond, and M. A. Kirk, “Cavity morphology in a Ni based superalloy under heavy ion irradiation with cold pre-injected helium. I,” J. Appl. Phys., vol. 115, no. 10, 2014.

[10] H. Zhang, Z. Yao, M. R. Daymond, and M. A. Kirk, “Cavity morphology in a Ni based superalloy under heavy ion irradiation with hot pre- injected helium . II,” J. Appl. PHYSIC, vol. 115, 2014.

[11] M. N. Tawfeeq and R. J. Klassen, “Effect of ion implantation on the grain boundary strength of heat treated Inconel X750,” J. Nucl. Mater., vol. 516, pp. 255–263, 2019.

[12] C. B. Howard, “Development of Novel Small Scale Mechanical Tests to Assess the Mechanical Properties of Ex-Service Inconel X-750 CANDU Reactor Components,” 2018.

[13] “http://www.civil.uwaterloo.ca/watrisk/research.html.” .

Chapter 2

2 Review of the literature

This chapter reviews previously published findings related to Inconel X750 and its use within CANDU nuclear reactors. Fundamental theories associated with irradiation-induced microstructural damage and its impact on the mechanical properties of crystalline metals is then presented. Specific studies associated with the use of high-energy particles implantation to emulate neutron irradiation is discussed along with their implantation effects on phase changes, lattice defects and cavity production in FCC metals.

2.1 The Inconel X750 alloy

Inconel X750 is a precipitation-hardenable Ni-based superalloy known for its exceptionally high strength and resistance to chemical degradation at elevated temperature approaching $0.80T_{melt}$ (T_{melt} ~ 1700 K) [1,2] X750 is frequently used in high-temperature structural applications in the nuclear and aerospace industries. At room temperature this alloy displays a continuous matrix, referred to as the γ phase, which is of Face Center Cubic (FCC) crystal structure (Figure 2.1) and provides the X750 alloy with exceptional ductility. The γ phase is typically present as large equiaxed grain shape of about 15 - 45 μm diameter. The principal alloying elements in Inconel X750 are Cr (14-17%) and Fe (5-9%) [2,3]. A second group of elements, Al, Ti and Nb are also present, in smaller concentrations. These elements are highly soluble in Ni and, when subjected to thermal treatment, form an atomically coherent, γ' precipitate (Ni_3[Ti, Al]). The exceptionally good mechanical properties of Inconel X750 at elevated temperature is due primarily to the presence of this ordered γ' phase.

Inconel X750 is also strengthened by the presence of larger, atomically incoherent, metal carbides; namely, (Ti, Nb)C and smaller $Cr_{23}C_6$. The latter carbides tend to precipitate preferentially along γ phase grain boundaries while (Ti, Nb)C existed in grain interior and grain boundaries [4,5]. These carbides strengthen the X750 alloy and, at high temperature, inhibit creep by suppressing grain boundary sliding [4].

Plastic deformation of the FCC γ phase of Inconel X750 occurs primarily by <110> {111} dislocation slip. The presence of the ordered γ′ phase in heat treated X750 impedes this deformation process by creating antiphase boundaries (APB) resulting from forced substitution of a Ni atoms into Al or Ti lattice sites as dislocations move through the γ′ phase. Consequently, the dislocation glide occurs along <100> which does not reside on the atomically close packed {111} plane. The thermal activation energy for this type of deformation is four times greater than normal <110> {111} γ phase dislocation slip and this results in the excellent strength displayed by heat treated Inconel X750 [2].

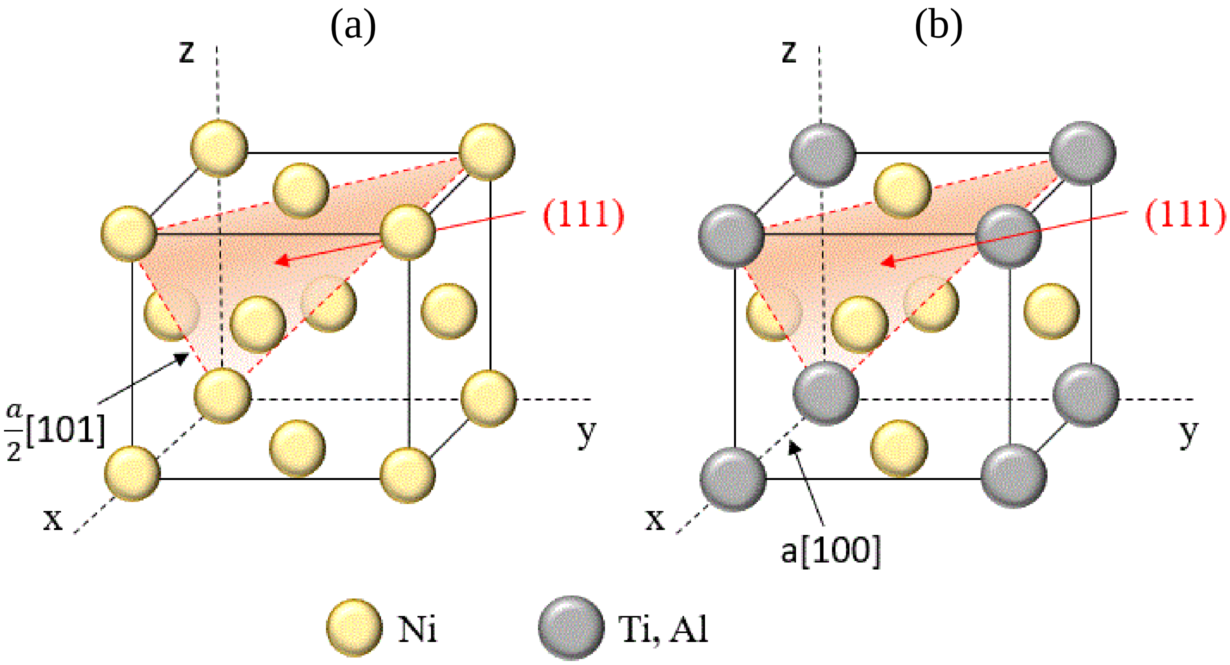

Figure 2.1: FCC crystal structure of the (a) X750 γ matrix and (b) γ′ Ni3(Al/Ti) precipitate.

2.2 Fundamentals of radiation-induced crystal damage

Metal components in a nuclear reactor core are subjected to significant neutron exposure and this can lead to considerable microstructural changes, often referred to as radiation damage. At its most fundamental level radiation damage is the result of simple elastic and in-elastic collisions between neutrons and atoms of the exposed metal. Various neutron –

atom interactions are schematically illustrated in Figure 2.2 and are detailed in the next section.

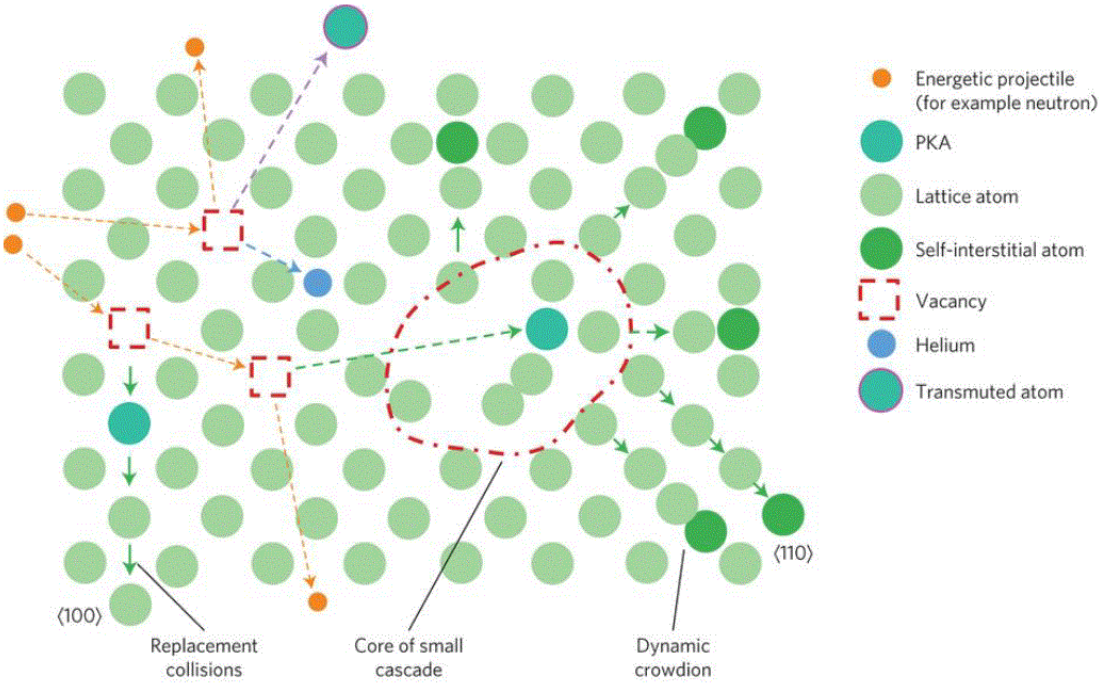

Figure 2.2: Schematic illustration of the different interaction types between high energy particles, such as a neutron, and atoms in a crystal lattice [6]. The first atom displaced via direct collision with the neutron is called the primary knock on atom (PKA).

2.2.1Neutron-induced atomic displacement damage

In general, bombarding a periodic, crystalline arrangement of atoms with high energy particles (i.e. neutron, ion, or electron) will dislocate atoms from their lattice sites. For an atom to be displaced from its lattice site, a minimum value of energy needs to be transferred to the atom during the collision. This energy, referred to as the threshold displacement energy Ed, depends on the direction of particle – atom impact and the crystallographic structure of the lattice [6-9]. The first atom displaced via direct collision with the neutron is called the primary knock on atom (PKA). PKAs with an energy two or three times larger than E_d go on to displace other atoms from their lattice sites until they reach energies below

E_d, producing a cascade of displacements in the atomic structure, generating pairs of self-interstitial atoms and vacancies (Frenkel pairs) in the crystal [10]. The energy deposited in the crystal by this series of collisions results in a very short duration localized thermal spike within the crystal. During this thermal spike phase, most of the displaced atoms manage to return to the normal lattice sites. However, some atoms that are unable to return to low-energy lattice sites will result in a population of interstitial atoms, and associated vacancies, to remain in the irradiated crystal [8]. The interstitial point defects will tend to agglomerate to form larger defects. The density and distribution of defects depend basically on the particle species and the energy of the incident particles.

The mass of the incident particle is important for determining the amount of energy transferred to the first stationary atom it encounters (i.e. the PKA). This transferred energy (T) can be expressed as [11]:

$$T = \frac{\Lambda E_k}{2}(1 - cos\theta_s) \tag{2-1}$$

where E_k is the kinetic energy of the incident particle, θ_s is the scattering angle in a collision system, and Λ is the mass ratio given by:

$$\Lambda = \frac{4(mM)}{(m+M)^2} \tag{2-2}$$

where m and M are the mass of incident particle and the mass of stationary atom respectively. The maximum transfer energy (T_{max}) will occur during a head on collision (θ_s =180°) and is given by:

$$T_{max} = \Lambda E_k \tag{2-3}$$

and for all other possible collisions, the average transferred energy is about ($T_{max}/2$) [12].

2.2.1.1 Quantification of atomic displacement damage

Many models were developed to quantify the number of atoms displaced by one PKA. The most frequently used model is that of Kinchin-Pease (referred to here as the K-P model) [10]. This model assumes that all particle – atom collisions are elastic and that a particle of energy less than E_d will not displace atoms from their lattice site, and the energy above a specific cutoff energy E_c will dissipate in electronic excitation and ionization without generating atomic displacement. Between E_d and E_c, however, there is a linear relationship between the PKA energy and the number of displaced atoms (Frenkel pairs) produced (Figure 2.3). Therefore, the average number ν_d of secondary displaced atoms created by a PKA of energy T can be calculated using K-P model as:

$$\nu_d = \begin{cases} 0 & for \quad T < E_d \\ 1 & for \quad E_d < T < 2E_d \\ \dfrac{T}{2E_d} & for \quad 2E_d < T < E_c \\ \dfrac{E_c}{2E_d} & for \quad T \geq E_C \end{cases} \tag{2-4}$$

It is important to note that the K-P model does not take consider point defect annihilation (i.e. interstitial – vacancy recombination) process that will occur during the displacement cascade. The implication of this is that the effect of temperature on a particle-atom displacement process cannot be determined by application of the K-P model in this simple form.

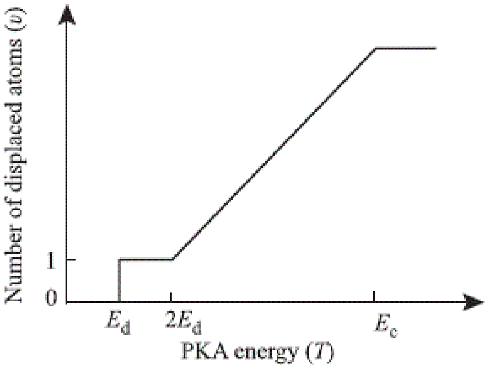

Figure 2.3: Number ν_d of displaced atoms in the cascade as function of the PKA energy according to Kinchin-Pease model [11].

Norgett, Robinson, and Torrens (NRT) developed more detailed model based on K-P method that consider both the elastic collision and electronic stopping power. This model assumes that only a portion of the PKA energy is consumed for elastic collision with atoms in the lattice, and thus the number of displacement per atoms is dependent on this portion, while the remaining fraction of energy is dissipated by electronic loses. The total number of displaced atoms (ν_{NRT}) produced via a PKA in this model is given by [13]:

$$\nu_{NRT} = \begin{cases} 0 & for \quad T_{dam} < E_d \\ 1 & for \quad E_d < T_{dam} < 2E_d \\ \dfrac{\beta T_{dam}}{2E_d} & for \quad T_{dam} \geq 2E_d \end{cases} \tag{2-5}$$

where T_{dam} is the energy portion dissipated in elastic collisions, and β (=0.8 for Ni based alloys [7]) is an empirical factor found to be a function of the kinetic energy of PKA; that is the factor decreases with increasing the PKA energy because of the rise in the electron stopping power [14].

Particle impact induced atomic displacement damage is quantified in terms of the Displacement Per Atom (dpa); the number of times an atom is displaced from its lattice position by collision with single particle, such as a neutron or ion, of specific kinetic energy. This unit was introduced to the nuclear field for the purpose of comparative discussion between different irradiation parameters [9]. “dpa” can be computed using Stopping Range of Ions in Matter (SRIM) software. SRIM utilize Monte Carlo simulation to trace the path of the high energy incident particle as it collides, and is deflected by, the crystalline target material. The SRIM software can then be used to calculate the dpa as a function of particle penetration depth. While the SRIM program is running the high energy incident particle undergoes multiple interactions with substrate atoms and each one results in an energy loss along with deflection of the particle and possible displacement of the impacted atom. The particle-atom interaction process is stochastic and the SRIM software models it iteratively with a Monte Carlo simulation. Two methods are available in SRIM to calculate the particle induced atomic damage; full cascade and quick methods. The full cascade method takes in to account all collision damages created from recoil atoms and the secondary displacements they produce. While the quick method employs the NRT model and include only the initial displacements caused by the original projectile. Both methods follow the injected particle until its energy drops below the target E_d and can no longer displace target atoms. SRIM input information like the implanted ion type, chemical composition of the target compound and the ion energy range over which the calculation has to be performed. SRIM output data (Figure 2.4) then gives the number of atomic displacements (vacancies) produced by a single particle, i.e. Ni^+ or He^+, based on the ion energy and target material properties. By using these data, it is possible to calculate the ion fluence required to create a certain level of irradiation damage, and corresponding dpa, as [15]:

$$dpa = \frac{\phi \times 10^8 \times D}{N} \qquad (2\text{-}6)$$

where ϕ is the incident ion fluence (ion/cm^2), D is the vacancy production rate (vacancy/ion/Å) calculated by SRIM and N is the atomic density (atom/cm^3) of the target material.

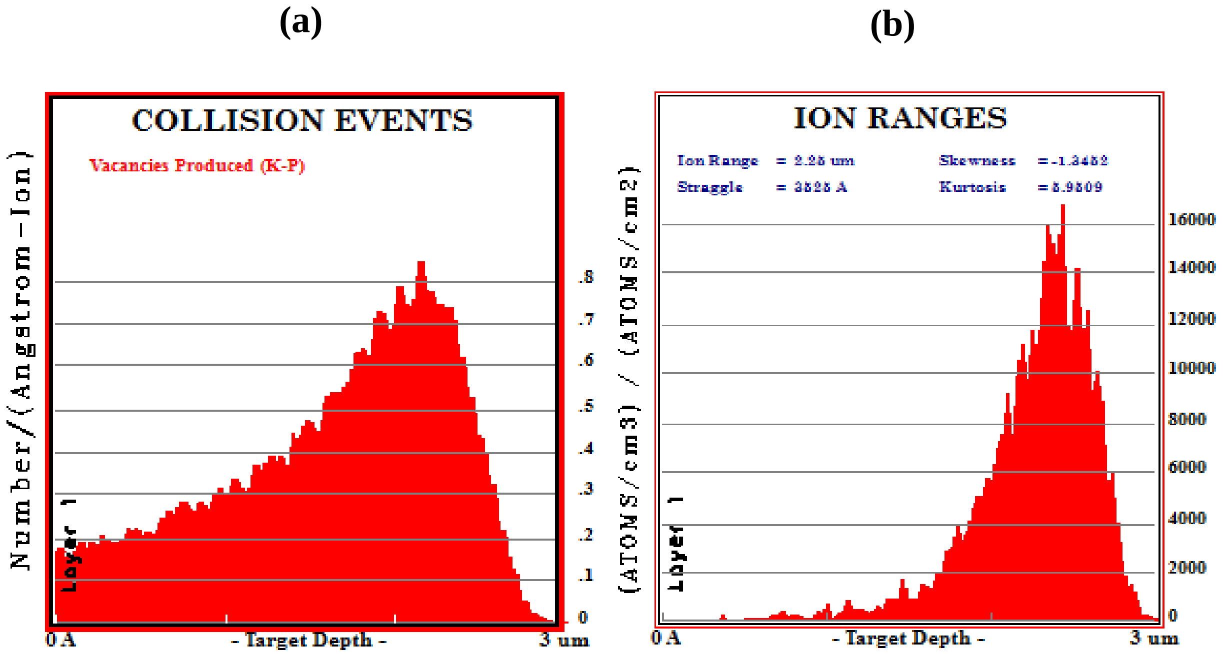

Figure 2.4: SRIM output plots illustrate: (a) damage profile of 8 MeV Ni+ in Inconel X750 (b) ion range in target material (X750)

It is worth to mention that an issues have been reported regarding the use of full cascade method in SRIM; that is the number of displacement obtained using this method is almost double in compare to quick method although the damage energy is similar [9]. An additional drawback in SRIM is inability to take both the elastic an inelastic collision theories in the same run. Nevertheless, it remains the most reliable method of evaluating ion behavior in matter.

2.2.2 Nuclear transmutation

Nuclear transmutation refers to a process where one type of sub-atomic particle, either a neutron or a proton, transforms to the other type. The most common example is a neutron spontaneous transmuting into a proton. The mass difference between the neutron and the proton results in the production of a high energy photon (gamma ray) during this process. Transmutation processes occur frequently in metals within nuclear reactor cores where they are exposed to high levels of neutron irradiation. In such a situation a neutron can become absorbed into the nucleus of an atom, of atomic number Z, resulting in the formation of a neutron-rich isotope. These isotopes are frequently very unstable, and the absorbed neutron transmutes to a proton resulting in the creation of a new element of atomic number Z+1. Further atomic stabilization can then occur by releasing a proton or a helium atom (α-decay process) from the atom.

In this thesis we are particularly interested in the nuclear transformation process that occurs in nickel atoms, the primary ingredient of the Inconel X750 alloy, when exposed to neutrons. This process is described as ^{59}Ni(n,α)^{56}Fe and is shown in expanded form below

$$^{58}_{28}Ni + {}^{1}n \rightarrow {}^{59}_{28}Ni \rightarrow {}^{59}_{28}Ni + {}^{1}n \rightarrow {}^{56}_{26}Fe + {}^{4}_{2}He$$

In situations of very high thermal neutron flux, as in the core of heavy-water moderated nuclear reactors such as the CANDU, elements like nickel which have a high neutron absorption cross section and (n, α) transmutation reactions, such as the one described above, result in the production of significant quantities of helium (Figure 2.5). The helium atom is large enough to have low solubility in solid Ni at the reactor operating temperatures

(250-300^{o}C) and therefore tends to accumulate as nano-bubbles or nano-cavities throughout the microstructure [12]. The effect of these nano-cavities, and the effect of dissolved helium in general, on the ductility of heat treated Inconel X750, and its effect on the strength of grain boundaries in particular, is currently an area of active study and is one of the key research topics of this thesis.

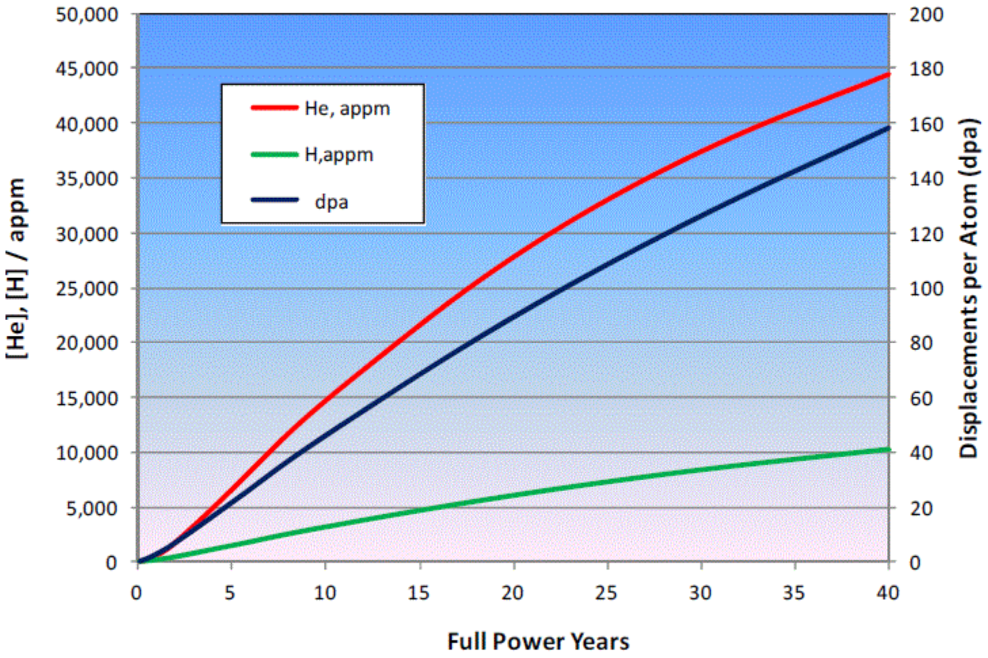

Figure 2.5: Calculated helium and hydrogen gas along with the total displacement damage for an Inconel X-750 spacer in a high power channel of a CANDU-6 reactor at full power assuming a mid-burn-up flux spectrum [3]

2.3 Ion implantation to simulate in reactor neutron radiation

Accelerated ion implantation has been used by material scientists for decades to study radiation-induced damage formation in nuclear materials. Not only to simulate the microstructural changes created by neutrons, accelerated particles irradiation is also used to understand radiation damage fundamental processes in a controlled condition, for which neutron irradiation is difficult to approach, such as material selection, dose level control, and irradiation temperature control [16-19].

Irradiation with high energy heavy ions, producing PKA with higher energy (~5 KeV), results in the production of dense atomic displacement cascades similar to that of neutron irradiation. A tremendous advantage of such a process is that it implants this crystallographic damage at a rate that is about four orders of magnitude higher than in-reactor neutron irradiation induced crystallographic damage. This allows one to create levels of irradiation damage in a test sample that is consistent with an "end of life" in-reactor component after only several hours of ion implantation [17]. This high dpa rate introduces a fundamental difference between ion and neutron irradiation; namely, high energy ion irradiation provides much less time for irradiation-induced defects to migrate after their creation. This affects the type of net irradiation damage produced. To overcome this, it has been suggested that high energy ion irradiation must be performed at significantly higher temperature than neutron irradiation to enhance the interstitial atom migration rate in proportion to the increased dpa rate [11,17,20]. Another drawback in using ion irradiation is that the depth of penetration of the ions into the test material is only on the order of several micrometers [20-22]. Micro or Nano-mechanical testing techniques must therefore be used to assess the mechanical properties of this thin ion-irradiated region. Finally, while reactor neutron radiation is characterized by a spectrum of energies, ion implantations are of a constant energy, and can only be combined sequentially to simulate the effects of irradiation over a wide energy spectrum.

2.4 Grain boundary as sinks for point defects during irradiation

Grain boundaries are acting as sinks for point defects and can play a significant role in absorbing vacancies and interstitials produced during irradiation [23]. The effect of grain boundaries is primarily expressed in terms of their crystallographic misorientation angle, which influences the grain boundary energy. Also associated with the grain boundary energy is the tendency for point defect and impurity accumulation at the boundary to minimize the boundary energy. To gain better understanding of the role of grain boundaries as a sink to point defect, their structure must be characterized.

2.4.1The misorientation of a grain boundary

In a polycrystalline material, a grain boundary is simply described as an interface of two adjacent grains. Since each grain has its own crystallographic orientation, then the misorientation of two adjacent grains can be defined as the difference between the orientation of one grain relative to other. The total misorientation across grain boundary is an important factor in controlling its properties, for instance, energy and diffusivity. The geometric character of a general grain boundary is defined by five degrees of freedom; three define the relative rotation of one grain with respect to another around three axes, and two more define the rotation of the grain boundary plane around either of two axes [24-26]. In other words, there are three ways we can tilt or twist one grain relative to other, and two ways to align the boundary plane between the grains as illustrated in Figure 2.6 a-b. The misorientation between the crystal lattices of two grains can be expressed in axis- angle pair scheme; misorientation axis (UVW) referred to one of the two grains and an angle of misorientation (θ) necessary to transfer both grains to an identical position as shown in Figure 2.6-c [27]. For example, twin boundary misorientation in an FCC structure can be described in angle-axis pair as a 60° <111>.

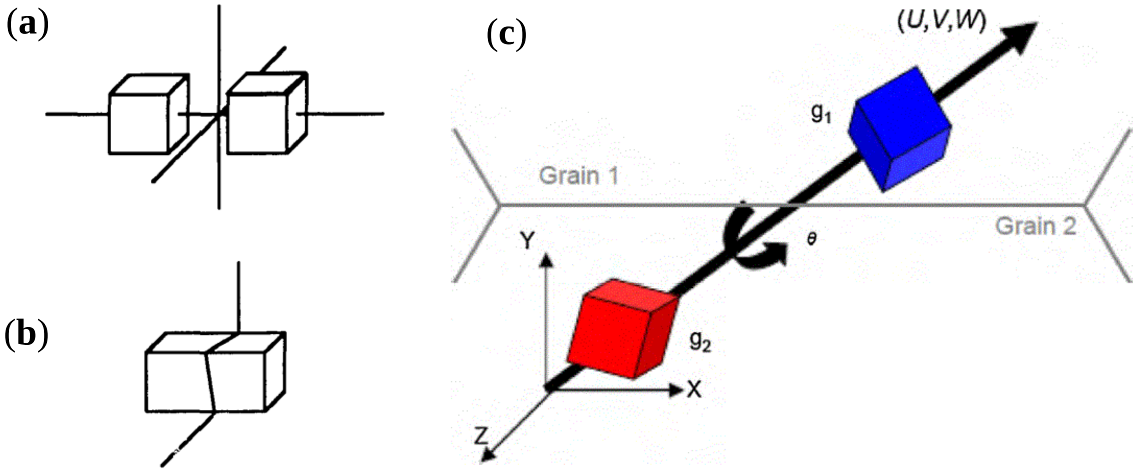

Figure 2.6: The five degree of freedom of a grain boundary, (a) two crystals adjacent at a grain boundary can be rotated around each of three axes; this gives three rotational degrees of freedom; (b) the grain boundary plane has two degrees of freedom for rotation of the plane around either of two axes [26], (c) Schematic of the axis–angle pair for grain boundary description [27].

To determine the grain boundary misorientation angle (θ) along with the associated axis (UVW) of the rotation, the orientation of each grain and its neighboring grain need to be obtained in terms of Euler angles. Electron back scattered diffraction (EBSD) technique is usually used for this purpose. Euler angles $(\varphi_1, \Phi,\ \varphi_2)$ then can be converted to obtain the rotation matrix, g_i**,** for each grain as follows [24]:

$$g_i = \begin{bmatrix} \cos\varphi_1\cos\varphi_2 - \sin\varphi_1\sin\varphi_2\cos\Phi & \sin\varphi_1\cos\varphi_2 + \cos\varphi_1\sin\varphi_2\cos\Phi & \sin\varphi_2\sin\Phi \\ -\cos\varphi_1\sin\varphi_2 - \sin\varphi_1\cos\varphi_2\cos\Phi & -\sin\varphi_1\sin\varphi_2 + \cos\varphi_1\cos\varphi_2\cos\Phi & \cos\varphi_2\sin\Phi \\ \sin\varphi_1\sin\Phi & -\cos\varphi_1\sin\Phi & \cos\Phi \end{bmatrix} \quad (2\text{-}7)$$

This allows for the determination of the misorientation rotation matrix, M_{ij}, between each grain and its neighbor by inverting one of the two adjacent grain matrices and multiplying by other as:

$$M_{ij} = g_i^{-1} g_j \quad (2\text{-}8)$$

The grain boundary misorientation angle (θ) along with the associated axis (UVW) of the rotation were then calculated as:

$$\theta = \cos^{-1}\left(\frac{M_{11} + M_{22} + M_{33} - 1}{2}\right) \quad (2\text{-}9)$$

$$(U, V, W) = \frac{(M_{23} - M_{32}, M_{31} - M_{13}, M_{12} - M_{21})}{\sqrt{(M_{23} - M_{32})^2 + (M_{31} - M_{13})^2 + (M_{12} - M_{21})^2}} \quad (2\text{-}10)$$

2.4.2 Classification of grain boundaries according to the atomic structure

Atomic arrangement within the grain boundary in a polycrystalline metal is significantly different from the periodical arrangement at grain interior. The crystallographic orientation changes suddenly in passing from one grain to the next across the grain boundary. According to this atomic structure or arrangement, the grain boundaries are classified to three categories: low angle grain boundaries, high angle grain boundaries and special boundaries (CSL boundary) [28-30]. Low-angle boundaries, where the misorientation angle is approximately $\theta \leq 15^{o}$, can be represented as a single array of dislocations stacked one above the other as shown in Figure2.7-a [30,31]. On the other hand, Grain boundaries with misorientations angle greater than 15^{o} are considered as high-angle boundaries and their structure consists of region of "random" atomic misfit the size of which is determined by θ (Figure 2.7-b).

In a high-angle boundary a few number of atoms are shared by both grains (i.e. have a coincidental position from one grain to the next) while most belong to neither. The atoms that belong to both grains form what known as a coincidental site lattice (CSL) and they are of special properties as noticed first by Kronberg and Wilson in 1949 [32]. The simplest example is the coherent twin boundary, where boundary is parallel to the twinning plane and the atoms in the boundary fit perfectly into both grains as illustrated in Figure 2.7c. The degree of CSL, denoted as Σ, can be obtained by taking the reciprocal density of coincidental sites; i.e. CSL boundary with $\Sigma 5$ has one coincident point for every five crystal lattice points.

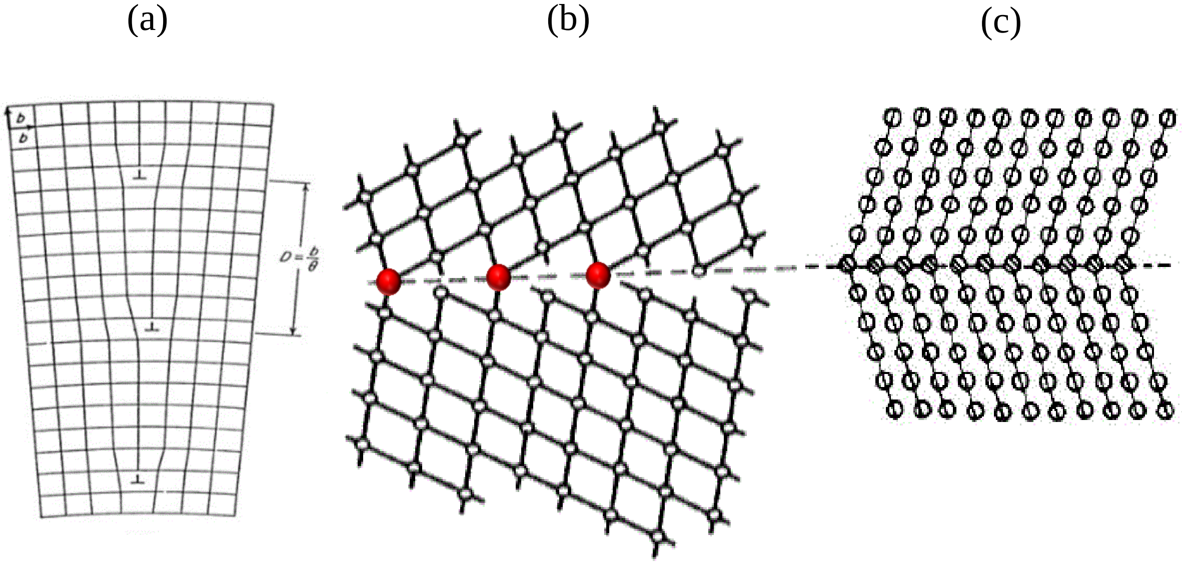

Figure 2.7: illustrate low angle grain boundary (a) two grains joined to form a low angle grain boundary made up of an array of edge dislocations (b) schematic illustration of high-angle grain boundary (Red point represent the CSL sites), (c) coherent twin boundary [28].

Some high angle grain boundaries fall at or nearby CSL misorientations. However, only grain boundary with a misorientation that satisfy Brandon's criterion [33] is considered to be a coincident site lattice boundary:

$$\Delta\theta \leq \theta_B = \frac{\theta_o}{\Sigma^{1/2}} \qquad (2\text{-}11)$$

where $\Delta\theta$ is the deviation angle from the exact CSL misorientation, θ_B is Brandon's criterion and $\theta_o=15^o$ represent the misorientation limit of low angle grain boundary so that all low angle grain boundaries are described as Σ1 [29]. Brandon's criterion is the commonly accepted misorientation limit up to which a boundary structure can be maintained by introducing grain boundary dislocations which can accommodate the boundary's misfit. All high angle grain boundaries that are not falling within Brandon's criterion are considered to be general (or random) boundaries because of their random atomic structure and have no special properties. In current work, the strength of the grain boundaries from all above-mentioned categories were investigated. Low angle grain boundary (10^o Σ1), high angle "random" grain boundary (33^o and 46 ^{o}), and high angle special boundary (57^o Σ3).

2.4.3 Grain boundary energy

The grain boundary energy is directly depending on the atomic structure of the boundary. Low angle grain boundaries have been characterized as low energy boundary since it represents a simple array of dislocations [29,34]. Read and Shockley [30] derive a theoretical expression for the grain boundary energy of low angle tilt boundary based on a simple dislocation model. However, this model is not valid for θ exceeding 15^o because the dislocation strain fields overlap with each other to such an extent that they lose their identity and the simple dislocation theory upon which this model is based becomes unsuitable [35].

CSL special boundaries also possess low energy, because of their high density of shared "coincident" atoms. These special boundaries exist as cusps in the boundary energy-misorientation relationship (Figure 2.8) [27,36,37]. On the other hand, high angle grain boundaries (random boundaries) have higher energy than the grain interior because its atomic arrangement is differing from that of bulk grain; i.e. the atomic bonds in the boundary core are broken or highly distorted in comparison to those of the grain interior [34,38]. For example, the energy of high angle boundary in Ni is 866 mJ/m^2 in comparison to 43 mJ/m^2 for coherent twin Σ3 boundary [39]. The energy of such boundaries is usually calculated via atomistic computer simulation [27,36]. Due to the high energetic states, a system tends to reduce its total energy by interaction of grain boundaries with other defects such as solute or impurity atoms. As a consequence, these solute atoms accumulate (segregate) at grain boundaries to such an extent that the boundaries may become weakened [29,40,41].

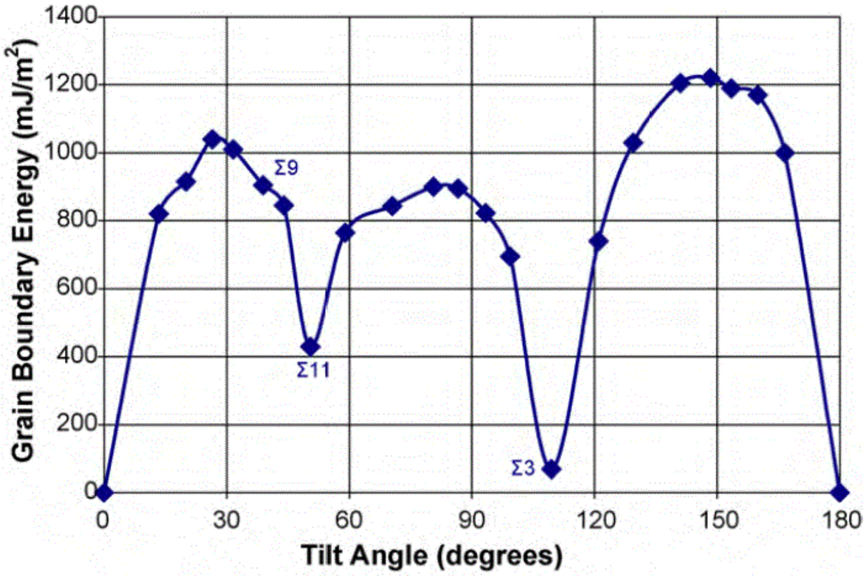

Figure 2.8: Schematic representation indicating grain boundary energy as a function of misorientation angle for Ni [27]. Special CSL Σ boundaries represent low energy cusps specially for Σ3 (coherent twin).

2.4.4 Correlation of grain boundary character, radiation-induced phenomena, and embrittlement

Radiation induced grain boundary phenomena such as radiation induced segregation (RIS), radiation enhanced diffusion, and void denuded zone (VDZ) are known to cause a significant degradation in the local properties of crystalline materials. These phenomena are closely related to the point defects and defect clusters produced during irradiation [42,43]. These defects that escape recombination and are mobile will re-integrated into the crystal structure through segregation to individual grain boundaries and other defect sinks [11].

The grain boundary sink strength is primarily expressed in terms of their crystallographic misorientation angle which influences the grain boundary energy [28,40]. Also associated with the grain boundary energy is the tendency for defect and impurity accumulation at the boundary to minimize the boundary energy [29,41]. Radiation induced diffusion and segregation of crystal point defects to grain boundaries has garnered extensive research with a number of studies examining factors related to this phenomenon in nickel alloys [43,44], austenitic stainless steel [42,45,46], and copper [41,47]. Watanabe et al [42] found a relationship between the tilt grain boundary sink strength and the misorientation angle as shown in the below equation:

$$S^{GB} = A\, sin\frac{\theta}{2} \tag{2-12}$$

where θ is tilt angle and $A = 2Z/(bd)$ is a parameter can be obtained for edge dislocation, here b is burger vector, d is the inter planner spacing and Z is an enrichment factor. Using this equation in the simulation model and compare it to the experimental results, they observed that, after 1MeV electron irradiation austenitic stainless steel with 3 dpa, the RIS was enhanced as the tilt angle increased but was suppressed at coincidence grain boundaries Σ9 and Σ3 as shown in Figure 2.9. This means that the strength of the segregation at grain boundaries depends on their structure; and that random high energy grain boundaries have more preferential sites for point defects or solute segregation than low energy boundaries such as CSL [40].

Barr et al. [43] noticed a major variations in RIS of Cr and void denuded zones only between the coherent and incoherent Σ3 twin grain boundaries but show minimal difference in Cr depletion between low-angle and high-angle GBs in Ni^+ irradiated Ni-5Cr alloy. Han et al. [47] found significant correlation between the width of void denoted zones (VDZs) and grain boundary character in helium irradiated Cu at elevated temperature. Specifically, the width of VDZs are larger at non special CSL boundaries than at Σ3 tilt boundaries, and the width of VDZ is proportional to the misorientation angle, indicating variability in grain boundaries sink strength with their characters.

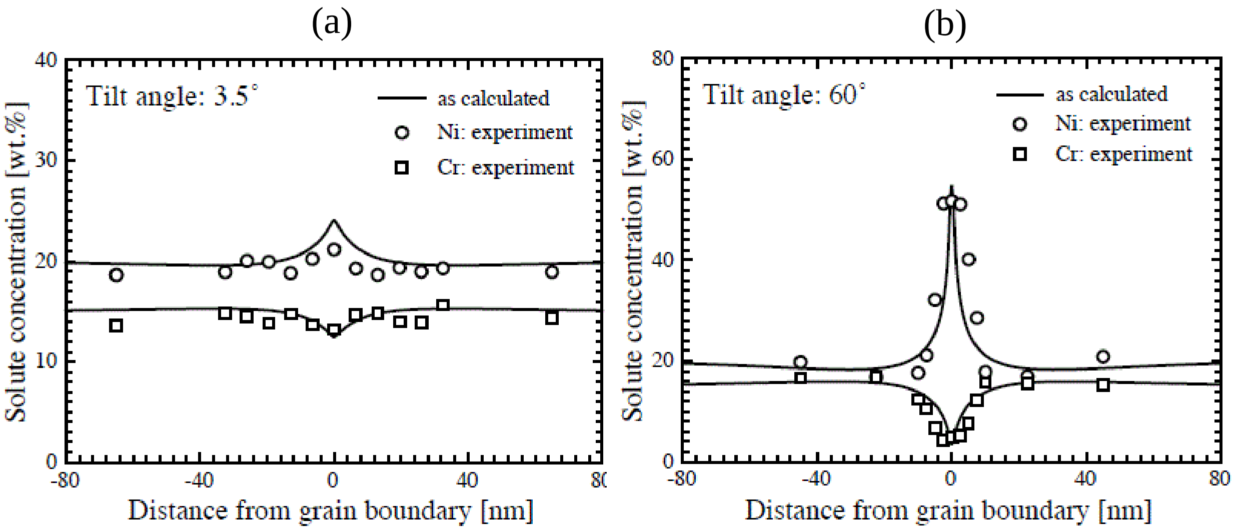

Figure 2.9: RIS of Ni and Cr at two different grain boundaries of austenitic stainless steel after irradiation to 3 dpa at 450 °C: (a) low angle tilt boundary (θ =3.5°), (b) random grain boundary (θ =60°); solid lines are theoretical predictions and unfilled characters are experimental data [42].

The accumulation of point defects, impurity atoms, and voids in individual grain boundaries known to cause dramatic changes in the localized solute composition which is responsible for the radiation induced embrittlement. The response of individual GBs, however, is dependent on the grain boundary structure or character [41,43,48,49]. Monzen et al. [41] found that the fracture toughness of Cu-2.0wt.%Sb alloy depend sensitively on the misorientation angle as shown in Figure 2.10-a. Local peaks were observed at different misorientation angles such as θ =28.1° (Σ17), θ =36.9° (Σ5), and θ =67.9° (Σ17). Interestingly, the position of these peaks agrees with those cusps presented in Sb concentration and the grain boundary energy plots (Figure 2.10, b-c). Therefore, they conclude that the high energy boundaries are more susceptible to Sb segregation and hence become more brittle and fracture more easily at lower tensile stress. Similarly, Micro-cantilever beams, containing a single grain boundary with known misorientation, were tested in bending to study the effect of small quantities of bismuth on the grain boundary embrittlement of copper [50]. The results show that among different oriented grain angles, the high angle boundaries fractured at a lower stress. This was correlated with the results from TEM-EXD studies performed to investigate the local chemical composition of four grain boundaries (two of which had fractured and two had not). Bismuth was found at the grain boundaries which had fractured and not at the boundaries which had not fractured (i.e. bismuth segregated to high angle grains).

The above-mentioned radiation induced grain boundary phenomena have been observed in Inconel X750 spacer material such as He bubbles void-denuded zone, intergranular embrittlement and impurity segregation [3,51,52]. However, it was never linked to the grain boundary structure. In this thesis a correlations are determined between boundary character and strength for Inconel X750 grains tested in bending before- and after- ion implantation (Chapter 5).

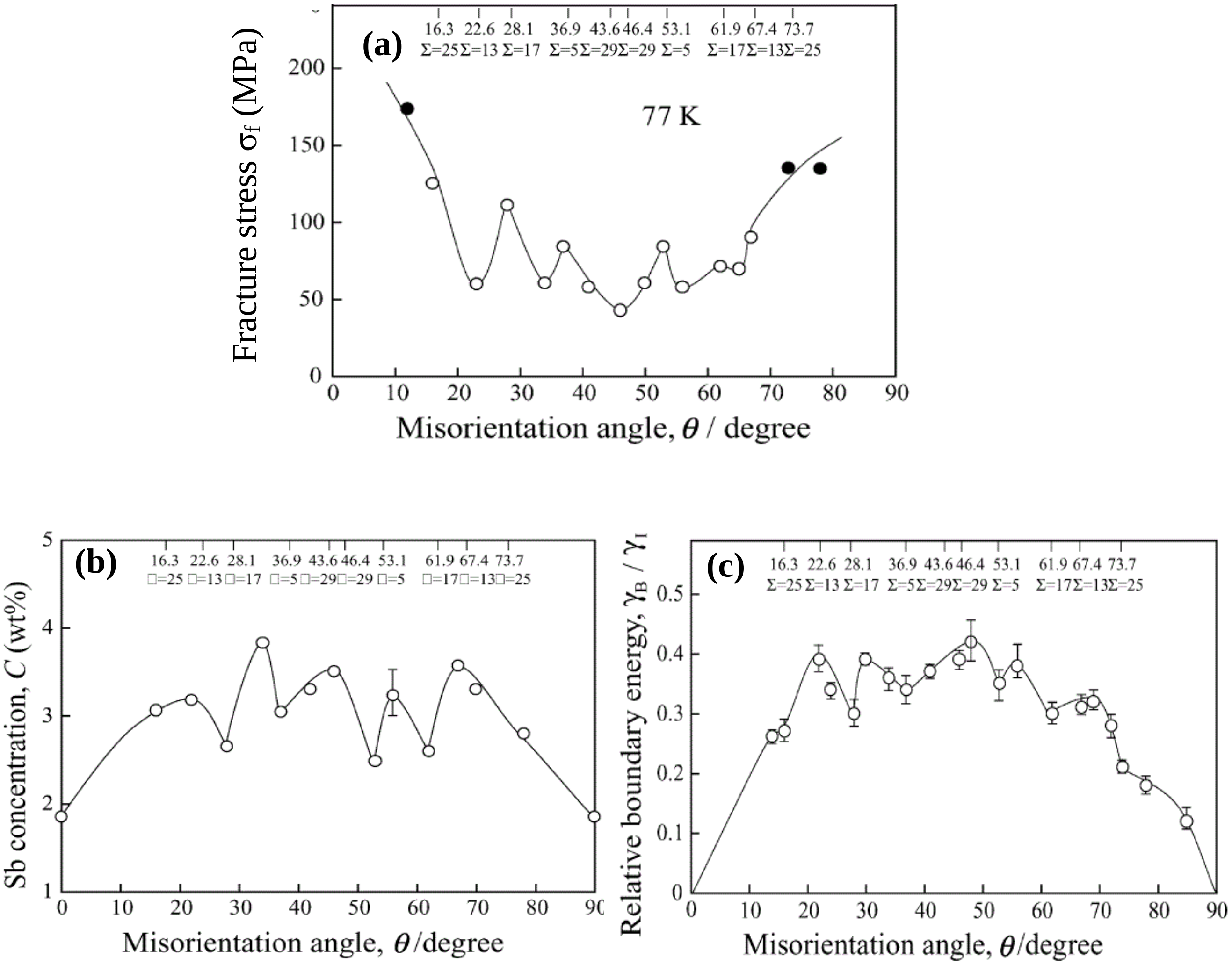

Figure 2.10: Dependence of fracture stress of Cu–2.0 wt.% Sb bicrystals on the misorientation angle, (b) Dependence of Sb concentration at each boundary in Cu–2.0 wt.% Sb bicrystals on the misorientation angle, (c) Relative boundary energy γ_B/γ_Iplotted against the misorientation angle [41].

2.5 Radiation damage in a CANDU reactor core

Previous sections of this chapter have covered the basic mechanisms by which neutron radiation invokes atomic displacement damage and helium transmutation products in Ni-bearing alloys located in a nuclear reactor core. In this section we will consider specific details of the characteristic crystallographic damage accumulation in heat treated Inconel X750 components located in a CANDU reactor core.

2.5.1 Fast neutron damage

The calculated neutron flux versus neutron energy profile at the Inconel X750 spacer location (red) in a CANDU reactor is shown in Figure 2.11. This profile is typical of a heavily moderated fission reactor and is characterized by a high flux of low energy thermal neutrons.

Fast neutrons ($E > 1.0$ MeV) induce direct atomic displacement damage follows many steps. To displace a Ni atom from its crystal lattice, a neutron with energy exceeds the Ni threshold displacement energy, $E_d \leq 40$ eV, is required [7]. Therefore, the minimum neutron energy needed to dislocate Ni atom, by direct collision, from its crystal lattice is 580 eV [53]. When neutrons within this energy range displace a Ni atom, the displaced Ni atom will then have a recoil energy approximately equal to its threshold energy (40eV), which is sufficient to generate a primary knock on atom (PKA). The resulting PKA will transfer most of its recoil energy to neighboring nuclei through secondary and tertiary collisions, dislocating more atoms. These secondary recoils in turn displace other atoms, and hence collision cascade develops as shown in Figure 2.2.

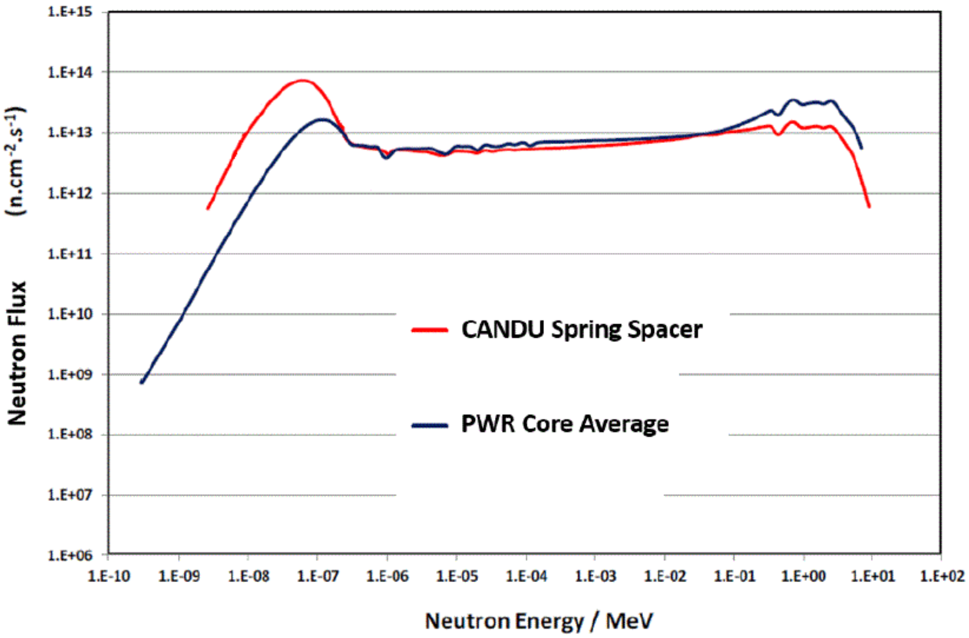

Figure 2.11: Neutron flux spectra seen by an Inconel X750 spacer compared to that seen in an average PWR core [3].

Such cascade occurs in a very short time and can comprise hundreds of displaced atoms depending on the initial PKA recoil energy. After the development of the cascade and depending on the irradiation temperature, the vacancies and interstitials that born during displacement cascade, have the opportunity either to recombine or to migrate to separate sinks, and eventually end up in different defect morphologies [12]. For instants, the vacancies combine into small clusters that can turn into stacking fault tetrahedron (SFT) in X750 and other FCC metals, with possibility to grow into large cavities. Also, the residual interstitials coalesce into dislocation loops. The evolution of point defects along with irradiation-induced segregation, and enhanced diffusion is responsible for the mechanical property degradation in X750 spacer, such as irradiation hardening and grain boundary embrittlement which will be discussed in subsequent sections.

The accumulated displacement damages are controlled by the energies of the incident neutrons. In CANDU reactor the neutron energies span in a range of magnitudes from 0.0001eV-10MeV depending on the location in the reactor (Figure 2.11). For an average CANDU fuel channel power profile, each Ni atom in X750 spacers will be displaced once a year by fast neutrons, which equal to 25 displacement per atom (dpa) in their lifetime in the reactor [53].

As aforementioned, this fast neutron damage is not the only type of radiation damage seen by the structural materials before they reach their end of life. This damage is supplemented by the presence of thermal neutron irradiation.

2.5.2 Thermal neutron damage

The displacement damages caused by thermal neutron irradiation are of insignificant importance in comparison to that created by fast neutron. However, for components comprise Ni, absorption of thermal neutrons will cause transmutation that leads to production of hydrogen and helium. Inconel X750 alloy contain 70 wt % Ni atoms. Nickel is basically composed of five different isotopes; ^{58}Ni is the most abundant isotope (67.8%) followed by ^{60}Ni (26.2%) then ^{61}Ni, ^{62}Ni, and ^{64}Ni (6.1% in total). Although all isotopes of

Ni have display a large tendency to absorb neutrons, only ^{58}Ni is able to transmute to the unstable ^{59}Ni isotope and emitting γ ray by a capturing thermal neutron as shown below in ^{58}Ni (n, γ) reaction [53,54]:

$$^{58}\mathrm{Ni} + n \rightarrow {}^{59}\mathrm{Ni} + \gamma$$

Up on the presence of thermal neutron, the concentration of the produced ^{59}Ni isotope will increase until reach a maximum concentration of ~4% of the ^{58}Ni concentration after 5-10 years depending on its location in CANDU reactor as shown in Figure 2.12-a [3]. ^{59}Ni, in turn, has a very high cross-sections for absorbing thermal neutrons and producing hydrogen and helium through (n, p) and (n, α) transmutation processes. The ^{59}Ni decays by several possible processes as shown below:

$$^{59}\mathrm{Ni} + n \rightarrow {}^{56}\mathrm{Fe} + {}^{4}\mathrm{He} \qquad (n, \alpha)$$

$$^{59}\mathrm{Ni} + n \rightarrow {}^{59}\mathrm{Co} + \mathrm{H} \qquad (n, p)$$

$$^{59}\mathrm{Ni} + n \rightarrow {}^{60}\mathrm{Ni} + \gamma$$

The ^{59}Ni (n, γ), (n, p) and (n, α) reactions are very exothermic, producing both charged particles and heavy atomic recoils which lead to enhanced displacement damages [55]. For instance, the ^{59}Ni (n, γ) reaction generate α particles (4.8 MeV) that produce 62 atomic displacements per neutron capture [54]. While the recoiling ^{56}Fe (340 keV) produce 1701 atomic displacements per neutron capture event [56].

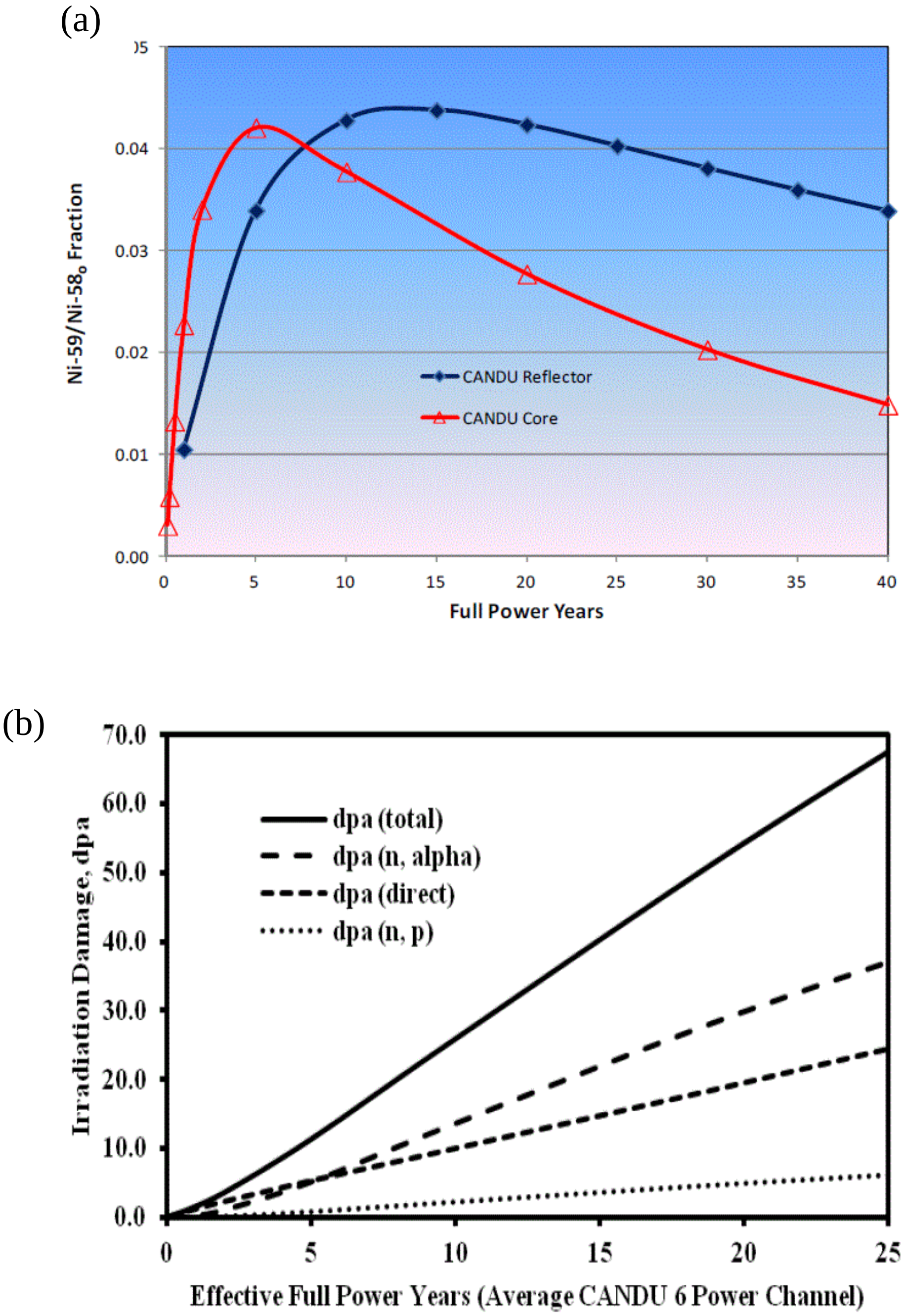

Figure 2.12: (a) ^{59}Ni production as a fraction of the original ^{58}Ni concentration for the central core and reflector region of CANDU-6 reactor [3]. (b) Total displacement damage and the contributions from each reaction for Inconel X750 using the neutron flux of an average fuel bundle [53]

When ^{59}Ni concentration reaches its peak values in the reactor, the radiation damages produced by thermal neutrons can exceed those produced by fast neutrons. Figure 2.12-b shows the displacement damages from an average CANDU bundle power channel at X750 spacer location. It's clear from Figure 2.12-b that the largest contribution to total displacement damages is generated via (n, α) reaction with 35dpa out of total 60 dpa after 25 years of service. While the displacement damages produced by direct collision with epithermal and fast neutrons (>600 eV) contributes approximately 25 dpa at the end of spacer life. There is also a large amount of hydrogen and helium gas production through ^{59}Ni (n, p) and (n, α) transmutation reactions which reach up to 44000appm He and 5000appm H by the end of life of the CANDU spacer [3]. The accumulation of these gases has an effect on the defect morphology in X750, and thus its mechanical properties.

2.5.3 Helium and hydrogen production

In a CANDU reactor the primary effect of neutron irradiation on the properties of X750 spacer is through the displacement of atoms. However, the production of gaseous atoms hydrogen and helium by (n, p) and (n, α) transmutation reactions also has deleterious consequences on spacer properties. At the temperature within a CANDU core, hydrogen is relatively soluble and extremely mobile within a solid, but helium is completely insoluble. Thus, helium atoms will find small vacancy clusters or pre-existing defect sinks such as dislocations, grain boundaries, and precipitate interfaces, to form micro-bubbles. With ongoing irradiation, the bubbles grow by absorbing the continuously produced helium. This process accelerates material hardening and the onset grain boundary embrittlement [3,12,52,57].

Figure 2.5 depicts the calculated concentration of helium and hydrogen gases along with the atomic displacement damage for an Inconel X750 spacer as a function of time in a CANDU reactor.

2.6 Radiation damage effect on the mechanical properties and microstructure

Displacement damages and the gases production during radiation can alter the microstructure significantly, which in turn cause a dramatic degradation in the mechanical properties of the materials. In this section the radiation-induced hardening will be reviewed, along with the irradiation-induced microstructural changes in Ni superalloys such as defects formation (dislocation loops, stacking faults tetrahedra, and cavities/bubble) and the order state of the strengthening phase γ'.

2.6.1 Irradiation hardening

The theories of irradiation hardening can be regarded as a comprised of two mechanisms; source hardening and friction hardening. Source hardening is the increase in the stress needed to unlock pinned dislocations and set them free to move on their slip planes. Once the dislocation released and during their movement, a radiation-induced defects lying on the slip plane will resist their motion. The resistance stress experienced by dislocation is known as friction hardening. Friction hardening is also defined as the stress required to sustain the plastic deformation [11,58]. For instance, in irradiated FCC metals and alloys such as Inconel X750, the radiation-induced defect clusters near Frank–Read sources increase the required stress for loops expansion and to allow source multiplication. Once the applied stress is sufficient to unlock the source, and the dislocation begin moving, the moving dislocations can eliminate the small defect clusters and reduce the stress needed to continue the plastic deformation under friction hardening mechanism.

Friction hardening can be characterized according to the source of hardening in to long-range hardening and short-range hardening:

$$\sigma_F = \sigma_{LR} + \sigma_{SR} \tag{2-13}$$

Long-range hardening resulted from the repulsive interaction between a moving dislocation and components of the dislocation network within the matrix of the alloy. Short range hardening resulted from the interaction of moving dislocation with an obstacles lie in its slip plane where it is moving. The stress in this case will increase only when the dislocation contacts the obstacle. Each obstacle, whether it be a precipitate, dislocation loop, void or helium bubble has its own short-range hardening stress, so the total short-range hardening can be expressed as the sum of each individual defect's short-range hardening:

$$\sigma_{SR} = \sigma_{precipitate} + \sigma_{loops} + \sigma_{bubbles+\cdots} \qquad (2\text{-}14)$$

Dislocations can overcome these barriers by either bowing around the obstacle, cutting through or climbing over it. The last two processes require the addition of energy by increasing the temperature while the bowing around the obstacle is temperature independent [11].

2.6.2 Gamma prime (γ') disordering

Inconel X750 and other Ni superalloys in their heat treated condition are strengthened by coherent ordered $Ni_3(Al, Ti)$ γ' precipitates, and retains their high strength and creep resistance at elevated temperature due to the high thermal stability of the γ' precipitates. During service in reactor, neutron radiation changes the thermodynamic state of the precipitate through radiation-induced mixing and destabilize γ' precipitates. In the disordered state of γ', Ti and Al atoms will be knocked out of their corner atom lattice sites and settle into temporary residence at a vacant lattice site or interstitial site. Under such disordered condition of γ' the contribution of the antiphase boundary and elastic coherency strain to its hardening has been erased.

Earlier studies on the γ' state of order under heavy ion irradiation have revealed the irradiation temperature and dose rate dependence. Nelson et al [59] stated the disordering of γ' at temperatures below nearly 325°C at a dose rate of 10^{-2} dpa/sec, while above this critical temperature the γ' precipitates remain stable. Following study by Camus et al [60] shows that at a lower dose rate, 10^{-3} dpa/sec, γ' state of order changes according to two temperature regimes as illustrated in Figure 2.13. For irradiation temperatures below 270 °C, a two-step process occurs where γ' precipitates first disorder at low dose (~0.1 dpa) and then fully dissolved at a higher dose (> 1 dpa). For the temperature range between 270°C and 350°C, disordering and dissolution occur simultaneously at a higher dose (> 10 dpa) because radiation enhanced diffusion is enough to cause reordering and slow down dissolution. The results of [59,60] emphasis the fact that γ' state of order (disordering and dissolution) is highly dependent on dose rate; that is the high rates of radiation-induced mixing will not give enough time for thermal diffusion to occur. Therefore, changes in dose rates will lead to shifts in critical temperature.

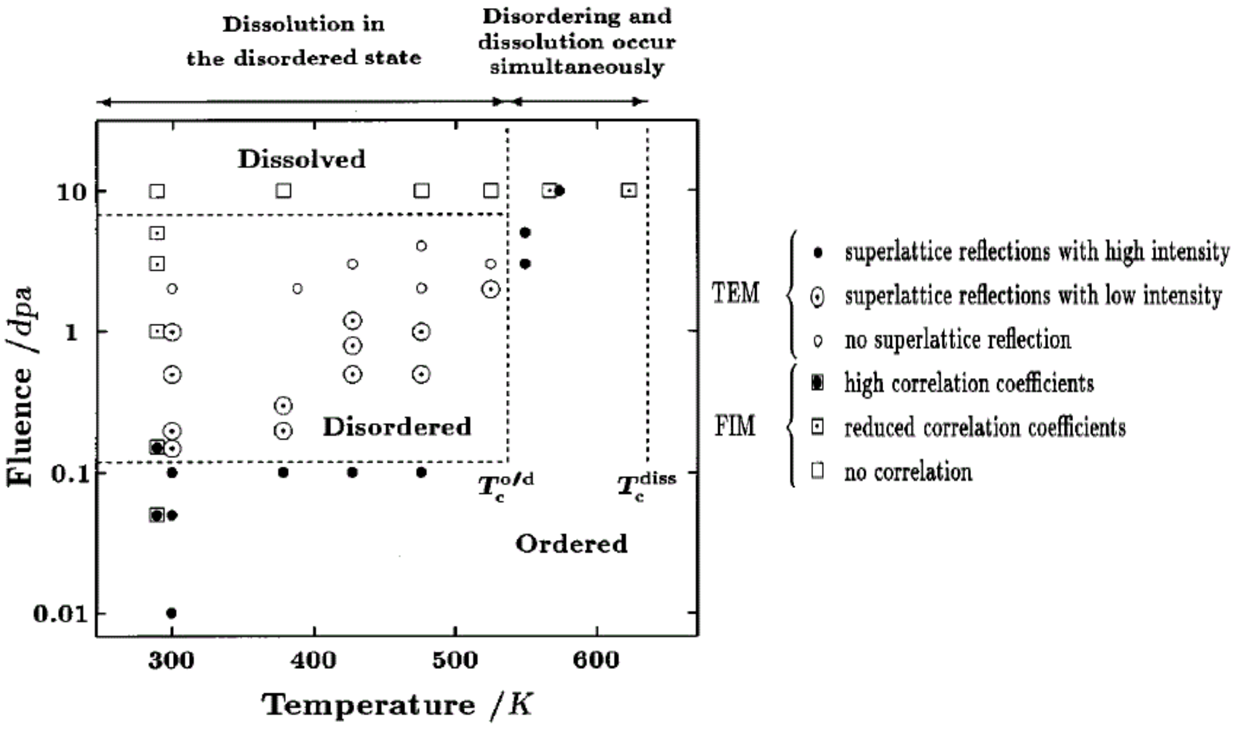

Figure 2.13: Disordering and dissolution kinetics of γ' precipitates under 300 keV Ni^+ irradiation at a dose rate of 10^{-3} dpa/sec [60].

Recent systematic TEM study performed by Zhang et al [61] on X750 in which he irradiated the alloy with Kr^{2+} ions at a dose rate of 10^{-3} dpa/sec up to a maximum dose of

5.4 dpa at a range of irradiation temperatures 60-400 °C , and then a following investigation at 500 °C and 600 °C. The dose evolution of the γ′ disordering was tracked by incrementally imaging its superlattice diffraction patterns at several doses and irradiation temperatures. The results show that at temperatures below 400°C, γ′ precipitates become disordered at a low dose (0.06 dpa), while it remains stable up to 5.4 dpa at higher irradiation temperature as shown in Figure 2.14. The effect of γ′ disordering or dissolution on mechanical properties of irradiated Inconel 718 has been extensively investigated [62-64].

(a)

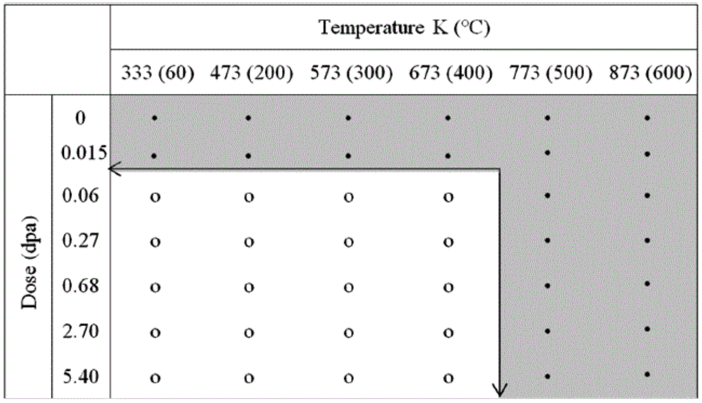

		Temperature K (°C)					
		333 (60)	473 (200)	573 (300)	673 (400)	773 (500)	873 (600)
Dose (dpa)	0	•	•	•	•	•	•
	0.015	•	•	•	•	•	•
	0.06	o	o	o	o	•	•
	0.27	o	o	o	o	•	•
	0.68	o	o	o	o	•	•
	2.70	o	o	o	o	•	•
	5.40	o	o	o	o	•	•

• Indicates the superlattice reflections observed; o indicates no superlattice reflection observed; γ′ were disordered at dose <0.06 dpa when the material was irradiated at temperature 333 K to 673 K (60 °C to 400 °C), but they stayed ordered at ≥773 K (500 °C).

(b)

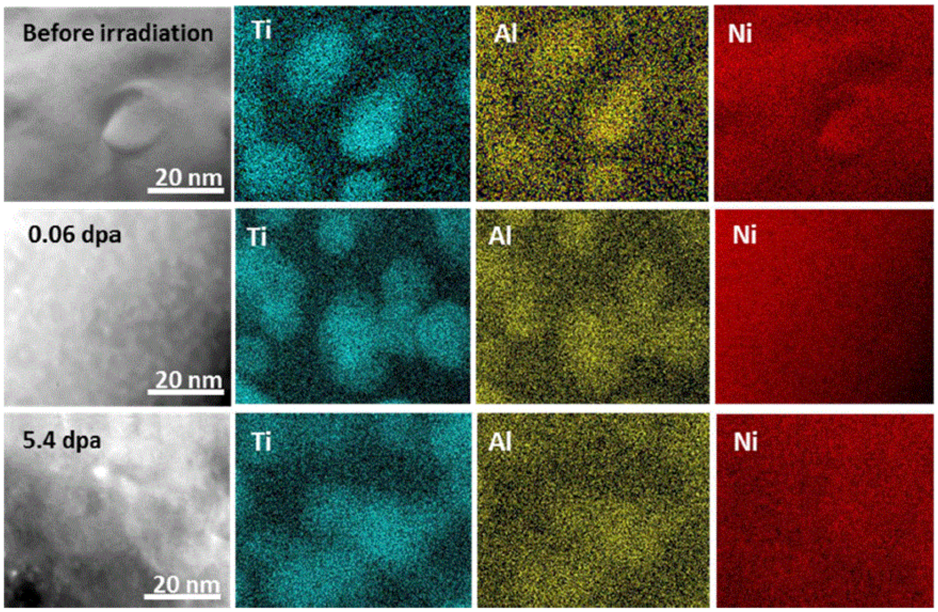

Figure 2.14: (a) Disordering kinetics of γ′, (b) Post-irradiation ChemiSTEM mapping of γ′ precipitates after irradiation at 300°C up to 0.06 and 5.4 dpa [61]

This alloy is precipitation hardened with both γ' and γ''. Following irradiation, the hardness drops rather than increase which indicates material softening. This softening behavior is a strong evidence on the contribution of strengthen phase to hardening, which is higher than that of irradiation hardening induced by dislocation loops and cavities [62,63].

Hun et al [62] studied the effect of Fe^+, He^+ and H^+ either single or triple beam irradiation on the stability of γ' and γ'' and their consecutive effects on the mechanical properties of Inconel 718. Results shows a decrease in hardness with increasing irradiation dose as depicted in Figure 2.15-a. TEM observation indicated that at 1dpa Fe^+ the superlattice diffraction spots of both precipitates disappeared. Although the Fe^+ irradiation added radiation defects, the loss of γ' and γ'' precipitates outweighed the hardening contribution from these defect. In a follow up TEM study by Hashimoto et al [63] in which a microstructure investigation has been performed on the samples irradiated in Ref [62]. They observed the disordering of the of γ' and γ'' precipitates after 0.2 at % He implantation with their superlattice spots became less intense, until a complete dissolution at 14 at % He concentration as shown in Figure 2.16. However, a hardening as a function of He^+ concentration was noted up to 14 at % He concentration where partial softening began (Figure 2.15-b). This indicate the buildup of helium bubbles in the matrix and their associate pinning occurs at higher rate than the disordering of γ' and γ'' precipitates, until the complete dissolution of both precipitates.

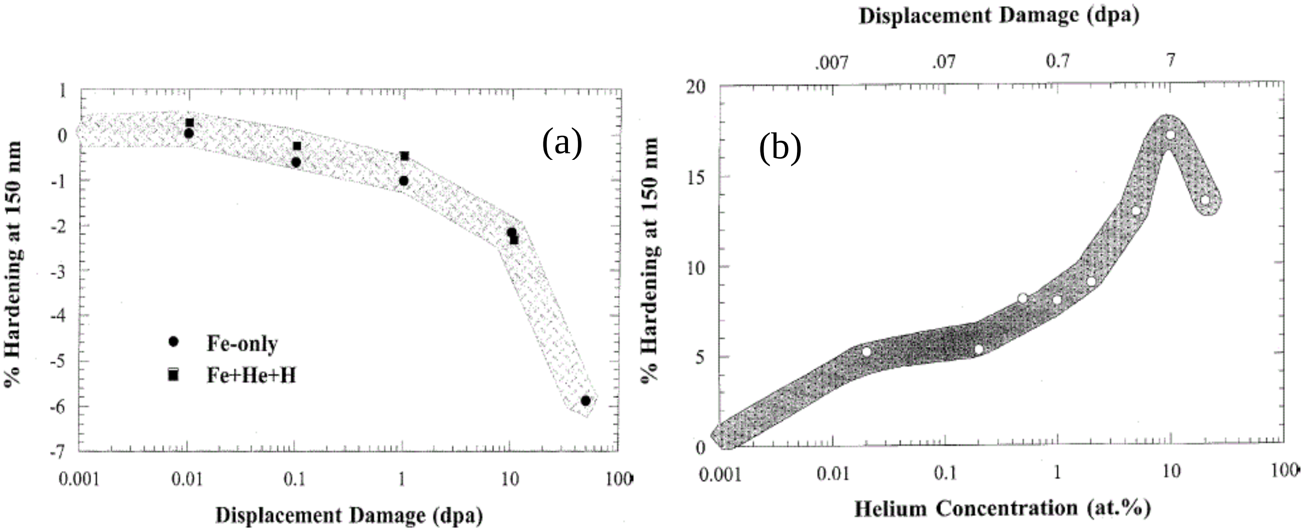

Figure 2.15: Percent change in hardness relative to the unirradiated material for Inconel 718 as (a) function of Fe-only and from triple-beam irradiation (b) function of He+ concentration [62].

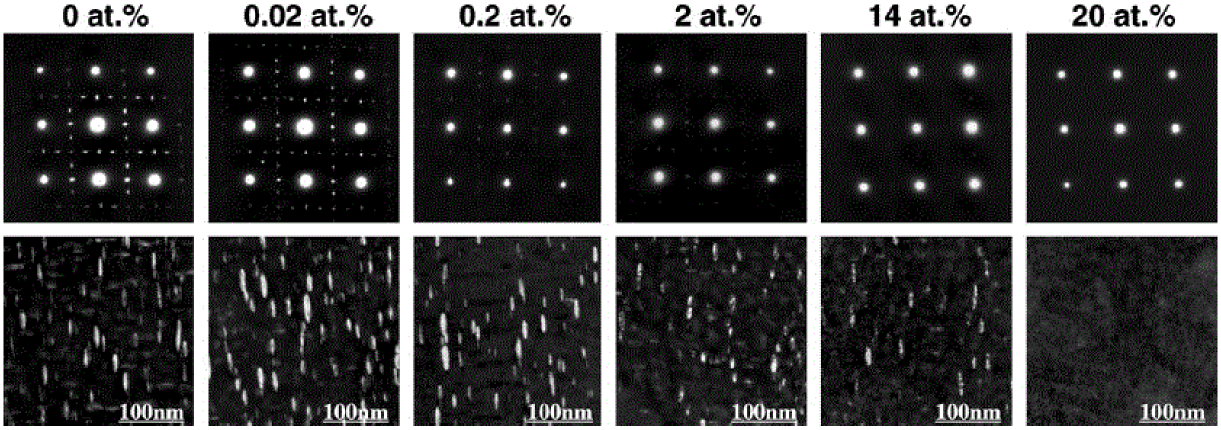

Figure 2.16: Microstructures and diffraction patterns as a function of helium concentration for helium implanted Inconel 718 [63].

2.6.3 Radiation-induced defect

As mentioned earlier, radiation by energetic particles can displace atoms from their lattice site through displacements cascade and produce point defects. These point defects may follow one of three regimes; either recombine with their opposite peer to annihilate, escape from cascade to become free migrating defects, or accumulate to form defect clusters. The defect agglomeration in FCC structure appear either in 3D clusters such as cavities and SFT, or in planner way to form dislocation loops [65]. In Inconel X750 components, these defects are being visible at relatively low irradiation temperature < 400°C.

The Dislocation loops that are seen consist of Frank (faulted) loops and perfect loops (Figure 2.17). Both types are formed by either removing or introducing extra layer of atoms from the matrix causing an extrinsic or intrinsic stacking fault. The majority observed dislocation loops in FCC metals are interstitial in type [66]. Frank loops are sessile, and form on {111} close pack plane with burger vector of 1/3 <111>. They can turn to perfect loops by the movement of 1/6<112> Shockley partial dislocation across the fault removing one layer of atoms. The new perfect loops have a burger vector of 1/2<110>. This is the nature of how perfect loops is created [67]. In situ TEM observations of ion irradiated X750 [68] reveals that the size of the dislocation loops is mainly depend on irradiation temperature.

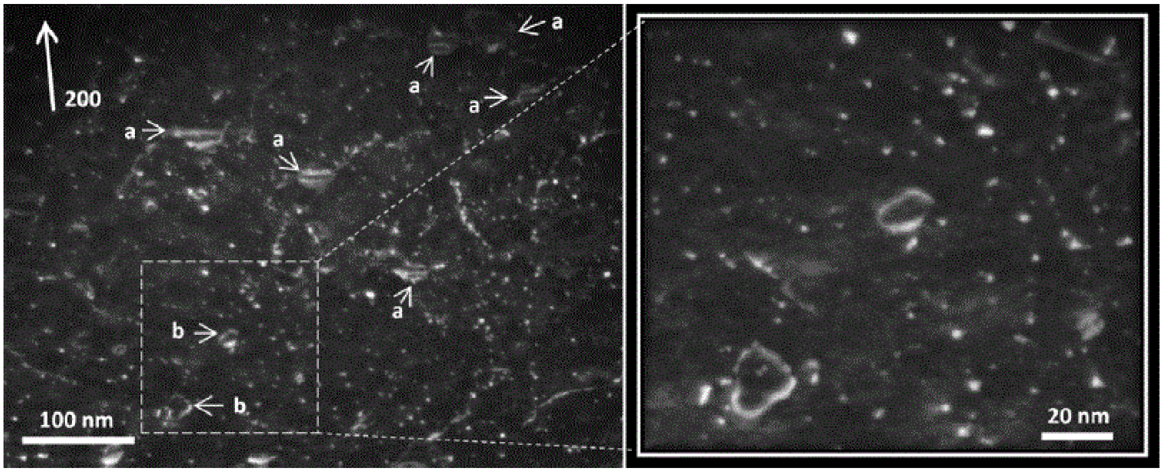

Figure 2.17: Microstructure induced by irradiation at 600 °C to 0.27 dpa. (a) 1/3<111> type faulted Frank loops and (b)1/2<110> perfect loops [68]

The loops formed at irradiation temperature below 400°C have a size of 1-5nm, while larger loops (~10nm) where observed at higher temperature >500°C. Furthermore, the number density of the dislocation loops is dose dependent; regardless irradiation temperature, the density of loops increased rapidly with irradiated dose level until in saturated as shown in Figure 2.18.

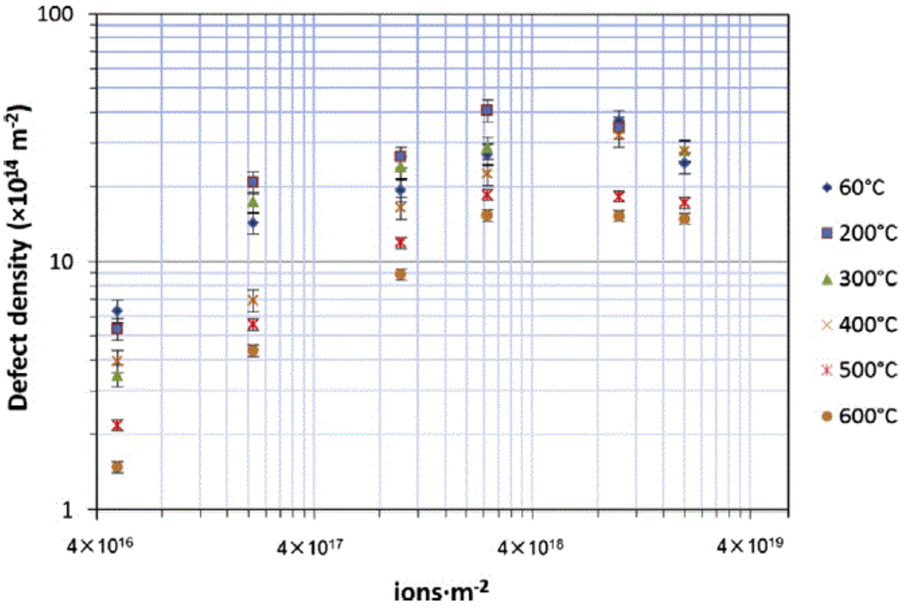

Figure 2.18: Defect number density in X750 as a function of irradiated dose at different irradiation temperature [68]

Stacking Fault Tetrahedron (SFT) is another arrangements of dislocations observed in FCC metals consist of tetrahedron stacking faults on {111} planes (i.e. four triangular planes) with six 1/6 <110> stair rod dislocation along the edge of the tetrahedron. Generally, the SFT can be produced by the collapse of vacancies platelet, which in turn arise from local supersaturation of vacancies produced by displacement cascades, and form 1/3 <111> Frank loops surrounding a loop. The Frank loop dissociates to stair rod dislocation and 1/6 <112> Shockley partial dislocation on intersecting {111} slip plane. By the gliding of the Shockley partial dislocation toward the apex of the tetrahedron formed by three intersecting planes and the original loop, an SFT will be created [67,69]. In X750, the SFTs forms at the very beginning of irradiation (Figure 2.19), and then decomposed with continues irradiation. The number density of SFTs is independent of the irradiation temperature or dose. While their size is proportional to the irradiation temperature, but not to the irradiation dose, with mainly 1-2 nm at low irradiation temperature but larger size was observed at higher temperature. This is because the SFTs act as sinks and absorb the free migrating vacancies and thus grow [70].

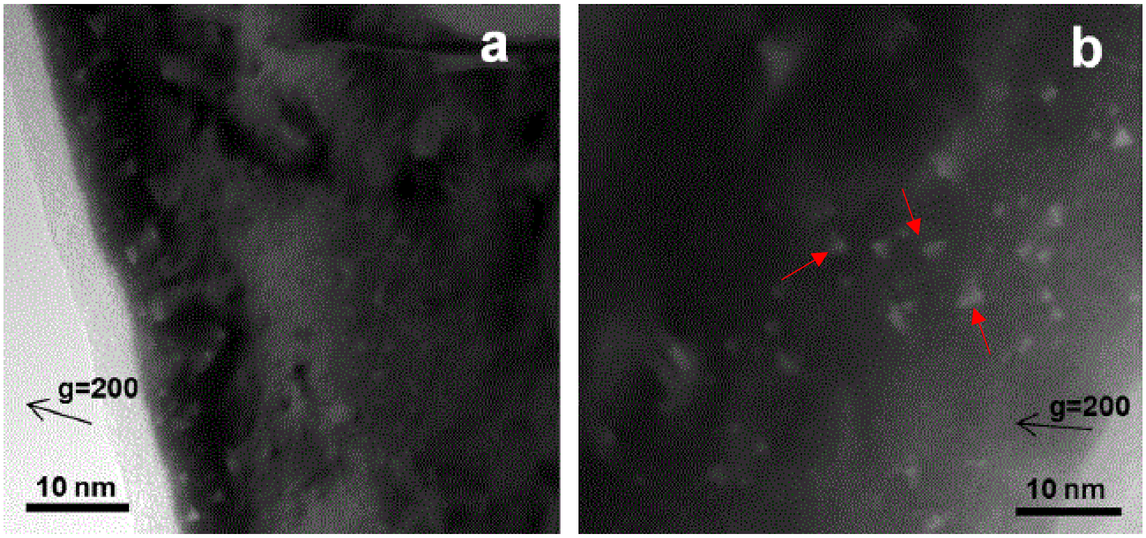

Figure 2.19: TEM micrograph close to zone axis [011] and g = 200 showing formation of SFTs. (a) 0.27 dpa at 60°C and (b) 0.27 dpa at 400°C [70]

The largest contributors to radiation hardening are the high densities of radiation produced immobile defect clusters because they have strong barrier strengths and the high resistance to dislocation motion. However, at a critical dose, the density of these defects is known to saturate and reach an equilibrium when the recombination and nucleation of these defects become even, and defect density remains stable with sustained irradiation [40,57,70]. Therefore, irradiation hardening from defects such as dislocation loops and SFTs reaches a maximum value.

Cavities are basically a three-dimensional clustering of vacancies. It may be empty and termed as voids or filled with gas and called bubbles. Cavities were observed in ex-service X750 spacer as a result of high rate of helium production during transmutation reaction. The size, distribution and density of the cavities are highly depending on the operation temperature as shown in Figure 2.20. At the pinched part of the spacer (operating between 60°C-310°C), the cavities are uniformly distributed in the matrix with small size of 1-2 nm, while at the un-pinched part (~310°C), larger cavity size was detected and are not distributed homogeneously; mostly segregate along the grain boundaries and precipitate interfaces [3,53,71].

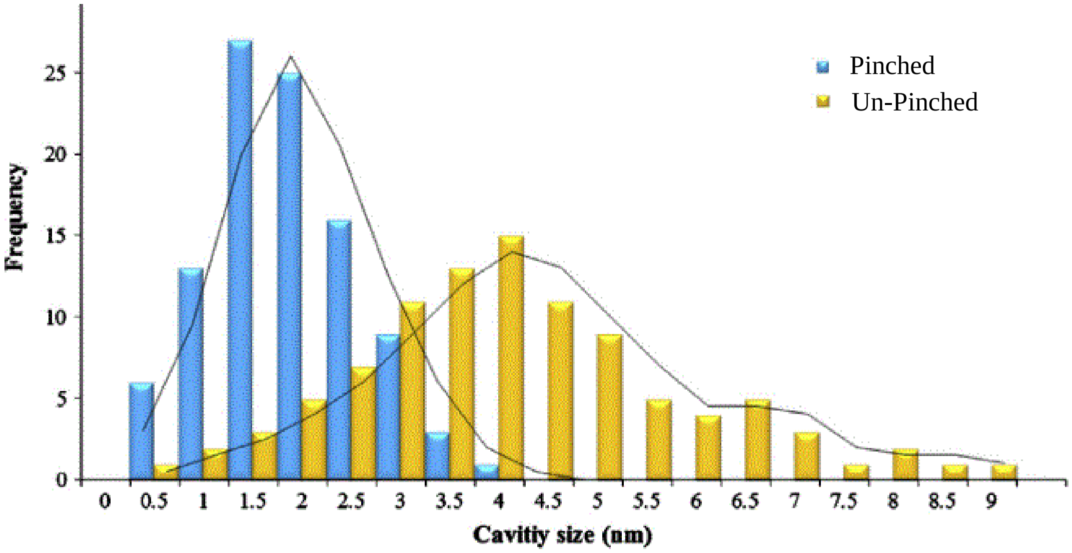

Figure 2.20: Statistical analysis showing cavity size distribution in pinched and un-pinched region in ex-service X750 spring spacer [71].

Unlike ex-service neutron irradiated material, cavities were not observed in heavy ion irradiated X750 even at high irradiation temperature because of the absence of transmutation reaction under such condition. This indicate that helium produced by (n, p) and (n, α) reactions is crucial in facilitating nucleation of cavities in X750 as its thought to enhance the nucleation of cavities by providing sites for vacancy clusters to form. In addition to helium atoms availability, cavity nucleation requires the vacancies to be mobile, supersaturation of vacancies is necessary, and sufficient vacancies must survive from recombination and annihilation, which requires the creation of interstitial-biased sinks such as interstitial loops [72].

Cavities (void or bubbles) formation and growth is of great concern in radiation environment. Bubbles are known to cause grain boundary embrittlement [3,52], and void swelling which is an increase in volume and a decrease in density that leads to changes in component dimensions and mechanical properties [11,73]. Therefore, to better understand the cavity nucleation, growth and their effect on the material properties through energetic particle irradiation experiments, helium must be injected in to the metal prior to energetic particle irradiation to simulate reactor environment [51,72,74-76]. TEM observation of X750 pre-implanted with cold helium followed by heavy ion irradiation demonstrate that cavity formation depends on the concentration of injected helium, irradiation dose and temperature [76]. The concentration level of implanted helium thought to influence the number density of the nucleated cavities and affect their size; high helium concentration will cause the formation of higher density of small size cavities as shown in Figure 2.21. This suggest that the given amount of vacancies is dispersed to more cavities, and hence the smaller and more uniformly distributed cavities nucleated.

At high temperature irradiation, a reduction in cavities density was observed due to the reduction of vacancy supersaturation. Also, high irradiation temperature may rise the vacancy diffusion rate and thus enhance cavity growth. In other study [75], where cold helium was injected in to X750 alloy prior to proton irradiation at 380°C, an enrichment of bubbles along grain boundaries was observed as shown in Figure 2.22. It is also found that sole helium implantation at room temperature and high temperature result in cavity formation in grain boundary and grain interior in Ni and Ni superalloy [51,77].

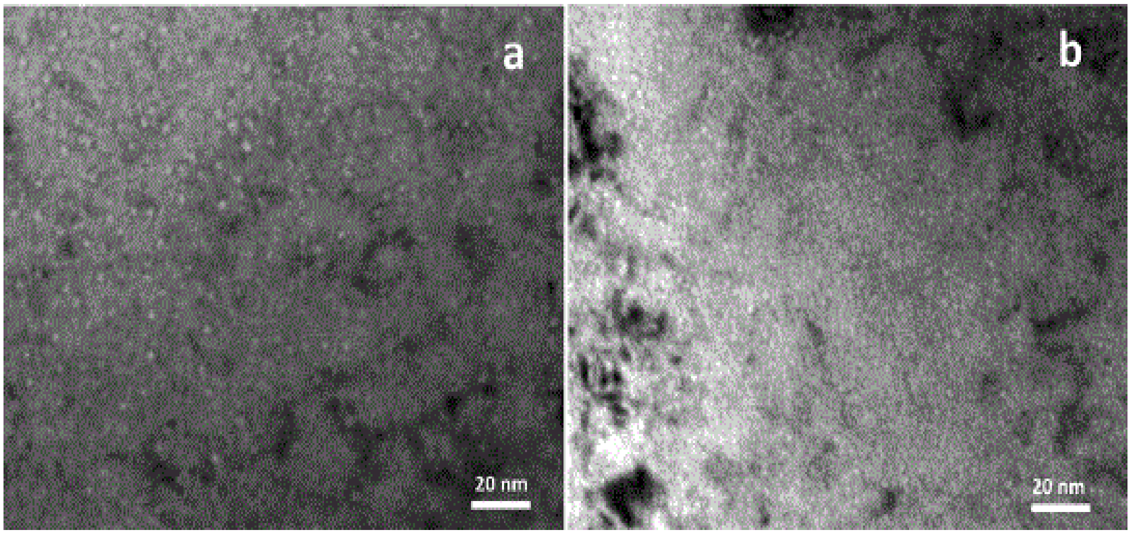

Figure 2.21: TEM micrographs showing cavity microstructures after irradiation to 5.4 dpa at 300 ˚C with (a) 200 appm helium and (b) 5000 appm helium [76].

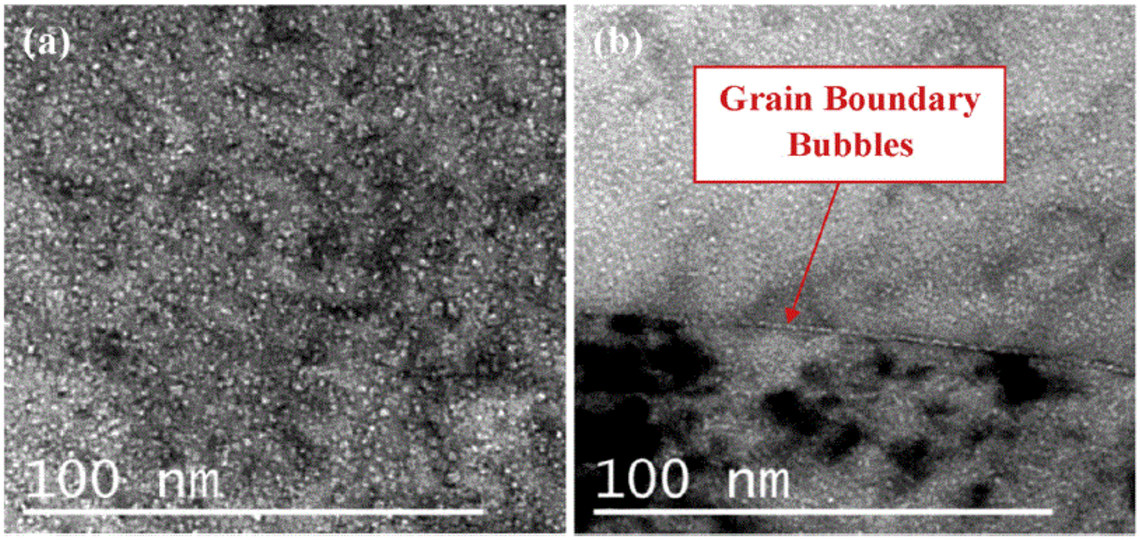

Figure 2.22: Helium bubbles in Inconel X750 imaged in the under focus condition from material at 20 dpa with 6000 appm helium irradiated at 380°C (a) within the grain interior, and (b) aligned along a grain boundary [75].

The hardening associated with cavities/bubbles depends on their relative barrier strength and how they interact with moving dislocations. Cavity size and density/volume fraction along with the internal pressure of the bubbles influences how they impede dislocation motion. It was suggested that alloy hardening associated with bubbles can be estimated using a standard dispersed barrier model proposed by Orowan as the bubbles will pinned the dislocation motion much like precipitates. Knapp et al [77] support this theory by implanting Ni with 1–5at. % He at room temperature and 200°C, producing a highly damaged layer with He bubbles of approximately 1 nm in diameter. Subsequent nano-indentation testing indicated that the hardness of implanted sample was 7 times higher than the un-implanted samples.

MD simulations on pure Ni [78] suggest a critical void size where a transition from small voids with weak barrier strengths into larger voids with stronger barrier strengths. This critical void size was found to be 2 nm. The leading dislocation will pass through small voids < 2 nm in a straight manner, while it will bow substantially when entering the void >2 nm in size and thus pinned as shown in Figure 2.23. Consequently, trailing dislocation is temporarily repelled and thus the energy required for the trailing dislocation to bypass the cavity increases. This is reflected in the rapid increase of stress required for the dislocation to detach from the larger voids and continue its motion shown in Figure 2.23. For the Inconel X-750 components studied here, the critical bubble size may be slightly different since this model was developed for voids in pure Ni, but it serves as a good approximation.

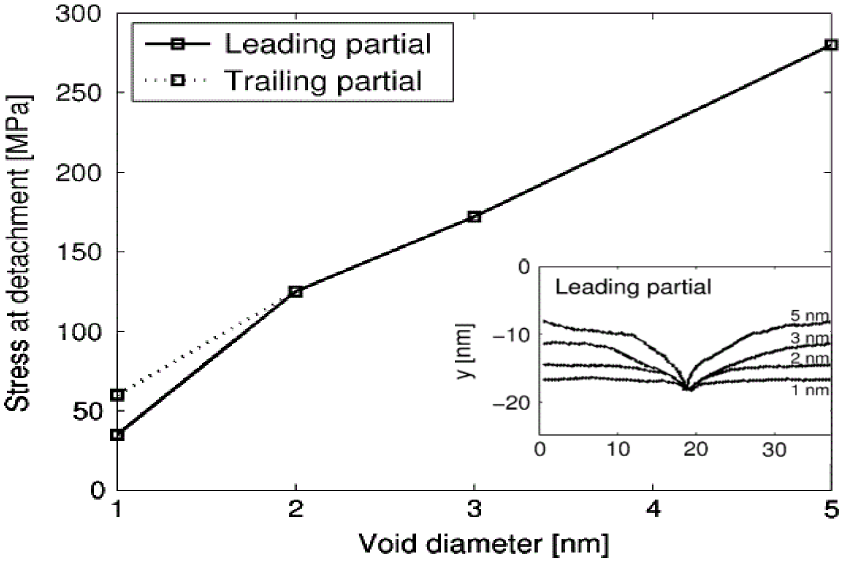

Figure 2.23: the applied shear stress needed to detach a dislocation from a void in pure Ni as a function of void diameter and the amount of bowing in the leading dislocation that initially encounters the void [78].

2.7 Micro/Nano mechanical testing

2.7.1 Nano-indentation hardness test

Nanoindentation tests measure the hardness and the elastic modulus of a specimen while only indenting it to a Nano or micron scale depth. This technique was specifically developed for probing the mechanical properties of samples that have a small volume. Therefore, nanoindentation is the ideal quick and robust mechanical testing technique used to study the effect of ion irradiations since the damaged layer extend only few microns beneath the surface [22]. Nanoindentation has been proven to accurately profile ion irradiated zones of material and the transition interface between irradiated and non-irradiated material where injected interstitials sit, in good agreement with SRIM software [79]. Several examples have been reported the potential of this technique for testing ion-irradiated materials [62,75,79,80].

A micro-indentation hardness test involves pressing a sharp-tipped, pyramidal shaped indenter into the test material a certain depth. The test ends by reducing the indentation force allowing the sample to elastically push the indenter, this distance is the elastic indentation depth, h_e. These tests usually include partial unloading during the indentation cycle. Through testing of the force-depth data at an unloading, the plastic depth, h_p, has been approximated as:

$$h_p = h_t - \frac{h_e}{2} \tag{2-15}$$

where h_e is the elastic depth and h_t is loaded depth as illustrated in Figure 2.24-a [81]. The area, A_p, of the indentation, projected normal to the indentation direction, can be calculated from h_p, which for a perfect three-sided pyramidal “Berkovich” indenter, is given as:

$$A_p = \pi . tan^2 \alpha . {h_p}^2 = 24.5{h_p}^2 \tag{2-16}$$

where α =70.32° and represent the effective semi-angle of the conical indenter equivalent to the Berkovich [82]. The area function of an actual indenter will be affected by a certain amount of indenter tip rounding causing A_p to typically be expressed by a higher order function of h_p. In this case $A_p(h_p)$ is determined experimentally by performing indentations on a standard of well-known hardness, such as quartz or sapphire. The area function in conjunction with the force allows the indentation hardness, H, to be calculated as:

$$H = \frac{P}{A_p(h_p)} \cong \frac{P}{24.5{h_p}^2} \tag{2-17}$$

During micro-indentation hardness studies, it is important to realize that the volume of the sample that is plastically deforming, and hence contributing to the calculated hardness value, extends significantly deeper than the actual indentation. This makes it critical to be able to determine the actual depth of the plastic zone beneath the indenter. K. L. Johnson [83] analyzed the size of the plastic zone beneath an axisymmetric conical indentation

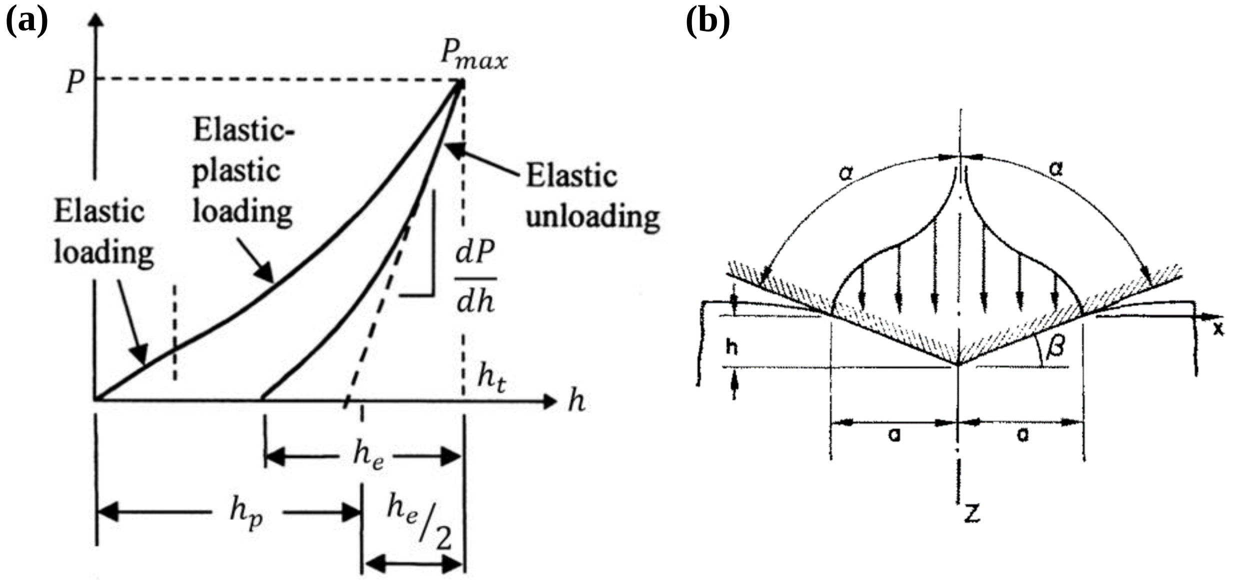

Figure 2.24: (a) Indentation force, P, versus indentation depth, h, for an elastic-plastic specimen [81], (b) Geometry of an axisymmetric conical indentation used to calculate the relationship between the indentation plastic zone radius "c" and the indentation width "a" [83].

made in an isotropic non-hardening material and determined that the plastic zone radius, c, was related to the indentation width, a, as:

$$\frac{c}{a} = \left[\frac{E_R \tan\alpha}{6\sigma_y(1-\nu)} + \frac{2}{3}\left(\frac{1-2\nu}{1-\nu}\right)\right]^{1/3} \quad (2\text{-}18)$$

where ν is the Poisson's ratio, σ_y is the yield stress, α is the apex angle of the indenter (Figure 2.24-b) [83], and E_R is the reduced elastic modulus which introduced because the indenter is not a perfectly rigid body. Therefore, E_R is the combination of the elastic moduli of the indenter head and the indented sample and is determined by [82,84]:

$$\frac{1}{E_R} = \frac{(1-\nu^2)}{E} + \frac{(1-\nu'^2)}{E'} \quad (2\text{-}19)$$

where ν' and E', and ν and E represent the Poisson's ratio and elastic modulus of the indenter and the sample respectively.

Considerable study has been made upon the relationship between H and the yield stress, σ_y, of the indented material. Tabor reported that the hardness of the majority of common metals was approximately $3\sigma_y$ and subsequent more detailed studies of specific alloy systems have shown that this relationship holds surprisingly well for the vast majority of ductile metals [85,86].

As mentioned earlier, Nano-indentation test is essential to test ion-irradiated samples, since the high-energy ions only penetrate a few micrometers into the test material.

2.7.2 Micro-beam bending test

Micro-cantilever bending method have been first introduced by Maio and Roberts [87] in 2004 to measure the fracture toughness of a thin chemically vapor deposited tungsten carbide based coating. The method based on machining a pre-notched micro-beam using Focus Ion Beam (FIB) and then loading it to fracture using nano-indenter. Figure 2.25 pictured the pentagonal-cross section beam they used to measure the fracture toughness by:

$$K_{IC} = \sigma_c \sqrt{\pi a} F\left(\frac{a}{b}\right) \qquad \text{(2-20)}$$

where K_{IC} is the fracture toughness, σ_c the fracture stress, *a* is the crack length, and *F(a/b) is* a dimensionless shape factor dependent on cantilever geometry:

$$F\left(\frac{a}{b}\right) = 1.85 - 3.38\frac{a}{b} + 13.24\left(\frac{a}{b}\right)^2 - 23.26\left(\frac{a}{b}\right)^3 + 16.8\left(\frac{a}{b}\right)^4 \qquad \text{(2-21)}$$

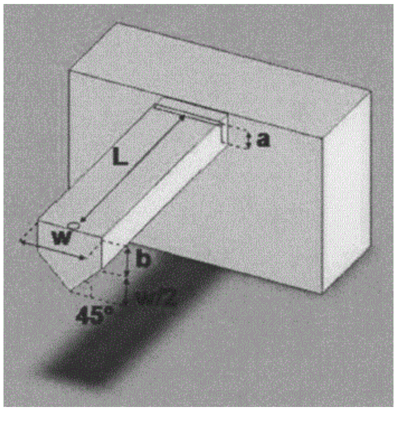

Figure 2.25: Notched pentagonal-shaped micro-cantilever [87]

After that, extensive studies of micro-cantilever beam bending has been performed and demonstrated that micron-scale cantilevers can be used to measure a range of mechanical properties of irradiated and non-irradiated materials in bulk and thin film samples including: elastic modulus [88,89], fracture toughness [90-92], stress corrosion crack in single grain boundaries [93], mechanical properties dependent on grain boundary character [90,92,94] and effect of irradiation on grain boundary embrittlement [89] . Iqbal et al [90] carried out in situ micro-cantilever tests on notched Ni-Al single crystals to investigate the orientation dependence of fracture toughness. Cantilever beams of two crystal directions, {(110) and (100)} of length of 8 µm, width 1.8 µm and thickness of 1.5 µm, were manufactured by FIB milling. A notch was made, also by FIB, at a distance of 2 µm away from the root of the beam. The micro-cantilever tests clearly show the orientation dependency of the fracture toughness since the measured fracture toughness values are found to be 3.52 ± 0.29 MPa $m^{1/2}$ for the (110) and 5.12 ± 0.50 MPa $m^{1/2}$ for the (100) orientations. Armstrong et al [94] used this testing technique to study the effect of small quantities of bismuth on the grain boundary embrittlement of copper. Micro-cantilever beams, containing a single grain boundary with known misorientation (as determined by using EBSD), were tested in bending. The results show that among different oriented grain angles, the high angle boundaries fractured at a lower stress (Figure 2.26). This was correlated with the results from TEM-EDX studies performed to investigate the local chemical composition of four grain boundaries (two which had fractured and two that did not). Bismuth was found at the grain boundaries which had fractured and not at the boundaries which had not fractured (i.e. bismuth segregate at high angle grains).

Micro-cantilevers served useful in investigating the ion irradiated effects on grain boundary embrittlement. Authors in [89] also used FIB fabricated micro cantilever beams to study the fracture behavior of helium and self-similar ion implanted in tungsten. No cantilever fracture was observed in the nonimplanted or the W^+ ion implanted material, however the samples implanted with both helium and tungsten ions were more brittle and exhibited by fracture during loading. This demonstrates the effect of helium accumulation in the grain boundaries. However, SEM examination of nano-indentations in all three conditions showed no cracking or fracture events. This reveal the function of micro-cantilever tests in measuring the micro-fracture properties of ion-implanted layers, which if only studied by indentation would not be observed.

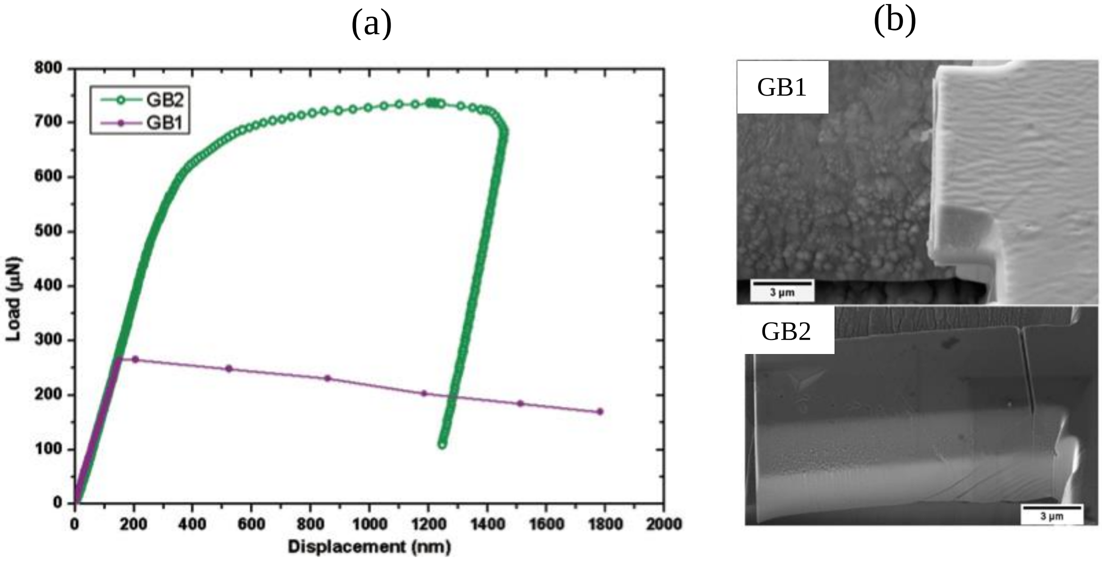

Figure 2.26: (a) Load-displacement curves for two micro-cantilevers. GB_1 fractures at a load of 260 mN, GB_2 yields at a load of 600 mN. (b) Side view of fractured micro-cantilever beam (showing fracture has occurred along the grain boundary) and an unfractured micro-cantilever after testing [94].

2.8 Conclusion

The primary objective of this research is to investigate the effect of heavy ion irradiation and helium implantation on the mechanical properties and the grain boundary strength of Inconel X750 spacer material in CANDU reactor. Descriptions of the theories, mechanisms and techniques which were applied to achieve the objectives were discussed in this chapter along with the results of some example studies performed on X750 and other FCC metals. It's clear from the above literature that most of the studies performed on Inconel X750 was focused mainly upon the effect of irradiation and irradiation temperature on the microstructure evolution. Only few studies correlate these microstructural changes to the onset of decreased ductility. In addition, and to best of my knowledge, no studies have been performed on grain boundary embrittlement of X750. The following chapters include detailed descriptions of all the investigations carried out for this research.

2.9 References

[1] Metals Special Corporation, “INCONEL alloy X750,” pp. 1–28, 2004.

[2] R. C. Reed, *The Superalloys Fundamentals and Applications*. New York: Cambridge, 2006.

[3] M. Griffiths, “The Effect of Irradiatoin on Ni-containing Components in CANDU Reactor Cores: A Review,” *AECL Nucl. Rev.*, vol. 2, no. 1, pp. 1–16, 2013.

[4] G. D. Smith and S. J. Patel, “The role of niobium in wrought precipitation hardened nickel-based alloys,” in *Superalloys*, 2005, pp. 135–154.

[5] A. K. Sinha and J. J. Moore, “Precipitation of M23C6 Carbides in an Aged Inconel X-750,” *Metallography*, vol. 98, pp. 87–98, 1986.

[6] M. Dagan, “3D Field Ion Microscopy and Atom Probe Tomography Techniques for the Atomic Scale Characterisation of Radiation Damage in Tungsten,” University of Oxford, 2016.

[7] “ASTM E521-16, Standard Practice for Investigating the Effects of Neutron Radiation Damage Using Charged-Particle Irradiation, ASTM International, West Conshohocken, PA”, 2009.

[8] D. J. Bacon, A. F. Calder, F. Gao, V. G. Kapinos, and S. J. Wooding, “Computer simulation of defect production by displacement cascades in metals,” *Nucl. Instruments methods Phys. Res. B*, vol. 102, pp. 37–46, 1995.

[9] R. E. Stoller, M. B. Toloczko, G. S. Was, A. G. Certain, S. Dwaraknath, and F. A. Garner, “On the use of SRIM for computing radiation damage exposure,” *Nucl. Instruments Methods Phys. Res. Sect. B*, vol. 310, pp. 75–80, 2013.

[10] G. H. Kinchin and R. S. Pease, “The Displacement of Atoms in Solids by Radiation,” *Reports Prog. Phys.*, vol. 18, no. 1, pp. 1–51, 1955.

[11] G. S. Was, *Fundamentals of radiation materials science*. Springer, 2007.

[12] H. Ullmaier, “Radiation Damage in Metallic Materials,” *MRS Bull.*, vol. 22, no. 4, pp. 14–21, 1997.

[13] M. I. Norgett, M. T. Robinson, and I. M. Torrens, “Proposed method of calculating displacement dose rates,” *Nucl. Eng. Des.*, vol. 33, pp. 50–54, 1975.

[14] L. E. Rehn, “Production of freely-migrating,” *J. Nucl. Mater.*, vol. 174, pp. 144–150, 1990.

[15] M. Li, M. A. Kirk, P. M. Baldo, D. Xu, and B. D. Wirth, “Study of defect evolution by TEM with in situ ion irradiation and coordinated modeling,” *Philos. Mag.*, vol. 92, no. 16, pp. 2048–2078, 2012.

[16] S. J. Zinkle and L. L. Snead, “Opportunities and limitations for ion beams in radiation effects studies : Bridging critical gaps between charged particle and neutron irradiations,” *Scr. Mater.*, vol. 143, pp. 154–160, 2018.

[17] G. S. Was *et al.*, “Emulation of reactor irradiation damage using ion beams,” *Scr. Mater.*, vol. 88, pp. 33–36, 2014.

[18] D. J. Mazey, “Fundamental aspects of high-energy ion-beam simulation techniques and their relevance to fusion materials studies,” *J. Nucl. Mater.*, vol. 174, pp. 196–209, 1990.

[19] G. S. Was *et al.*, “Emulation of neutron irradiation effects with protons : validation of principle,” *J. Nucl. Mater.*, vol. 300, pp. 198–216, 2002.

[20] N. H. Packan, K. Farrell, and J. O. Stiegler, “Correlation of neutron and heavy ion damage,” *J. Nucl. Mater.*, vol. 78, pp. 143–155, 1978.

[21] D. Kiener, A. M. Minor, O. Anderoglu, Y. Wang, S. Maloy, and P. Hosemann, “Application of small-scale testing for investigation of ion-beam-irradiated materials,” *J. Mater. Res.*, vol. 27, no. 21, pp. 2724–2736, 2012.

[22] P. Hosemann, C. Shin, and D. Kiener, “Small scale mechanical testing of irradiated materials,” *J. Mater. Res.*, vol. 30, no. 9, pp. 1231–1245, 2015.

[23] B. N. Singh, “Effect of grain size on void formation during high -energy electron irradiation of austenitic stainless steel,” *Philos. Mag.*, vol. 29, no. 8, pp. 25–42, 1974.

[24] O. Engler and V. Randle, *Introduction to texture analysis*. Taylor & Francis, 2010.

[25] V. Randle, H. Davies, and I. Cross, “Grain boundary misorientation distributions,” *Curr. Opin. Solid State Mater. Sci.*, vol. 5, no. 1, pp. 3–8, 2001.

[26] R. E. Reed-Hill, *Physical metallurgy principles*. New York: Van Nostrand, 1973.

[27] M. D. Sangid, H. Sehitoglu, H. J. Maier, and T. Niendorf, “Grain boundary characterization and energetics of superalloys,” *Mater. Sci. Eng. A*, vol. 527, no. 26, pp. 7115–7125, 2010.

[28] G. E. Dieter, *Mechanical metallurgy*. New York;Montreal: McGraw-Hill, 1988.

[29] P. Lejček, *Grain boundary segregation in metals*. Verlag Berlin Heidelberg:

Springer, 2010.

[30] W. T. Read and W. Shockley, “Dislocation model of crystal grain boundary,” *Phys. Rev.*, vol. 78, no. 3, pp. 275–289, 1950.

[31] J. M. Burgers, “Geometrical considerations concerning the structural irregularities to be assumed in a crystal,” *Proceeding Phys. Soc.*, vol. 52, 1940.

[32] M. L. Kronberg and F. H. Wilson, “Secondary recrystallization in copper,” *Jom*, vol. 1, no. 8, pp. 501–514, 1949.

[33] D. G. Brandon, “The structure of high-angle grain boundaries,” *Acta Metall.*, vol. 14, pp. 1479–1484, 1966.

[34] F. . Weinberg, “Grain boundaries in metals,” *Prog. Met. Phys.*, vol. 8, pp. 105–128, 1959.

[35] F. J. Humphreys and M. Hatherly, *Recrystallization and related annealing phenomena*, 2nd Editio. Elsevier, 2004.

[36] D. L. Olmsted, E. A. Holm, and S. M. Foiles, “Survey of computed grain boundary properties in face-centered cubic metals-II: Grain boundary mobility,” *Acta Mater.*, vol. 57, no. 13, pp. 3704–3713, 2009.

[37] T. Skidmore, R. G. Buchheit, and M. C. Juhas, “Grain boundary energy vs. misorientation in Inconel® 600 alloy as measured by thermal groove and OIM analysis correlation,” *Scr. Mater.*, vol. 50, no. 6, pp. 873–877, 2004.

[38] H. Mehrer, *Diffusion in solids*. Springer, 2007.

[39] L. E. Murr, *Interfacial phenomena in metals and alloys*. Addison-Wesley Pub. Co, 1975.

[40] J. J. Kai, F. R. Chen, and T. S. Duh, “Effects of Grain Boundary Misorientation on Radiation-Induced Solute Segregation in Proton Irradiated 304 Stainless Steels,” *Mater. Trans.*, vol. 45, no. 1, pp. 40–50, 2004.

[41] R. Monzen, O. Matsuda, and H. Miura, “Misorientation dependence of intergranular embrittlement of Cu – 2 . 0 wt .% Sb bicrystals,” *Mater. Sci. Eng. A*, vol. 389, pp. 424–427, 2004.

[42] S. Watanabe, Y. Takamatsu, N. Sakaguchi, and H. Takahashi, “Sink effect of grain boundary on radiation-induced segregation in austenitic stainless steel,” *J. Nucl. Mater.*, vol. 283–287, pp. 152–156, 2000.

[43] C. M. Barr *et al.*, “Grain boundary character dependence of radiation-induced

segregation in a model Ni – Cr alloy," *J. Mater. Res.*, vol. 30, no. 9, pp. 1290–1299, 2015.

[44] A. F. Rowcliffe, L. K. Mansur, D. T. Hoelzer, and R. K. Nanstad, "Perspectives on radiation effects in nickel-base alloys for applications in advanced reactors," *J. Nucl. Mater.*, vol. 392, no. 2, pp. 341–352, 2009.

[45] T. S. Duh, J. J. Kai, F. R. Chen, and L. H. Wang, "Effects of grain boundary misorientation on the solute segregation in austenitic stainless steels," *J. Nucl. Mater.*, vol. 258–263, pp. 2064–2068, 1998.

[46] M. Tomozawa, Y. Miyahara, and K. Kako, "Solute segregation on Σ3 and random grain boundaries in type 316L stainless steel," *Mater. Sci. Eng. A*, vol. 578, pp. 167–173, 2013.

[47] W. Z. Han, M. J. Demkowicz, E. G. Fu, Y. Q. Wang, and A. Misra, "Effect of grain boundary character on sink efficiency," *Acta Mater.*, vol. 60, pp. 6341–6351, 2012.

[48] T. Watanabe, T. Murakami, and S. Karashima, "Misorientation dependance of grain boundary segregation," *Scr. Metall.*, vol. 12, pp. 361–365, 1978.

[49] R. Monzen, T. Kuze, T. Okamoto, and H. Miura, "Bismuth Embrittlement of [011] Twist Boundaries in Copper Bicrystals," *Metall. Mater. Trans. A*, vol. 30A, pp. 483–485, 1999.

[50] D. E. J. Armstrong, C. D. Hardie, J. S. K. L. Gibson, A. J. Bushby, P. D. Edmondson, and S. G. Roberts, "Small-scale characterisation of irradiated nuclear materials: Part II nanoindentation and micro-cantilever testing of ion irradiated nuclear materials," *J. Nucl. Mater.*, vol. 462, pp. 374–381, 2015.

[51] H. Zhang *et al.*, "Cavity morphology in a Ni based superalloy under heavy ion irradiation with hot pre-injected helium . II," *J. Appl. Phys.*, vol. 115, 2014.

[52] C. D. Judge *et al.*, "Intergranular fracture in irradiated Inconel X-750 containing very high concentrations of helium and hydrogen," *J. Nucl. Mater.*, vol. 457, pp. 165–172, 2015.

[53] C. D. Judge *et al.*, "Embrittlement of nickel alloys in CANDU reactor environment," *25th Int. Symp. Radiat. Eff. Mater. ASTM, Anaheim, California, USA*, vol. 25, pp. 161–175, 2012.

[54] F. A. Garner, L. R. Greenwood, E. R. Gilbert, and M. Griffiths, "Impact of Ni-59 (N, α) and (N, P) reactions on DPA rate, heating rate, gas generation and stress relaxation in LMR, LWR and candu® reactors," in *Proc. Fourteenth Intern. Conf. on Environmental Degradation of Materials in Nuclear Power Systems Water Reactors, Virginia Beach, Virginia, USA*, pp. 1344–1354, 2009.

[55] L. R. Greenwood and F. A. Garner, “Hydrogen generation arising from the 59Ni(n, p) reaction and its impact on fission-fusion correlations,” *J. Nucl. Mater.*, vol. 233–237, pp. 1530–1534, 1996.

[56] L. R. Greenwood, “A new calculation of thermal neutron damage and helium production in nickel,” *J. Nucl. Mater.*, vol. 115, pp. 137–142, 1983.

[57] J. D. Hunn, E. H. Lee, T. S. Byun, and L. K. Mansur, “Helium and hydrogen induced hardening in 316LN stainless steel,” *J. Nucl. Mater.*, vol. 282, pp. 131–136, 2000.

[58] K. L. Murty, “Role and significance of source hardening in radiation embrittlement of iron and ferritic steels,” *J. Nucl. Mater.*, vol. 270, pp. 115–128, 1999.

[59] R. S. Nelson, J. A. Hudson, and D. J. Mazey, “The stability of precipitates in an irradiation environment,” *J. Nucl. Mater.*, vol. 44, no. 3, pp. 318–330, 1972.

[60] E. Camus, C. Abromeit, F. Bourdeau, N. Wanderka, and H. Wollenberger, “Evolution of long-range order and composition for radiation-induced precipitate dissolution,” *Phys. Rev. B*, vol. 54, no. 5, pp. 3142–3150, 1996.

[61] H. E. K. Zhang, Z. Yao, M. A. Kirk, and M. R. Daymond, “Stability of Ni 3 (Al , Ti) Gamma Prime Precipitates in a Nickel- Based Superalloy Inconel X-750 Under Heavy Ion Irradiation,” *Metall. Mater. Trans. A*, vol. 45A, pp. 3422–3428, 2014.

[62] J. D. Hunn, E. H. Lee, T. S. Byun, and L. K. Mansur, “Ion-irradiation-induced hardening in Inconel 718,” *J. Nucl. Mater.*, vol. 296, pp. 203–209, 2001.

[63] N. Hashimoto, J. D. Hunn, T. S. Byun, and L. K. Mansur, “Microstructural analysis of ion-irradiation-induced hardening in inconel 718,” *J. Nucl. Mater.*, vol. 318, pp. 300–306, 2008.

[64] F. Carsughi, H. Derz, P. Ferguson, G. Pott, W. Sommer, and H. Ullmaier, “Investigations on Inconel 718 irradiated with 800 MeV protons,” *J. Nucl. Mater.*, vol. 264, pp. 78–88, 1999.

[65] R. Schaublin, Z. Yao, N. Baluc, and M. Victoria, “Irradiation-induced stacking fault tetrahedra in fcc metals,” *Philos. Mag.*, vol. 85, no. 4–7, pp. 769–777, 2005.

[66] S. J. Zinkle, *Radiation-Induced Effects on Microstructure*, 1st ed. Elsevier Inc., 2012.

[67] D. Hull and D. J. Bacon, *Introduction to Dislocations*, Fifth Edit. Elsevier, 2011.

[68] H. K. Zhang, Z. Yao, M. R. Daymond, and M. A. Kirk, “Elevated temperature irradiation damage in CANDU spacer material,” *J. Nucl. Mater.*, vol. 445, pp. 227–234, 2014.

[69] M. Kiritani, “Story of stacking fault tetrahedra,” *Mater. Chem. Phys.*, vol. 50, pp. 133–138, 1997.

[70] H. Ken, Z. Yao, C. Judge, and M. Griffiths, “Microstructural evolution of CANDU spacer material Inconel X-750 under in situ ion irradiation,” *J. Nucl. Mater.*, vol. 443, pp. 49–58, 2013.

[71] H. K. Zhang, Z. Yao, G. Morin, and M. Griffiths, “TEM characterization of in-reactor neutron irradiated CANDU spacer material Inconel X-750,” *J. Nucl. Mater.*, vol. 451, pp. 88–96, 2014.

[72] K. Farrell, P. J. Maziasz, E. H. Lee, and L. K. Mansur, “Modification of radiation damage microstructure by helium,” *Radiat. Eff.*, vol. 78, pp. 277–295, 1983.

[73] M. A. Stopher, “The effects of neutron radiation on nickel-based alloys,” *Mater. Sci. Technol.*, vol. 33, no. 5, pp. 518–536, 2017.

[74] J. J. Kai and G. L. Kulcinski, “14 MeV nickel-ion irradiated HT-9 ferritic steel with and without helium pre-implantation,” *J. Nucl. Mater.*, vol. 175, pp. 227–236, 1990.

[75] C. D. Judge *et al.*, “The effects of proton irradiation on the microstructural and mechanical property evolution of inconel X-750 with high concentrations of helium,” *J. Nucl. Mater.*, vol. 492, pp. 213–226, 2017.

[76] H. Zhang *et al.*, “Cavity morphology in a Ni based superalloy under heavy ion irradiation with cold pre-injected helium . I,” *J. Appl. Phys.*, vol. 115, 2014.

[77] J. A. Knapp, D. M. Follstaedt, and S. M. Myers, “Hardening by bubbles in He-implanted Ni,” *J. Appl. Phys.*, vol. 103, 2008.

[78] A. Simar, H. L. Voigt, and B. D. Wirth, “Molecular dynamics simulations of dislocation interaction with voids in nickel,” *Comput. Mater. Sci.*, vol. 50, pp. 1811–1817, 2011.

[79] P. Hosemann, J. G. Swadener, D. Kiener, G. S. Was, S. A. Maloy, and N. Li, “An exploratory study to determine applicability of nano-hardness and micro-compression measurements for yield stress estimation,” *J. Nucl. Mater.*, vol. 375, pp. 135–143, 2008.

[80] P. Changizian, A. Brooks, Z. Yao, and M. R. Daymond, “Nano-scale Mechanical Properties and Microstructure of Irradiated X-750 Ni-Based Superalloy,” *Metall. Mater. Trans. A*, vol. 49, pp. 498–514, 2018.

[81] A. . Fischer-Cripps, “A review of analysis methods for sub-micron indentation testing,” *Vacuum*, vol. 58, pp. 569–585, 2000.

[82] A. . Fischer-Cripps, “Critical review of analysis and interpretation of nanoindentation test data,” *Surf. coatings Technol.*, vol. 200, pp. 4153–4165, 2006.

[83] K. L. Johnson, “The correlation of indentation experiments,” *J. Mech. Phys. Solids*, vol. 18, pp. 115–126, 1970.

[84] W. C. Oliver and G. M. Pharr, “An improved technique for determining hardness and elastic modulus using load and displacement sensing indentation experiments,” *J. Mater. Res.*, vol. 7, no. 6, pp. 1564–1583, 1992.

[85] J. T. Busby, M. C. Hash, and G. S. Was, “The relationship between hardness and yield stress in irradiated austenitic and ferritic steels,” *J. Nucl. Mater.*, vol. 336, no. 2–3, pp. 267–278, 2005.

[86] D. Tabor, “The physical meaning of indentation and scratch hardness,” *Br. J. Appl. Phys.*, vol. 7, pp. 159–166, 1956.

[87] D. Di Maio and S. G. Roberts, “Measuring fracture toughness of coatings using focused-ion-beam-machined microbeams,” *J. Mater. Res.*, vol. 20, no. 2, pp. 299–302, 2005.

[88] D. E. J. Armstrong, A. J. Wilkinson, and S. G. Roberts, “Measuring anisotropy in Young ’ s modulus of copper using microcantilever testing,” *J. Mater. Res.*, vol. 24, no. 11, pp. 3268–3276, 2009.

[89] D. E. J. Armstrong, C. D. Hardie, J. S. K. L. Gibson, A. J. Bushby, P. D. Edmondson, and S. G. Roberts, “Small-scale characterisation of irradiated nuclear materials: Part i - Microstructure,” *J. Nucl. Mater.*, vol. 462, pp. 374–381, 2015.

[90] F. Iqbal, J. Ast, M. Göken, and K. Durst, “In situ micro-cantilever tests to study fracture properties of NiAl single crystals,” *Acta Mater.*, vol. 60, no. 3, pp. 1193–1200, 2012.

[91] D. E. J. Armstrong, A. J. Wilkinson, and S. G. Roberts, “Measuring anisotropy in Young’s modulus of copper using microcantilever testing,” *J. Mater. Res.*, vol. 24, no. 11, pp. 3268–3276, 2009.

[92] A. Stratulat, D. E. J. Armstrong, and S. G. Roberts, “micro mechanical measurment of fracture behaviour of individual grain boundaries in Bi alloy 600 exposed to a pressurized water reactor enviroment,” *Corros. Sci.*, vol. 104, pp. 9–16, 2016.

[93] D. E. J. Armstrong, M. E. Rogers, and S. G. Roberts, “Micromechanical testing of stress corrosion cracking of individual grain boundaries,” *Scr. Mater.*, vol. 61, pp. 741–743, 2009.

[94] D. E. J. Armstrong, A. J. Wilkinson, and S. G. Roberts, “Micro-mechanical measurements of fracture toughness of bismuth embrittled copper grain boundaries,” *Philos. Mag. Lett.*, vol. 91, no. 6, pp. 394–400, 2011.

Chapter 3

3 Ni^+ and He^+ implantation effects on the hardness and microstructure of heat-treated Inconel X750

In this chapter, the effect of sole Ni^+ and He^+ implantation on the stability of the strengthening phase γ' and the mechanical properties of X750 was investigated. Heat-treated and solution annealed samples were implanted at 25°C with different dose levels and then tested by nanoindentation technique. SEM and TEM were utilized to examine the stability of γ' precipitates.

3.1 Introduction

Helical spring annulus gas spacers are used in CANDU nuclear reactors to maintain an insulating gas gap between the pressure tube and the calandria tube within the fuel channels. There are over one thousand such spacers in a CANDU reactor core. The spacers are made of the heat-treated nickel-based Inconel X750 alloy. In its heat-treated state this alloy is strengthened by both incoherent precipitates (TiC, NbC, and $Cr_{23}C_6$) and coherent ordered $Ni_3(Al,Ti)$ γ'precipitates and retains its strength and creep resistance at elevated temperature due to the high thermal stability of the γ' precipitates. High energy particle, ion or neutron, irradiation has been observed to destabilize γ' precipitates [1-5]. The temperature dependence of this destabilization is unusual in that γ' precipitates appear to become disordered during low temperature neutron irradiation but remain stable during high temperature neutron irradiation [1,6-8].

In addition to irradiation-induced disordering/dissolution of the γ' phase, Inconel X750 is subject to significant helium accumulation when exposed to thermal neutron flux via the $^{59}Ni(n,\alpha)^{56}Fe$ transmutation process. The accumulated helium concentration within Inconel X750 annulus gas spacers can reach approximately C_{He} = 40,000 appm by the end of its service life in a CANDU nuclear reactor [9]. The effect of accumulated helium on promoting hardening and embrittlement of metals is well established and is correlated to the formation of cavities/bubbles at grain boundaries and at precipitate/matrix interfaces

[9-14]. Examination of ex-service spacers removed from CANDU rectors, indicate differences in helium cavity/bubble size depending upon irradiation temperature. The cavities are larger, and distributed primarily along grain boundaries, when the spacers are irradiated at elevated temperature (between 260°C-310°C) compared to when they are irradiated at lower temperature (60°C) [9,10,15,16].

Concurrent neutron irradiation and helium accumulation appears therefore to induce both a *hardening* and a *softening* effect on heat-treated Inconel X750 by forming crystal defects and helium nanocavities while simultaneously disordering/dissolving the γ' phase. The nuanced contribution of simultaneous irradiation-induced hardening, phase destabilization, and helium accumulation remains a subject of ongoing examination and is far from being completely understood. Here we report results of a study, involving Ni^+ and He^+ implantation at 25°C, as a surrogate for neutron irradiation, to investigate the contribution of the mechanisms of concurrent softening, due to γ' phase destabilization, and hardening, due to ion-induced crystal damage and accumulated helium, of the Inconel X750 alloy. We undertake this study by performing nanoindentation hardness testing and SEM/TEM microstructural assessments on ion-implanted Inconel X750 in the solution annealed (SA) and heat-treated (HT) conditions.

3.2 Experimental procedure

3.2.1 Materials

Table 3-1 indicates the chemical composition of the Inconel X750 alloy used in this study. The alloy was received in the heat treated (HT) condition which consisted of solution annealing at 1010°C (30 minutes) followed by air-cooling to room temperature, 18% cold work, and then aging at 728°C (16 hours). Samples (6 x 6 x 3 mm) were cut by EDM from HT X750 material. Some samples were then reheated by solution annealing at 1010°C for 22 hours to remove the heat-treated microstructure. These are referred to as the SA samples. The specimens were then mechanically ground followed by polishing with an aqueous slurry of 0.02 μm colloidal SiO_2.

Table 3-1: Chemical composition (weight percent) of the Inconel X750 alloy used in this study [15].

Inconel	Ni	Cr	Fe	Nb	Co	Mn	Cu	Al	Ti	Si	C
X-750	70	14.0-17.0	5.0-9.0	0.7-1.2	1.0	1.0	0.5	0.4-1.0	2.25-2.75	0.5	0.08

3.2.2 Ion implantation

Ion implantations were performed at 25°C on the polished HT and SA samples with a high-current tandem ion accelerator at the University of Western Ontario, London, Ontario Canada. Sequential helium implantation was performed with He^+ ions at fourteen kinetic energy levels, from 0.3 to 1.6 MeV, to ensure uniform helium concentration to a depth of about 3 μm (Figure 3.1-a). The ion beam exposure was controlled to achieve average helium concentrations of C_{He} = 100, 1000, and 5000 appm.

Another set of Inconel X750 samples (HT and SA) were Ni^+ implanted at 25°C to invoke levels of irradiation damage up to ψ = 5 dpa (displacements per atom) without significantly changing the chemical composition of the Ni-based alloy. Sequential Ni^+ implantations were performed at thirteen kinetic energy levels, from 2.0 to 8.0 MeV, to invoke uniform irradiation damage over a depth of about 3 μm (Figure 3.1-b). The Ni^+ exposure was controlled to achieve calculated average ψ levels of 0.1, 0.5, 1.0 and 5.0 dpa.

The Stopping Range of Ions in Matter (SRIM-2013) software, was used to calculate the average implanted ion depth and the average ion-induced crystal damage ψ using the Kinchin-Pease approximation [17] with threshold displacement energy of 40 eV and 0 eV lattice binding energy for Ni as discussed in Chapter 2. Table 3-2 Lists the levels of ψ and C_{He} and the corresponding He^+ and Ni^+ implantation dosages for all specimens studied.

Table 3-2: He^+ and Ni^+ implantation conditions used in this study along with ion mixing parameter K. All ion implantations were performed at 25°C on Inconel X750 samples in the heat-treated (HT) and solution annealed (SA) conditions.

	Sample Identification	Implanted He^+ ($Ions/cm^2$)	Implanted Ni^+ ($Ions/cm^2$)	C_{He} (appm)	ψ_{ion} (dpa)	K ($Å^5/eV$)	comments
Non-Implanted	HT1 & SA1	0	0	0	0		
He^+ implanted samples	HT2 & SA2	$2.05 x 10^{14}$	0	100	0.0002		
	HT3 & SA3	$2.06 x 10^{15}$	0	1000	0.002		
	HT4 & SA4	$1.03 x 10^{16}$	0	5000	0.012		-Slight softening -No super lattice -Re-agglomeration
Ni^+ implanted samples	HT5 & SA5	0	$1.5 x 10^{15}$	0	0.1	15	Softened
	HT6 & SA6	0	$7.4 x 10^{15}$	0	0.5	15	-Softened -No superlattice
	HT7 & SA7	0	$1.5 x 10^{16}$	0	1.0	17	-Re-hardening(20%) -No super lattice -Re-agglomeration
	HT8 & SA8	0	$7.4 x 10^{16}$	0	5.0	28	Saturated hardness

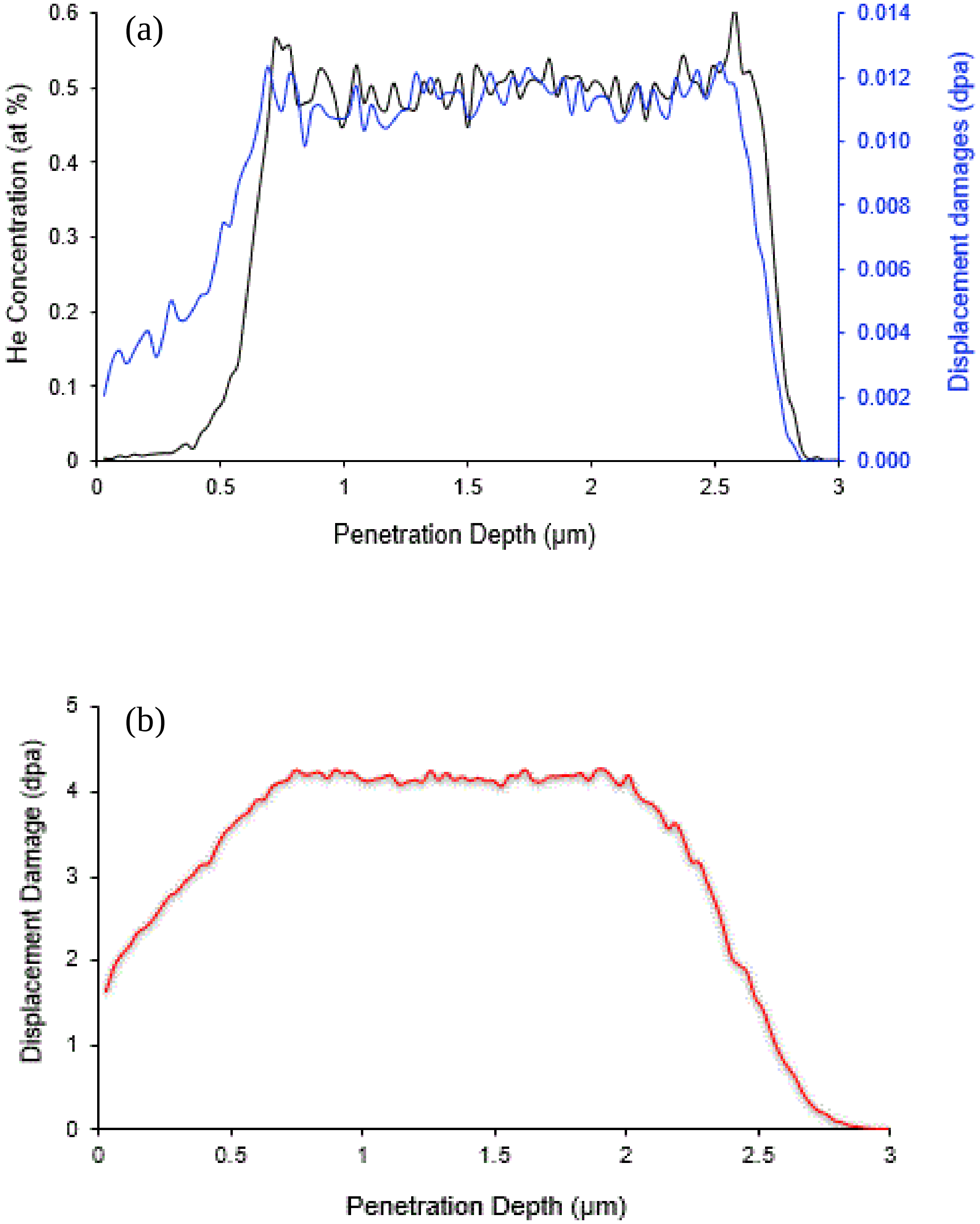

Figure 3.1: The profile of helium concentration (C_{He} = 5000appm) and Ni^+ ion-induced atomic displacement damage (ψ =1dpa) resulting from (a) fourteen consecutive He^+ ion implantation energies (E_{He+} = 0.3 - 1.6 MeV) and (b) Ni^+ ion implantations energies (E_{Ni+} = 2.0 – 8 MeV).

3.2.3 Electron microscopy

Samples selected for microstructural analysis by SEM were lightly sputter polished/etched with low energy (10 keV) Cs^+ ions. This revealed the grain structure and, when imaged with high-resolution back-scattered electrons, contrast features consistent with the presence of γ' precipitates.

TEM foils were produced from the ion-implanted samples using the focused ion beam (FIB) lift-out procedure. The foils were thinned to electron transparency with a 5 keV Ga^+ ion beam, and the average foil thickness was measured by EELS and found to be 76nm. TEM characterization was performed at the Canadian Centre for Electron Microscopy Hamilton, Ontario, Canada with a 200 keV Joel 2010F TEM/STEM. Energy dispersive x-ray analysis and selected area electron diffraction was used to assess the ion-induce crystallographic damage, γ' precipitates, and helium micro-cavities in the samples. TEM micrographs were taken close to [011] and [001] the zone axis [1,23].

3.2.4 Indentation hardness testing

Nanoindentation hardness testing was used to assess the effect of He^+ and Ni^+ implantation on the mechanical strength of the Inconel X750. Hardness tests were performed on two perpendicular planes, Planes (i) and (ii), of each sample (Figure 3.2-a).This allowed a precise assessment of how the hardness changed within the 3 μm implanted region of the test samples. Both planes were flat and polished (0.02μm colloidal SiO_2).Plane (i) was polished prior to ion implantation. Plane (ii) was prepared after implantation by cutting the sample, normal to the implanted surface, with a slow-speed diamond saw, depositing a Cu layer to prevent edge deflection during the indentation test, and then polishing (Figure 3.2b)

Nanoindentation hardness tests were performed with a Nano-Test indentation testing platform (Micro Materials Ltd, Wrexham UK) with a diamond Berkovich indenter, at a constant indentation loading rate of $\dot{F} = 1\,mN/s$ to optimize the performance of the nanoindenter; that is, providing the best balance between test duration and indentation depth precision. All indentation tests performed in this study were made to a plastic indentation depth of h = 200nm. The indentation hardness H was calculated using Eq.2-17.

Hardness testing on Plane (i) consisted of an array of 20 indents each spaced 25 μm apart to ensure that the plastic zones of individual indentations did not overlap. Hardness tests on Plane (ii) were performed in two paths; rows of 15 indents beginning on the irradiated edge and proceeding diagonally into the sample, and row of 15 indents on the irradiated edge. In this way the hardness was measured at precisely controlled locations and the variation of hardness through the 3 μm ion-implanted zone could be assessed.

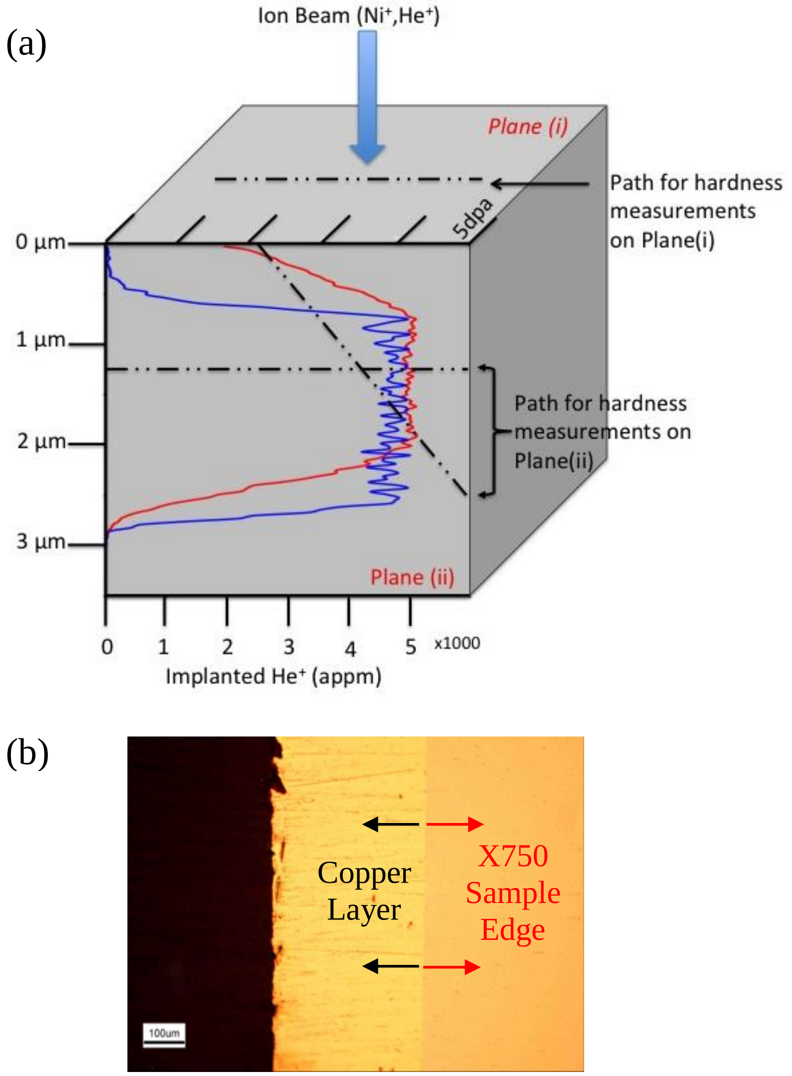

Figure 3.2: (a) Schematic illustration of the three paths along which indentation hardness measurements were performed on the ion implanted samples. Superimposed on this illustration are the implanted helium content (appm, blue line) and ion-induced damage (dpa, red line) as a function of depth into the sample. (b) Plane (ii) with Cu layer deposited on the sample edge to promote edge retention during polishing.

3.3 Results and discussion

In this study we are interested in delineating the effect of ion-implantation damage ψ and implanted helium concentration C_{He} on the hardness and microstructure of Inconel X750. Since previous studies suggest that ψ has the complex effect of both destabilizing the γ' precipitates while simultaneously increasing the hardness due to accumulated irradiation damage. We investigate the effect of ψ and C_{He} on the hardness of X750 in both the HT, containing abundant coherent γ' precipitates, and the SA, containing very few coherent γ' precipitates, conditions.

3.3.1 The microstructure of non-irradiated Inconel X750

The HT Inconel X750 had a microstructure consisting of equiaxed grains of FCC matrix material (Figure 3.3-a). The average grain size was about 20μm with a maximum grain size of about 45μm. Twins and large precipitates were observed in the microstructure (Figure 3.3, b-c). The large precipitates, about 2μm in size, were analyzed by EDX as being rich in Ti and Nb and are therefore MC carbides (Ti,Nb)C. TEM observation revealed additional smaller, nanometer size, Cr-rich precipitates typical of $M_{23}C_6$ type carbides (Figure 3.3-d). γ' precipitates $Ni_3(Al,Ti)$ were observed in the HT X750 samples by SEM operating in high-magnification back-scattered electron imaging mode (Figure 3.4). The chemical difference of the γ' precipitates relative to the surrounding matrix generated atomic mass contrast, visible with back scattered electron imaging, along with small topographical roughness, associated with differential Cs^+ ion sputtering rate associated with the compositional variation. The HT samples displayed a uniform distribution of small γ' precipitates while the SA samples displayed significantly fewer γ' precipitates. TEM micrographs, along with selected area diffraction patterns close to zone axis [001] and [011] along with diffraction spot intensity profiles, are shown for the non-irradiated HT and SA material in Figure 3.4. Super-lattice diffraction reflections, arising from the ordered γ' precipitates, are present in the HT samples but not in the SA samples. STEM and EDX elemental mapping of the non-irradiated material shows the chemical composition and morphology of γ' precipitates in the HT samples as being enriched in Ti and Al with the average precipitate diameter of about 22 nm.

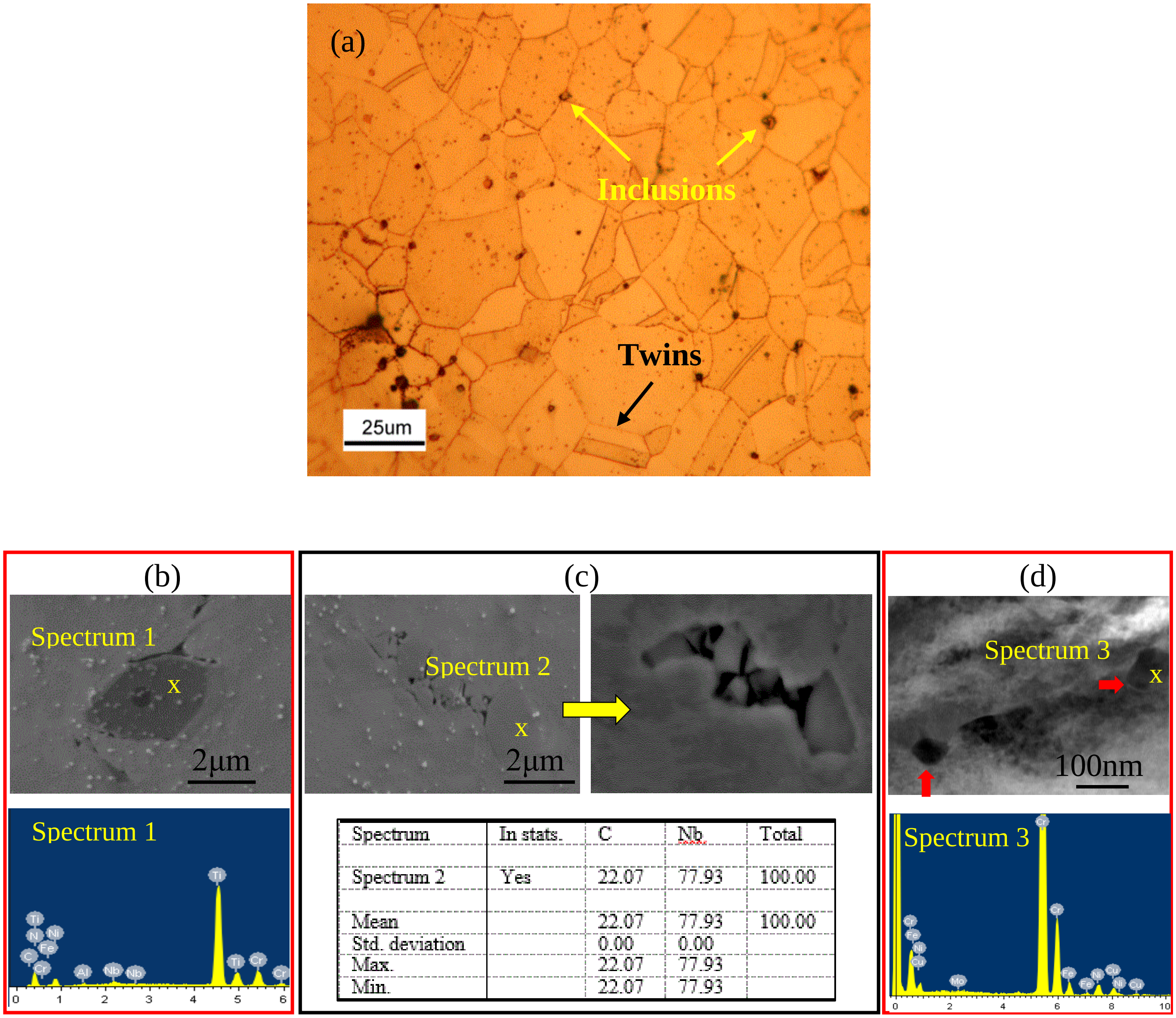

Spectrum	In stats.	C	Nb	Total
Spectrum 2	Yes	22.07	77.93	100.00
Mean		22.07	77.93	100.00
Std. deviation		0.00	0.00	
Max.		22.07	77.93	
Min.		22.07	77.93	

Figure 3.3: (a) Optical micrograph of a chemically etched sample of the Inconel X750 alloy (HT condition). (b) SEM image of a large inclusion known as MC carbides (Ti,Nb)C with EDX map shows their enrichment with Ti and Nb. (c) SEM image shows stringers inclusion. (d) TEM micrograph reveals nanometer size precipitate known as $M_{23}C_6$ type carbides rich with Cr (90%).

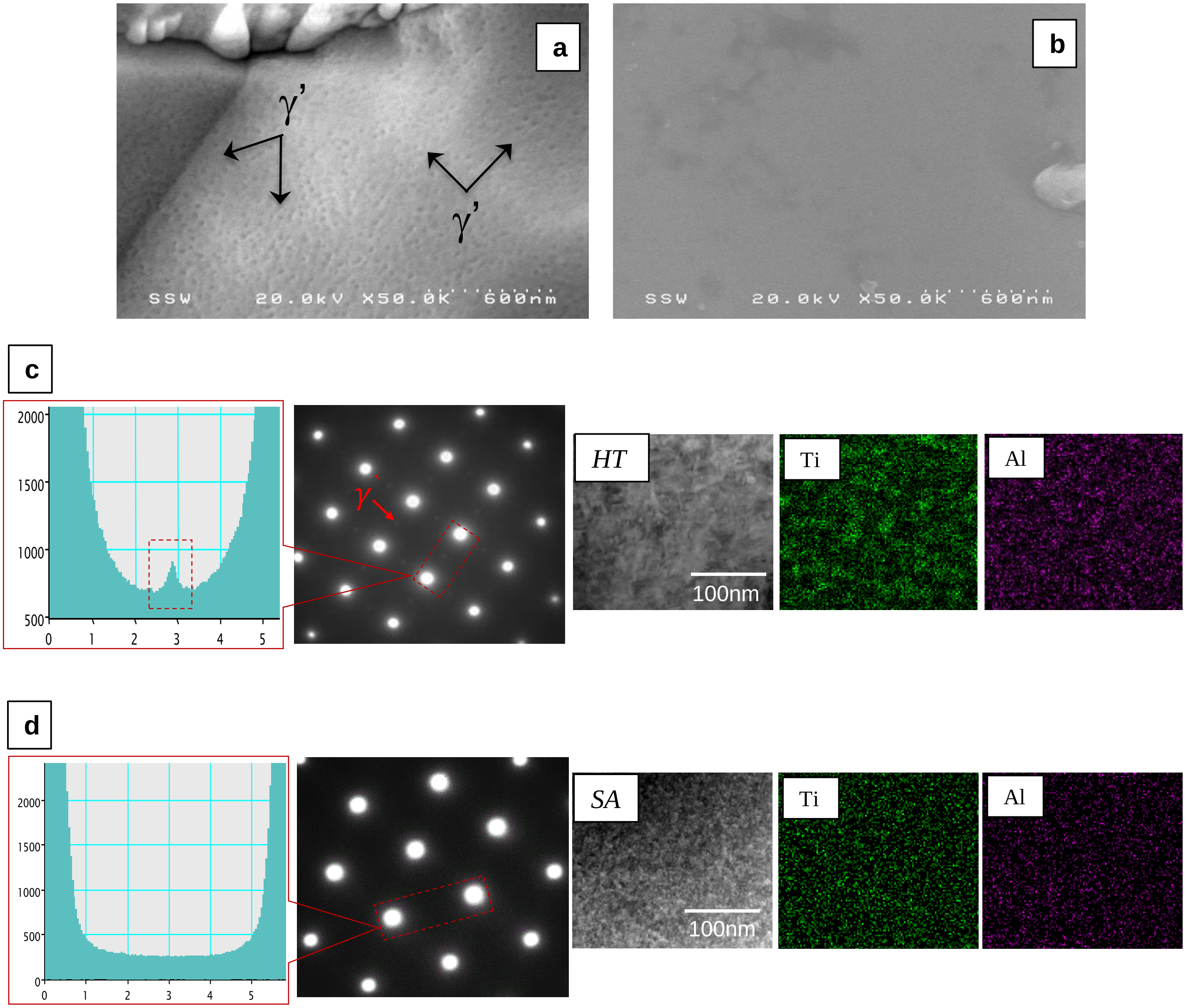

Figure 3.4: Back-scattered (20 keV) scanning electron micrographs of lightly Cs^+ sputtered surfaces showing γ′ precipitate availability in the non-irradiated: (a) heat-treated (HT) and (b) solution annealed (SA) samples. TEM micrograph with selected area diffraction spot close to zone axis: (c) [001] for HT sample and (d) [011] SA sample along with intensity profile.

3.3.2 Effect of irradiation damage ψ on the hardness H of Inconel X750

Plots of H versus ψ for the Inconel X750 alloy in the HT and SA conditions are shown in Figure 3.5. The plots include hardness data from tests performed on Planes (i) and (ii). Hardness values from either plane revealed quantitatively similar trends indicating that similar hardness information can be obtained by performing indentation tests on either plane provided sufficiently shallow (h = 200 nm) indentations and multi-energy ion implantations are used.

In the non-implanted state, the Inconel X750 alloy was considerably harder in the HT compared to the SA condition. This is of course consistent with a higher density of γ' precipitates in the heat-treated condition (Figure 3.4). The average hardness value, measured from Plane (i), was 7.16 GPa for HT and 5.72 GPa for SA X750.

The Inconel X750 alloy, in both the HT and the SA conditions, displayed generally increasing hardness with increasing ψ. However, a perturbation in this trend occurs in the early implantation stages, between ψ = 0.0 and 0.5 dpa when the hardness drops by about 30% and 2% for the HT and the SA samples. Interestingly, the hardness at 0.5 dpa is very close in magnitude to that of non-implanted SA sample (Figure 3.5, a-b) indicating nearly complete dissolution of the γ' precipitates at ψ = 0.5 dpa. The indentation hardness then increases steadily with increasing ψ beyond 0.5 dpa. Nano-indentation hardness values presented in this study for low doses (i.e. ψ = 0.1 and 0.5 dpa) are similar to previously reported findings on Inconel X750 [18,19] and other Ni superalloys [20].

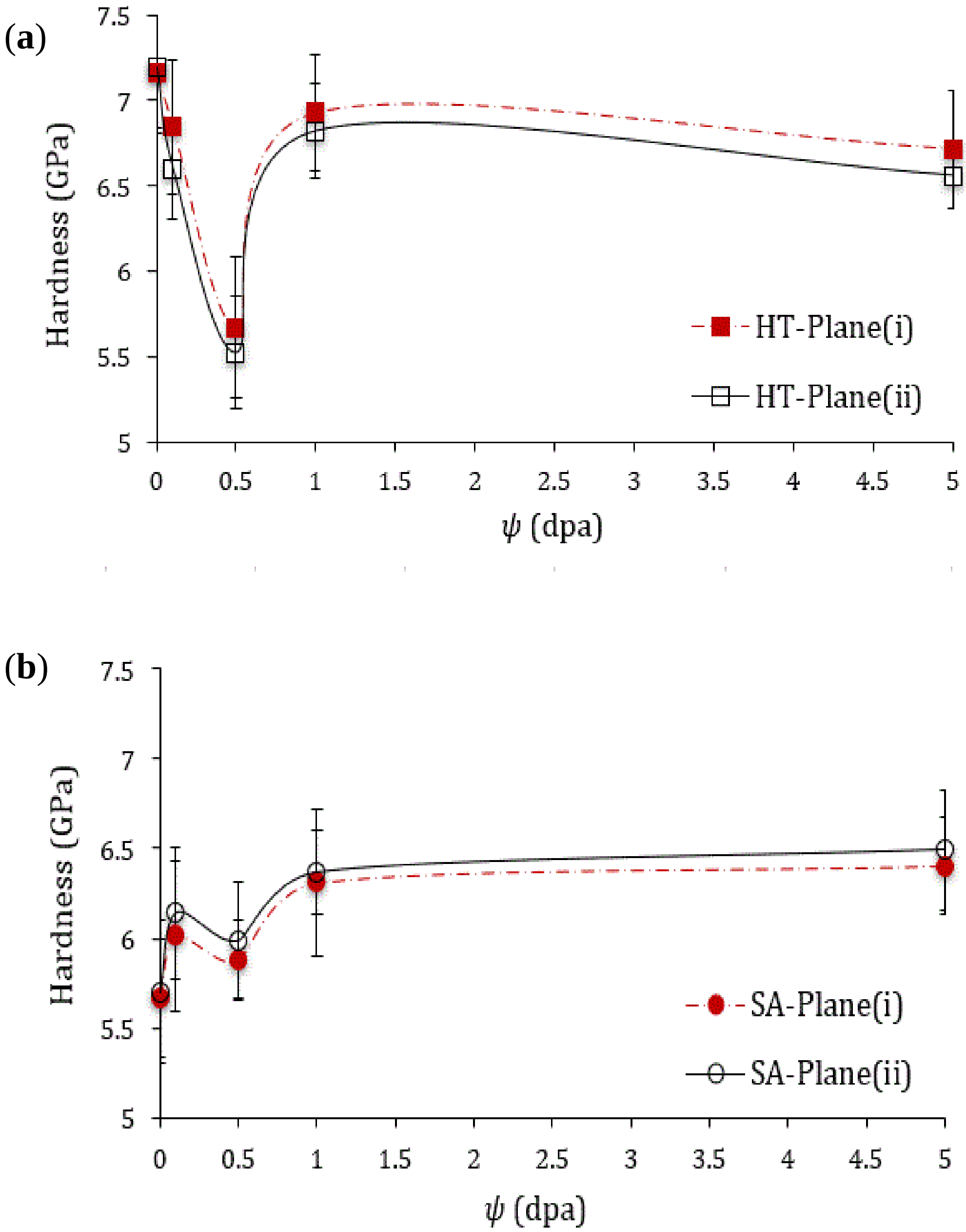

Figure 3.5: Average indentation hardness H versus ion irradiation damage *ψ* for the Inconel X750 samples in the (a) HT and (b) SA conditions. The graphs show trends for hardness measurements performed on Planes (i) and (ii). Error bars represent the measurement of the amount of variation of hardness data.

TEM and back-scattered SEM analysis of the Ni^+ implanted surface identified the cause of the observed softening to be the disordering/dissolution of the γ' precipitates. Figure 6-a shows TEM electron diffraction patterns, and the intensity profile across the diffraction spots, for the HT X750 implanted with ψ = 0.5 and 1 dpa compared to those from the non-implanted condition. The γ' super-lattice reflections disappear at ψ = 0.5 and 1dpa, indicating that γ' disordering has occurred. Figure 3.6-a shows EDX mappings of γ' precipitates in the, ψ = 0.0, 0.5, and 1.0 dpa conditions. Agglomeration of Ti and Al were observed in the non-implanted sample (Figure 3.6-a, row 1). At ψ = 0.5 dpa (Figure 3.6-a, row2), considerable local chemical composition change has occurred with significant diffusion of Ti and Al atoms into the γ matrix indicating that the γ' precipitates are being dissolved. At the higher implantation level, ψ = 1 dpa (Figure 3.6-a, row3), a re-formation of Ti/Al rich regions are observed but in a disordered state (i.e. no super-lattice diffraction spots arise). Similar formation of precipitates at ψ = 1 dpa was previously reported, under similar ion implantation conditions (dose and temperature), in other Ni superalloys [2,21]. This is also supported by our high-resolution back scattered SEM images which show a uniform distribution of dark-light atomic mass contrast for the ψ =1dpa sample but significantly less atomic mass contrast for the ψ= 0.5 dpa sample (Figure 3.6, b-c). These observations confirm that the softening of the Inconel X750 exposed to low level Ni^+ implantation (ψ = 0.5 dpa, Figure 3.5) is due to the loss of coherency of the γ' precipitates and this is in agreement with previously reported findings [1,18-20,22]. Our observation that the percentage decrease in hardness during the initial Ni^+ implantation stage is larger for the HT than for the SA X750 sample is consistent with the fact that the Inconel X750 has significantly less γ' phase present in the SA compared to the HT condition. The increase in indentation hardness that occurs when $\psi > 0.5$ dpa results from both: i) continuous increase in ion-induced crystal damage with increasing ψ and ii) re-formation of Al/Ti rich regions (precipitates) which, while being incoherent, still harden the alloy.

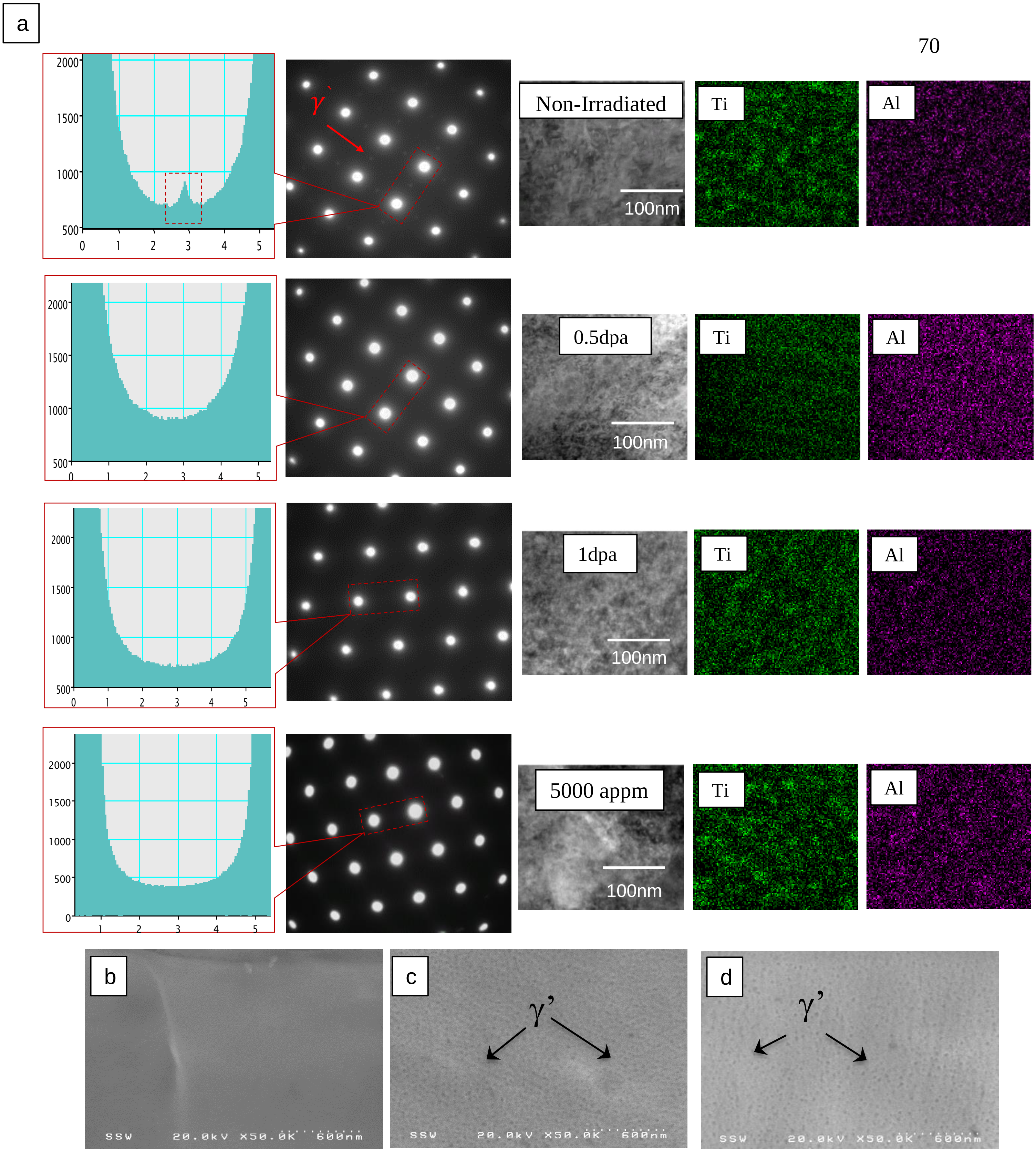

Figure 3.6: (a) Bright field TEM micrograph close to zone axis [001]for non-irradiated HT and 0.5dpa irradiated condition, and [011] for 1 dpa and 5000 appm samples, in conjunction with SADP and intensity profile along with EDX analysis showing elemental mapping and morphology of γ′ precipitate. The non-irradiated TEM images were repeated here for comparison purpose. Back-scattered SEM images of lightly Cs^+ sputtered surface of (b) 0.5 dpa, (c) 1 dpa, and (d) 5000 appm samples.

3.3.3 Effect of accumulated helium on the hardness of Inconel X750

Figure 3.7 indicates that the hardness of the Inconel X750 (HT and SA) increases continuously with increasing helium concentration. This is consistent with previous reports on the effect of implanted helium on increasing indentation hardness of pure Ni production of helium nano-/micro-cavities which act as obstacles to dislocation glide [13]. TEM analysis of our He^+ implanted (C_{He} = 5000 appm) HT sample also indicated the presence of a uniform distribution of He nano-cavities (Figure 3.8). Unlike the Ni^+ implanted samples (Figure 3.5), no perturbation in the H versus C_{He} trend was observed suggesting that He^+ implantation, at least up to C_{He} = 1000 appm, has no effect on the stability of the coherent γ' precipitates. In the case of the HT samples, slight softening occurs between C_{He} = 1000 and 5000appm. SRIM calculation indicates that He^+ implantation to C_{He} = 5000 appm induced small amounts of atomic displacement (ψ = 0.012dpa, Figure 3.1-a). This small amount of ψ is sufficient to disorder the γ' precipitate and thus result in the observed slight decrease in hardness. This assessment is supported by our data for the X750 in the SA condition which display no softening at C_{He} = 5000 appm (Figure 3.7) and by diffraction pattern analysis which indicates the disappearance of the γ' phase super-lattice reflections for the HT X750 at C_{He} = 5000 appm (Figure 3.6-a (row4)). Similar observations were reported previously, at lower C_{He} = 2000 appm, for He^+ implanted Inconel 718 [20,23].

We observe however that EDX mapping indicates that Al/Ti rich regions remain in the HT X750 sample at C_{He} = 5000 appm. We thus deduce that the small, ψ = 0.012dpa, level of ion-induced atomic displacement associated with C_{He} = 5000 appm He^+ implantation is sufficient to disorder the γ' precipitates but not to completely redistributed the Ti and Al back into the matrix. In other words, the γ' precipitates are made incoherent, but their presence still results in significant hardening. This is also supported by the high-resolution back-scattered SEM image of helium implanted HT X750 samples (C_{He} = 5000appm) which show regions of atomic-mass contrast (Figure 3.6-d).

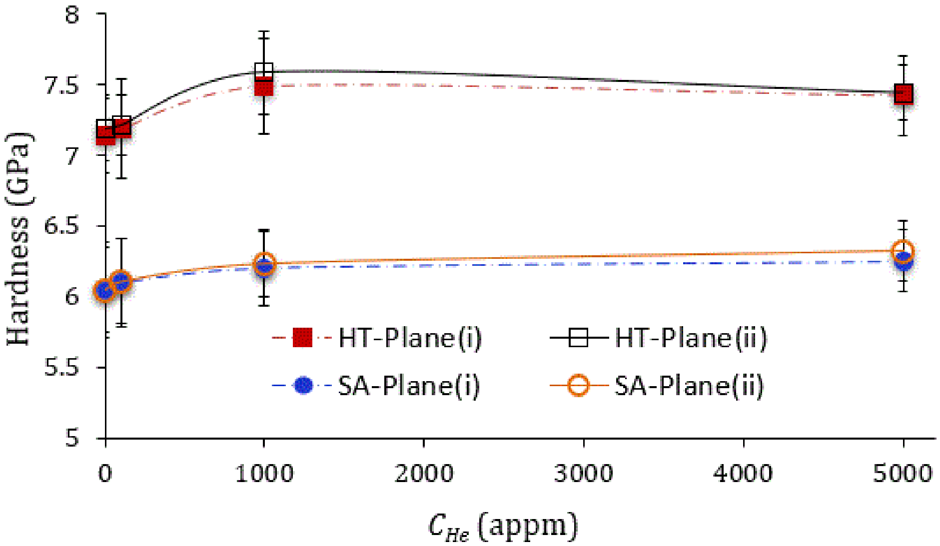

Figure 3.7: Average indentation hardness H versus accumulated helium content C_{He} for the Inconel X750 samples in the HT and SA conditions. The graphs show trends for hardness measurements performed on planes (i) and (ii). Error bars represent the measurement of the amount of variation of hardness data.

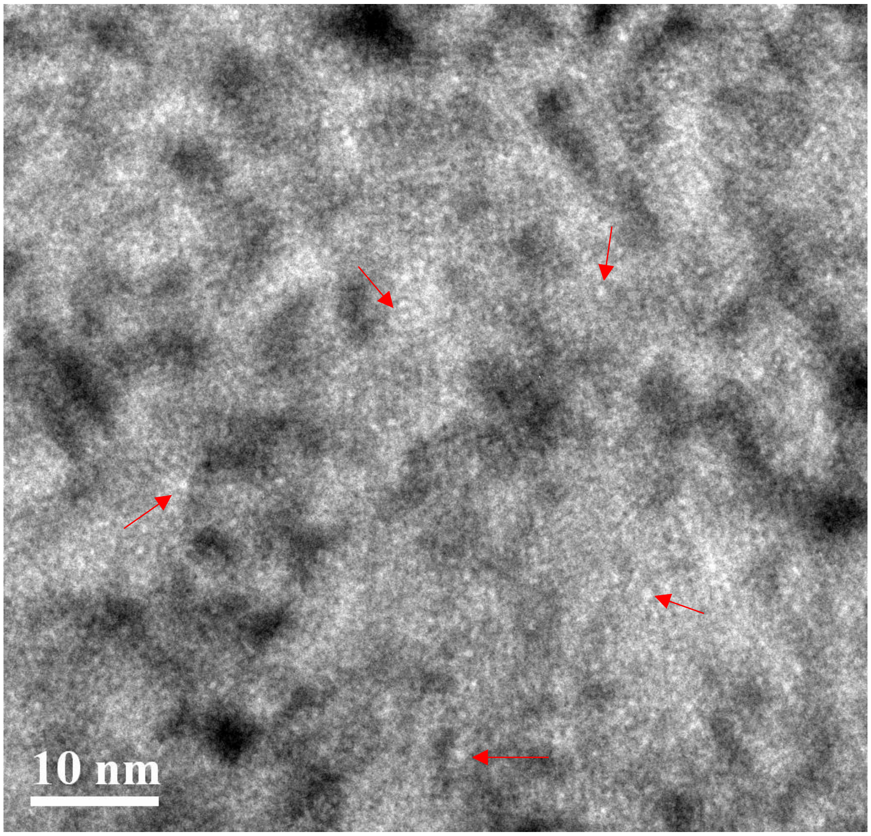

Figure 3.8: High magnification TEM image of nano-cavities formed by helium implantation at 25°C in to X750 at C_{He} = 5000appm.

3.3.4 The effect of Ni^+ and He^+ induced mixing on precipitate phase stability

The hardness testing and microstructural characterization presented in this paper provide information on how Ni^+ and He^+ implantation, and by association neutron-induced crystal damage and accumulated helium transmutation products, affect both precipitate stability and the irradiation-/helium-induced hardening in heat-treated Inconel X750. Since both Ni^+ and He^+ implantation invokes atomic displacement, with Ni^+ implantation causing significantly higher levels of ψ than He^+ implantation (Table 3-2), we can illustrate the effect of both types of implantation on a single plot of H versus log(ψ) (Figure 3.9). This plot is informative since data from both He^+ and Ni^+ implantation follow the same trend displaying a localized softening between ψ = 0.1 and 1.0dpa. Here we will consider the driving force for this localized softening to be the ion-induced atomic mixing and its effect on disordering the γ' phase.

The coherent γ' precipitates are a metastable microstructural feature arising from rapid cooling from the solution annealing temperature and subsequent thermal aging. Thermal energy resulting from ion-induced atomic displacements will provide energy to destabilize the coherent γ' precipitates causing them to first become disordered, and thus lose crystallographic coherency, and then dissolve. Previous studies of X750 have proposed that the γ' phase becomes disordered because of ion-atom collision mixing alone [1,18]. In experiments such as those performed here ion-induced displacement cascades arise from both collision mixing and thermal mixing due to localized temperature spikes associated with the implantation process. This situation can be described in terms of a γ/γ' interface mixing parameter (K) as [24]:

$$K = \frac{D_{mix}t}{\emptyset F_D} = \left(\frac{D_t}{\emptyset F_D}\right)_{collision} + \left(\frac{D_t}{\emptyset F_D}\right)_{thermal\,spike} \qquad (3\text{-}1)$$

where t is the irradiation time, ϕ is the ion fluence and F_D is the damage energy deposited per unit length normal to the specimen surface, as calculated by SRIM. D_{mix} is an intermixing diffusion coefficient. By using t = 1020 s and $\phi = 0.73/\text{Å}^2$, characteristic of ψ

= 0.5 dpa Ni$^+$ implantations performed in this study, along with F_D = 126 eV/Å/ions and D_{mix} = 1.4 Å^2/s [25], K can be approximated as 15 Å^5/eV. Higher K values obtained for higher doses are listed in Table 3-2. Molecular dynamics simulations on the radiation-induced intermixing of a Ni/Ni_3Al interface show that K is 12–20 Å^5/eV [26], which is similar to this approximation and are significantly larger than the K value estimated by a simple collision mixing process, the first term on the RHS of Eq. 3-1 [27]. We can thus conclude that including thermally-induced atomic mixing, due to the thermal spike associated with the ion-implantation process (the second term on the RHS of Eq. 3-1) is key to describing the mixing mechanism contributing to the loss of coherency and ultimately the dissolution of the γ' precipitates in the heat-treated Inconel X750 alloy.

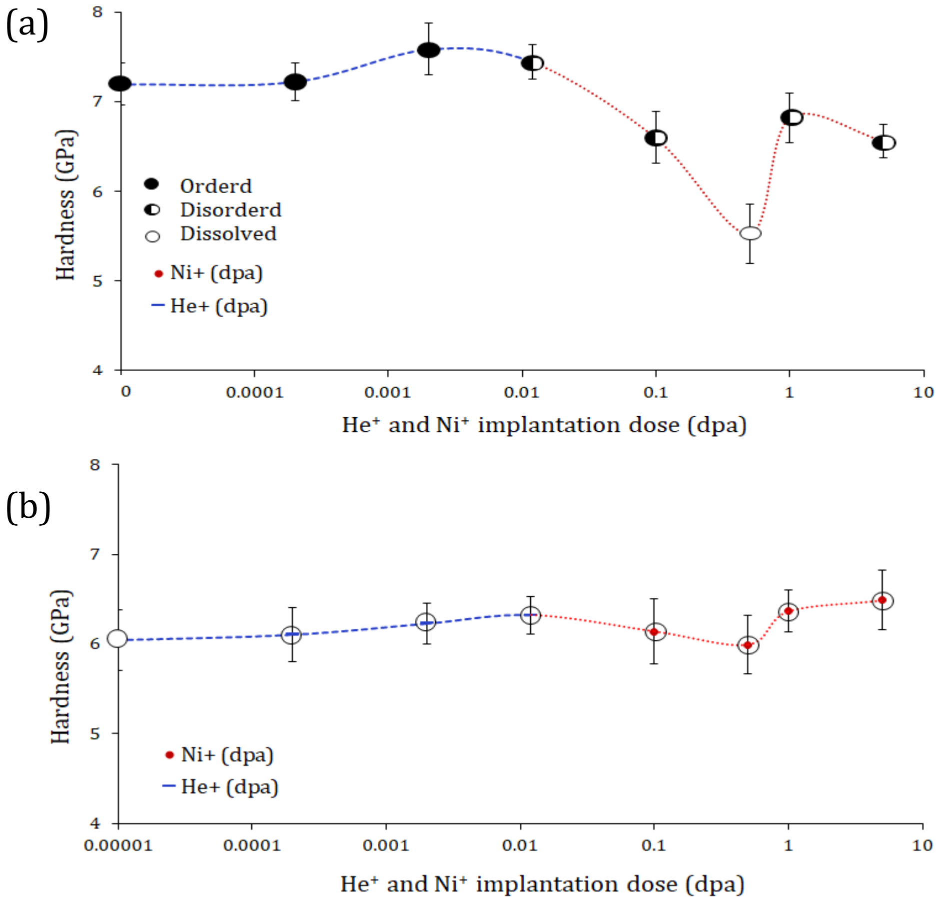

Figure 3.9: Semi-logarithmic plots of average indentation hardness H versus ion irradiation damage ψ implanted with either Ni$^+$ or He$^+$ for (a) HT Inconel X750 and (b) SA Inconel X750. The labelling of the data points as Ordered, Disordered or Dissolved describes the state of the γ' precipitates as determined by SEM/TEM at specific levels of ψ. Error bars represent the measurement of the amount of variation of hardness data.

Reformation of incoherent Ti/Al rich regions (precipitates) within the Inconel X750 matrix at ψ >1 dpa (Figure 3.9) indicates that significant re-ordering, via atomic mixing, occurs which allows the Ti and Al atoms to reposition. In other words, the large super-saturation of point defects produced during ion-implantation can lead to sufficient diffusion via either vacancy-atom exchanges or interstitial-atom movements [28]. This radiation induced re-precipitation is similar to that reported for Ni_3Al, Niomonic PE16, and other Ni alloys [2,4,21,28].

The amount of hardening observed for the He^+ implanted samples is slightly higher, for a given value of ψ (Figure 3.9). TEM images of the ψ = 5000appm sample show a high density of small, uniformly distributed helium nano-cavities, of about 0.7nm average diameter (Figure 3.8). The occurrence of similar distributions of nano-cavities have been previously reported for He^+ implanted nickel [13,29], Inconel 718 [23] and other FCC metals [29-31]. Helium nano-cavities are considered to be weak barriers to dislocation motion and thus are likely the source of this observed small increase in hardness.

Helium-induced hardening of the Inconel X750 alloy in the HT condition was higher than in the SA condition and this may be the result of the lack of γ' precipitates and the low initial dislocation density in the SA samples.

3.4 Conclusion

Nickel and Helium ion implantation-induced hardening and microstructural evolution of Inconel X750 in the heat-treated (HT) and solution annealed (SA) conditions was investigated using nanoindentation hardness testing and electron microscopy (SEM and TEM). Irradiation crystal damage up to ψ = 5 dpa was invoked with Ni^+ implantation while He^+ implantation up to C_{He} = 5000 appm was performed on samples the HT and SA conditions. The X750 alloy displayed generally increasing hardness with increasing Ni^+ implantation damage but a perturbation in the trend occurred when $\psi \leq 0.5$ dpa, and the hardness dropped by about 30% and 2% for the HT and the SA samples respectively. TEM analysis indicated that this softening was associated with disordering and dissolution of the γ′ strengthening phase. The hardening behavior observed at higher implantation damage (ψ =1 dpa) resulted in re-formation of Al/Ti rich regions within the microstructure phase. The hardness of the Inconel X750 increased continuously with increasing implanted He^+ up to C_{He} = 1000 appm. This was associated with the formation of helium bubbles as observed by TEM. Slight drop in hardness in the HT condition at C_{He} = 5000 appm indicated that high levels of He^+ implantation destabilize the γ′ precipitates as was confirmed with TEM observed disappearance of γ′ super-lattice reflections.

3.5 Acknowledgements

The authors wish to acknowledge the assistance of Mr. Jack Hendriks at the Tandetron Ion Accelerator facilities at the University of Western Ontario (London, Ontario, Canada) for his support with performing ion implantations of the Inconel X750 samples. The assistance of Dr. T. Simpson of the University of Western Ontario Nanofabrication Laboratory in preparing the TEM foils is also gratefully acknowledged. The authors offer a special note of thanks to Dr. Carmen Andrei in Canadian Centre for Electron Microscopy at McMaster University for her help with performing the TEM analyses. The assistance of Dr. S. Ramamurthy of Surface Science Western is also gratefully acknowledged. The authors also gratefully acknowledge the financial support of this research by the Natural Science and Engineering Research Council (NSERC) and University Network of Excellence in Nuclear Engineering (UNENE).

3.6 References

[1] H. K. Zhang, Z. Yao, M. A. Kirk, and M. R. Daymond, “Stability of Ni3(Al, Ti) gamma prime precipitates in a nickel-based superalloy inconel X-750 under heavy ion irradiation,” *Metall. Mater. Trans. A Phys. Metall. Mater. Sci.*, vol. 45, no. 8, pp. 3422–3428, 2014.

[2] C.Abromeit, S.Müller, and N.Wanderka, “Stability of γ′ Phase in the Stoichiometric Ni3Al Alloy Under Ion Irradiation,” *Scr. ametallurgica Matererialia*, vol. 32, no. 10, pp. 1519–1523, 1995.

[3] C. Abromeit, H. Wollenberger, S. Matsumura, and C. Kinoshita, “Stability of ordered phases under irradiation,” *J. Nucl. Mater.*, vol. 276, pp. 104–113, 2000.

[4] E. M. Schulson, “The Ordering and Disordering of Solid Solutions Under Irradiation,” *J. Nucl. Mater.*, vol. 83, pp. 239–264, 1979.

[5] W. V. Vaidya, “Modification of the precipitate interface under irradiation and its effect on the stability of precipitates,” *J. Nucl. Mater.*, vol. 83, no. 1, pp. 223–230, 1979.

[6] R. S. Nelson, J. A. Hudson, and D. J. Mazey, “The stability of precipitates in an irradiation environment,” *J. Nucl. Mater.*, vol. 44, pp. 318–330, 1972.

[7] E. Camus, C. Abromeit, F. Bourdeau, N. Wanderka, and H. Wollenberger, “Evolution of long-range order and composition for radiation-induced precipitate dissolution,” *Phys. Rev. B*, vol. 54, no. 5, pp. 3142–3150, 1996.

[8] H. K. Zhang, Z. Yao, G. Morin, and M. Griffiths, “TEM characterization of in-reactor neutron irradiated CANDU spacer material Inconel X-750,” *J. Nucl. Mater.*, vol. 451, pp. 88–96, 2014.

[9] M. Griffiths, “The Effect of Irradiation on Ni-Containing Components in CANDU ® Reactor Cores: A Review,” *AECL Nucl. Rev.*, vol. 2, no. 1, pp. 1–16, 2013.

[10] C. D. Judge *et al.*, “Intergranular fracture in irradiated Inconel X-750 containing very high concentrations of helium and hydrogen,” *J. Nucl. Mater.*, vol. 457, pp. 165–172, 2015.

[11] L.K.Mansur, E.H.Lee, P.J.Maziasz, and A.P.Rowcliffe, “Control of helium effects in irradiated materials based on theory and experiment,” *J. Nucl. Mater.*, vol. 143, pp. 633–646, 1986.

[12] M. A. Stopher, “The effects of neutron radiation on nickel-based alloys,” *Mater. Sci. Technol.*, vol. 33, no. 5, pp. 518–536, 2017.

[13] J. A. Knapp, D. M. Follstaedt, and S. M. Myers, “Hardening by bubbles in He-implanted Ni,” *J. Appl. Phys.*, vol. 103, p. 013518, 2008.

[14] D. J. Edwards, F. A. Garner, S. M. Bruemmer, and P. Efsing, “Nano-cavities observed in a 316SS PWR flux thimble tube irradiated to 33 and 70 dpa,” *J. Nucl. Mater.*, vol. 384, no. 3, pp. 249–255, 2009.

[15] M. Griffiths *et al.*, “Degradation of Ni-alloy Components in CANDU Reactor Cores,” in *16th Int. Conference on Environmental Degradation of Materials in Nuclear Power Systems – Water Reactors, Asheville, North Carolina, USA,August 11-15*, 2013.

[16] H. Zhang, Z. Yao, M. R. Daymond, and M. A. Kirk, “Cavity morphology in a Ni based superalloy under heavy ion irradiation with cold pre-injected helium. I,” *J. Appl. Phys.*, vol. 115, no. 10, 2014.

[17] R. E. Stoller, M. B. Toloczko, G. S. Was, A. G. Certain, S. Dwaraknath, and F. A. Garner, “On the use of SRIM for computing radiation damage exposure,” *Nucl. Instruments Methods Phys. Res. Sect. B*, vol. 310, pp. 75–80, 2013.

[18] P. Changizian, C. Lu, Z. Yao, and L. M. Wang, “Indentation behaviour of ion-irradiated X-750 Ni- based superalloy,” *Philos. Mag. Lett.*, vol. 97, no. 3, pp. 101–109, 2017.

[19] R. J. K. Maisaa N. Tawfeeq, “Effect of Sequential Helium and Nickel Ion Implantation on the Nano-Indentation Hardness of Inconel X750-Submitted,” *J. Nucl. Mater.*, vol. submitted, 2019.

[20] J. D. Hunn, E. H. Lee, T. S. Byun, and L. K. Mansur, “Ion-irradiation-induced hardening in Inconel 718,” *J. Nucl. Mater.*, vol. 296, no. 2001, pp. 203–209, 2008.

[21] F. Bourdeau, C. Abromeit, and H. Wollenberger, “Disordering and dissolution of γ′ precipitates under ion irradiation,” *Phys. Rev. B*, vol. 50, no. 22, pp. 205–211, 1994.

[22] B. H. Sencer *et al.*, “Microstructural evolution of Alloy 718 at high helium and hydrogen generation rates during irradiation with 600-800 MeV protons,” *J. Nucl. Mater.*, vol. 283–287, no. PART I, pp. 324–328, 2000.

[23] N. Hashimoto, J. D. Hunn, T. S. Byun, and L. K. Mansur, “Microstructural analysis of ion-irradiation-induced hardening in inconel 718,” *J. Nucl. Mater.*, vol. 318, pp. 300–306, 2003.

[24] R. S. Averback, D. Peak, and L. J. Thompson, “Ion-Beam Mixing in Pure and in Immiscible Copper Bilayer Systems,” *Appl. Phys. A*, vol. 39, pp. 59–64, 1986.

[25] C. Sun *et al.*, “Chemistry and mechanical properties of Ni-based superalloy Rene N4 under irradiation at room temperature,” *Acta Mater.*, vol. 95, pp. 357–365, 2015.

[26] T. Lee, A. Caro, and M. J. Demkowicz, “Atomistic modeling of radiation-induced disordering and dissolution at a Ni / Ni 3 Al interface,” *J. Mater. Res.*, vol. 30, no. 9, pp. 1456–1463, 2015.

[27] J. L. Klatt, R. S. Averback, and D. Peak, “Ion beam mixing in Ag-Pd alloys,” *Appl. Phys. Lett.*, vol. 55, no. 13, pp. 1295–1297, 1989.

[28] C. Abromeit and V. Naundorf, “Re-ordering of disordered Ni3Al at low temperatures : contribution of mobile interstitials,” *Intermetallics*, vol. 4, no. 6, pp. 441–446, 1996.

[29] W. Jager and J. Roth, “He trapping and bubble formation in Ni, stainless steel 316 and amorphous alloys,” *Nucl. Instruments Methods*, vol. 182/183, pp. 975–983, 1981.

[30] J. D. Hunn, E. H. Lee, T. S. Byun, and L. K. Mansur, “Helium and hydrogen induced hardening in 316LN stainless steel,” *J. Nucl. Mater.*, vol. 282, no. 2–3, pp. 131–136, 2000.

[31] E. H. Lee, J. D. Hunn, T. S. Byun, and L. K. Mansur, “Effects of helium on radiation-induced defect microstructure in austenitic stainless steel,” *J. Nucl. Mater.*, vol. 280, pp. 18–24, 2000.

Chapter 4

4 Effect of sequential helium and nickel ion implantation on the Nano-indentation hardness of Inconel X750

In the previous chapter, sole He^+ and Ni^+ implantations were performed at 25ºC to assess the effect of irradiation on X750 microstructure and concurrent mechanical properties changes. In this chapter, He^+ and Ni^+ ions were sequentially implanted at 25ºC and 200ºC to investigate the effect of irradiation temperature and the combined effect of Ni^+ and He^+ on the indentation hardness of heat-treated Inconel X750 alloy.

4.1 Introduction

Annulus gas helical spring spacers are critical components separating the high temperature pressure tube from the low temperature calandria tube in fuel channels of a CANDU nuclear reactor. These spacers are made from the heat-treated Inconel X750 nickel based alloy and are exposed to very high neutron fluence over their service life. They are thus susceptible to microstructural instability and mechanical property degradation with time [1]. Extensive TEM investigations were recently performed to understand the microstructural evolution of this heat-treated alloy under conditions of high energy ion implantation as a neutron irradiation surrogate. These studies demonstrated that ion implantation induced both disordering of the γ' strengthening phase and production of crystal defect clusters, such as stacking fault tetrahedra and dislocation loops [2,3]. These concurrent processes cause the hardness of the X750 alloy to first decrease with increasing ion implantation, up to about 1.0 ion-induced atomic displacements per atom (dpa), due to disordering of the γ' phase and then increase, with further increasing dpa, as a result of increasing ion-induced crystal defects.

Nickel based alloys are also subject to significant helium accumulation when exposed to thermal neutron irradiation due primarily to the $^{59}Ni(n,\alpha)^{56}Fe$ transmutation process. The helium concentration within Inconel X750 annulus gas spacers can reach approximately 40,000 appm by the end of their service life in a CANDU reactor [1,4]. The effect of accumulated helium on promoting hardening in Ni and Ni-based alloys has been correlated to the formation of cavities/bubbles within grains and at grain boundaries [5,6]. TEM-based studies of helium in X750 have concentrated on characterizing the mechanisms behind the formation of these cavities/voids [7,8,9]; however, very little work has been carried out to directly measure their influence on the mechanical properties of the X750 alloy [10].

While sole ion implantations are necessary to understand the fundamental mechanisms governing the microstructural/mechanical property changes resulting from various types of ion implantation (i.e Ni^+ or He^+), they do not assess the effect of multiple irradiation-induced processes that may be occurring simultaneously in heat-treated alloys, such as Inconel X750, when in nuclear reactor cores. Recent TEM studies have indicated that, while implanted helium is clearly essential in the formation of helium cavities, it may also affect the rate of development of ion-induced γ' phase disordering and, to a smaller extent, the rate of development of ion-induce crystal damage [7,8,11]. In addition, the ion implantation temperature may also significantly affect the rate of ion-induced microstructural changes. For example, helium cavity nucleation was noticed only when He^+ implantation temperature was above 200°C, and γ' precipitate disordering was only observed at relatively low ion implantation temperature of $60^oC \leq T_{imp} \leq 400^oC$ [7,12]. Two studies have investigated the effect of sequential ion-implantation on the indentation hardness of heat-treated Inconel X750, however both studies investigated only limited implantation conditions: Judge et al [11] studied the microstructure and hardness of X750 after sequential proton/ He^+ implantation (40 dpa and 18000 appm) performed at 250°C and 380°C while Changizian et al [13] performed a microstructural analyses on the same alloy subjected to concurrent He^+/Ni^+ implantation (1 dpa and 5000 appm) at 25°C and 400°C. To properly assess the combined effect of ion/neutron-induced phase disordering / crystal damage accumulation and helium accumulation on the hardness of heat-treated Inconel X750, one must perform nanoindentation hardness tests on samples exposed to a wider range of sequential He^+/Ni^+ implantation conditions. This is necessary primarily to determine if the effects of the two types of implantation are independent and additive. This determination will ultimately allow for development of predictive equation to account for concurrent neutron-induced microstructural damage and helium accumulation in in-core components made from heat-treated Inconel X750.

In this work, heat-treated Inconel X750 material is subjected to thirty-two He^+/Ni^+ implantation conditions. Subsequent nanoindentation hardness tests and TEM microstructural analyses are performed on the implanted samples and data are obtained that strengthen our understanding of the interaction of multiple ion-induced mechanisms of γ' phase destabilization, crystal defect accumulation, and helium cavity formation and growth.

4.2 Experimental procedure

4.2.1 Material preparation and ion implantation

The chemical composition of the Inconel X750 is about 70 wt% Ni, 16 wt% Cr, 6 wt% Fe, and 2.5 wt% Ti, with minor additions of Co, Mn, Cu, Al, Si, and C. The alloy was heat-treated by first solution annealing at 1010^{o}C followed by 18% cold working at room temperature and then aging at 728^{o}C for 16 hours. Two sets of eight samples, each of 6 x 6 x 3 mm dimensions, were sectioned from the heat-treated X750 with a slow speed diamond saw. The specimens were then mechanically ground followed by polishing with an aqueous slurry of 0.02μm colloidal SiO_2.

Ion implantations were performed on the polished samples at the Tandetron Ion Accelerator Facility at the University of Western Ontario (London, Ontario). The samples were first implanted with He^+ ions at 25^{o}C to helium concentration levels of C_{He} = 100, 1000 and 5000 appm. This was achieved by performing multiple implantations over a range of He^+ energy from 0.3 MeV to 1.6 MeV to ensure that C_{He} was uniform to a depth of about 3 μm into the samples (Figure 4.1). Nickel ion implantations were then performed on the same samples at temperatures of 25^{o}C and 200^{o}C. The implantations were performed over a range of ion energy from 0.3 to 8.0 MeV to ensure uniform levels of ion-induced atom displacements of ψ = 0.01, 0.1 and 1dpa to a depth of about 3 μm (Figure 4.1) and to overlap the He^+ implanted region. The level of C_{He} and ψ was determined with the SRIM (stopping range of ions in matter) software incorporating the Kinchin-Pease model for ion-atom displacement with the incorporation of a 40 eV atom displacement threshold energy with 0 eV lattice binding energy. The SRIM calculations assume cryogenic implantation, thus the effect of implantation temperature was not captured. Each ion implanted sample contained two regions of different ion exposure. It should be noted that implantation of He^+ resulted in significantly little ψ (i.e. ψ = 0.012dpa when C_{He} = 5000appm) compared with implantation of the larger Ni^+ ions. TEM foils were prepared from selected ion-implanted samples using the focused ion beam (FIB) lift-out procedure using a 30kV Ga^+ ion beam with controllable beam current from 10nA - 50pA. TEM characterization was then performed on the foils with a 200KV instrument at the Canadian Centre for Electron Microscopy (CCEM) at McMaster University, Hamilton Ontario.

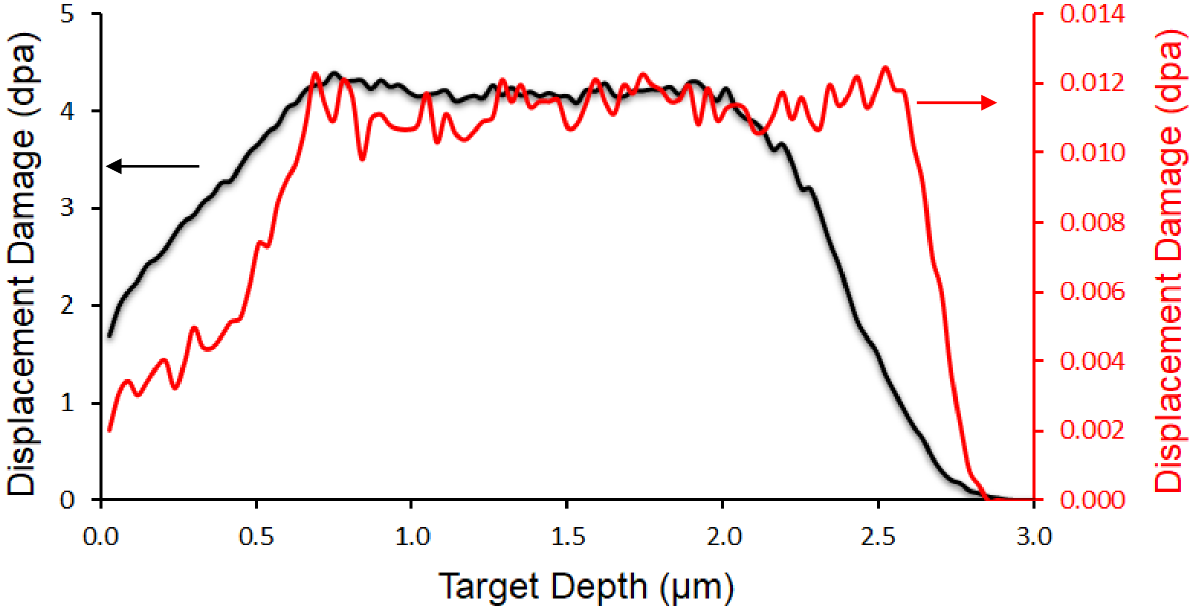

Figure 4.1: He^+ ion-induced atomic displacement profile (Red) resulting from fourteen consecutive implantation energies (E_{He+} = 0.3-1.6 MeV) and Ni^+ ion-induced atomic displacement profile (Black) resulting from thirteen consecutive implantation energies (E_{Ni+} = 2.0-8.0 MeV)

4.2.2 Nano-indentation hardness tests

Nano-indentation hardness measurements were performed to assess the effect of the combined C_{He} and ψ on the mechanical strength of the Inconel X750. The hardness tests were performed at 25°C with a Nano-Test indentation testing platform (Micro Materials Ltd, Wrexham UK) using a diamond Berkovich indenter under a constant indentation loading rate of 1 mN/s to optimize the performance of the nanoindenter; that is, providing the best balance between test duration and indentation depth precision. Partial unloading steps were performed such that the indentation hardness could be determined at indentation depths of 100, 200, up to 500nm. Twenty indentations, each spaced 30µm apart, were made in each ion implanted region of the samples. The plastic zone around a pyramidal indentation extends to a depth of about five times the indentation depth [14]. Our 500nm deep indentations therefore induced plastic deformation to a depth of about 2.5 µm in the Inconel X750 sample. This is well within the ion-implanted depth of 3 µm (Figure 4.1).

4.3 Results:

4.3.1 Effect of combined C_{He} and ψ on the indentation hardness

Figure 4.2-a shows a TEM micrograph of the non-irradiated heat-treated Inconel X750 alloy. The diffraction patterns, and related intensity profiles, display superlattice reflections indicative of the presence of ordered γ’ precipitates. In contrast, the superlattice reflections were absent in the samples implanted with ψ = 1 dpa Ni^+ (Figure 4.2-b) and C_{He} = 5000 appm He^+ (Figure 4.2-c) This indicates that the both implantation processes resulted in disordering of the γ’ phase.

The effect of sole Ni^+ induced atomic displacement damage, ψ, without accumulated helium, on the indentation hardness (h = 200nm) of the Inconel X750 is shown in Figure 4.3-a. The indentation hardness decreases with increasing ψ to 0.1 dpa and then displays increasing hardness with further increasing ψ. The initial softening trend has been attributed to ion-induced disordering of the γ’ phase [2,3]. The results in Figure 4.3-a indicate that the γ' disordering process starts at lower level of ψ than was previously reported. The increasing hardness with ψ greater than 0.1 dpa is the result of re-formation of γ' phase and increasing ion-induced crystal defects, such as dislocation loops and stacking fault tetrahedra [12].

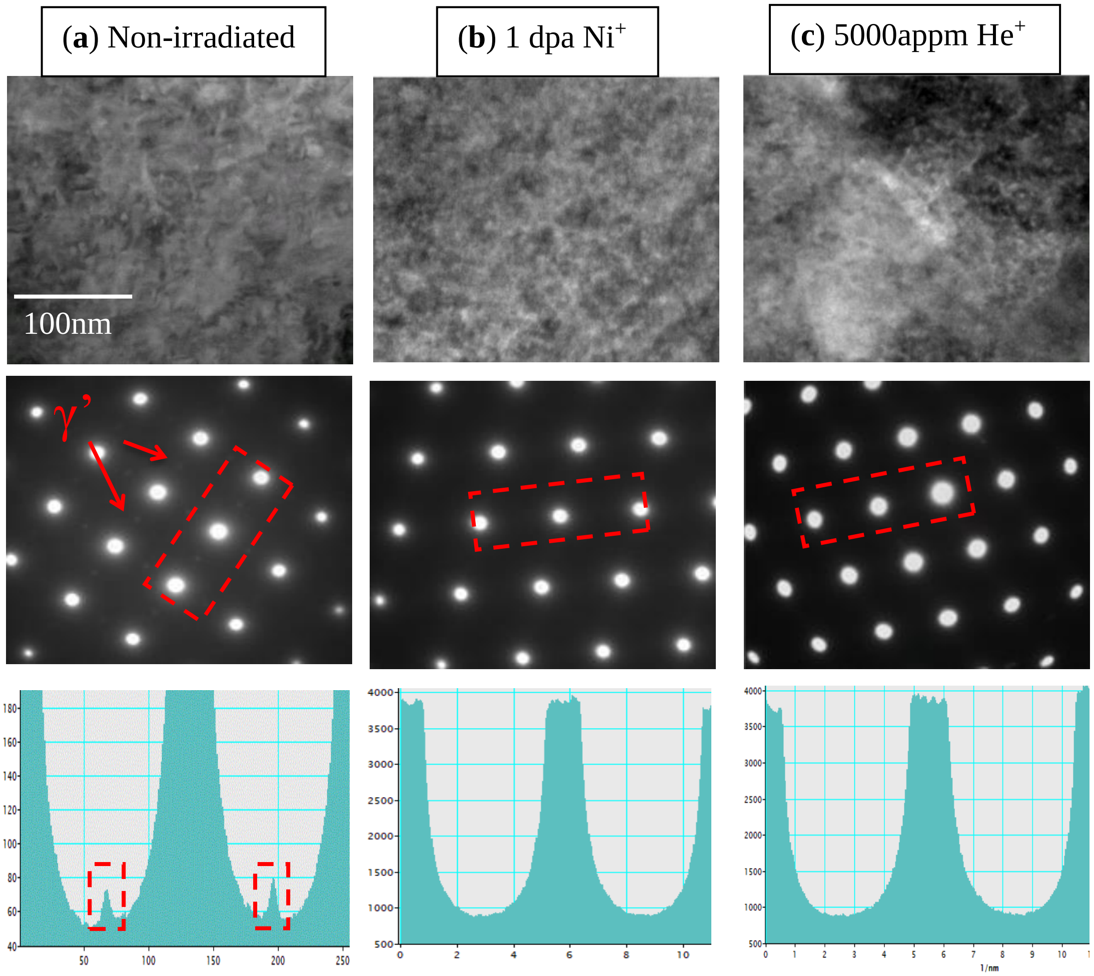

Figure 4.2: TEM micrograph of the Inconel X750 alloy along with selected area diffraction pattern close to zone axis [011] and associated diffraction spot intensity profile for: (a) non-implanted (b) 1 dpa Ni^+ implanted and (c) 5000appm He^+ implanted conditions.

The effect of accumulated helium, C_{He}, on the indentation hardness (h = 200 nm) of Inconel X750 is shown in Figure 4.3-b. SRIM calculation indicates that the He^+ implantation performed in this study induce only small amounts of atomic displacement. For example, He^+ implantation to C_{He} = 5000appm, the maximum implantation level in study, induces only ψ = 0.012dpa (Figure 4.1). Despite this, diffraction pattern analysis of this sample indicates disappearance of the γ' phase superlattice reflections (Figure 4.2-c). Figure 4.3-b indicates that a slight softening appears in the plot of H versus C_{He} at 5000 appm compared to 1000 appm at both 25^{o}C and 200^{o}C implantation temperatures. Bright field TEM images of the C_{He} = 5000appm sample (Figure 3.8) indicate the presence of helium nano-bubbles, approx. 0.7nm size.

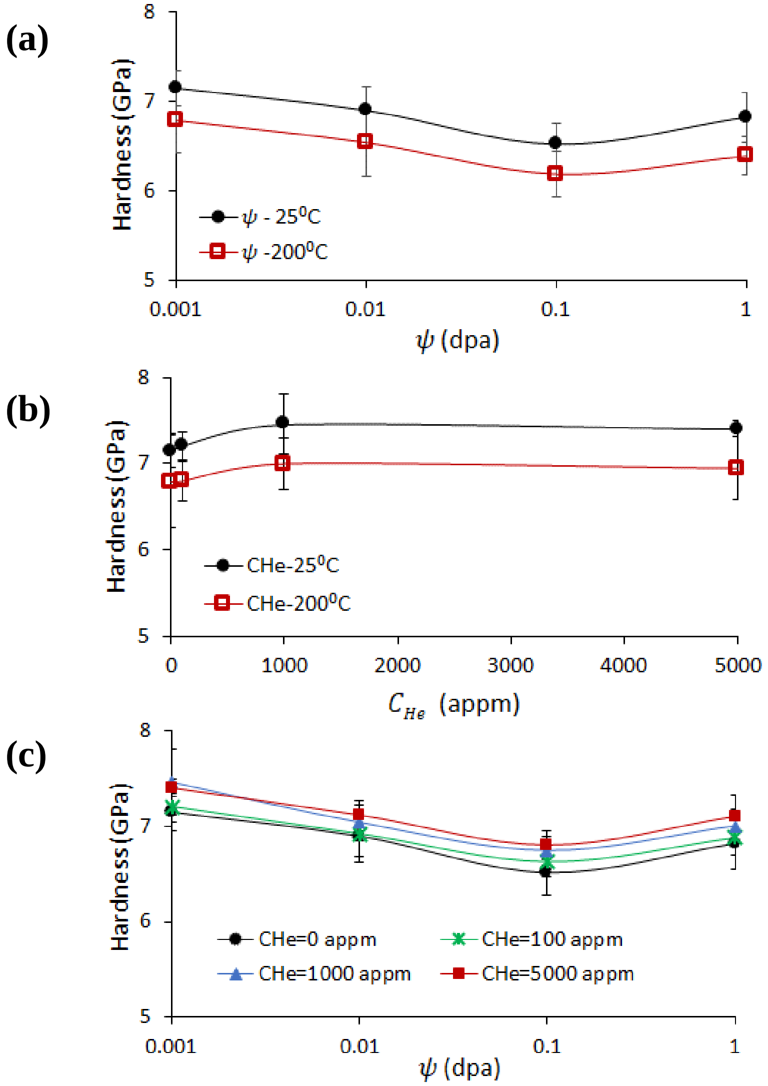

Figure 4.3: (a) Indentation hardness (h=200nm) as a function of sole Ni^{+} implantation induced ψ. (b) Indentation hardness (h=200nm) as a function of sole He^{+} implantation induced C_{He} (the broken lines indicate the slight softening of the alloy at C_{He} =5000 appm). (c) Indentation hardness (h=200nm) of sequentially He^{+}/Ni^{+} implanted samples as a function of ψ at 25°C. Error bars represent the measurement of the amount of variation of hardness data.

Figure 4.3-c displays the trends of H (h = 200 nm) versus ψ for samples that were first implanted to various levels of He^+ followed by Ni^+ implantation to various levels of ψ. The indentation hardness follows a similar trend with increasing ψ as when the material was solely Ni^+-implanted (Figure 4.3-a); however, while H decreased by about 600 MPa when ψ = 0.1 dpa and C_{He} = 0, it drops by only about 300MPa when ψ = 0.1 dpa and C_{He} = 5000appm. This indicates that implanted helium reduces the softening effect initiated by high energy Ni^+-induces γ’ phase disordering. This observation is consistent with microstructural changes observed in TEM studies of X750 subjected to dual-beam (He^+/ Ni^+) implantation [8].

4.3.2 Effect of implantation temperature (T_{imp}) on the indentation hardness

Lower hardness values were obtained for samples implanted with Ni^+ at 200°C than at 25°C (Figure 4.3-a). Despite this difference, the hardness of both implantation temperatures shows very similar trend with increasing ψ and C_{He}. Figure 4.4 illustrates the change in hardness as a function of Ni^+ induced ψ at all C_{He} levels of this study. The minor differences in values between both irradiated temperatures especially at higher ψ and C_{He} (1dpa and 5000appm) are within error bars describing the variability in the measured hardness. The similarity in the H trend indicates that the strengthening phase γ’ is disordering at the same rate even at a temperature as high as 200°C.

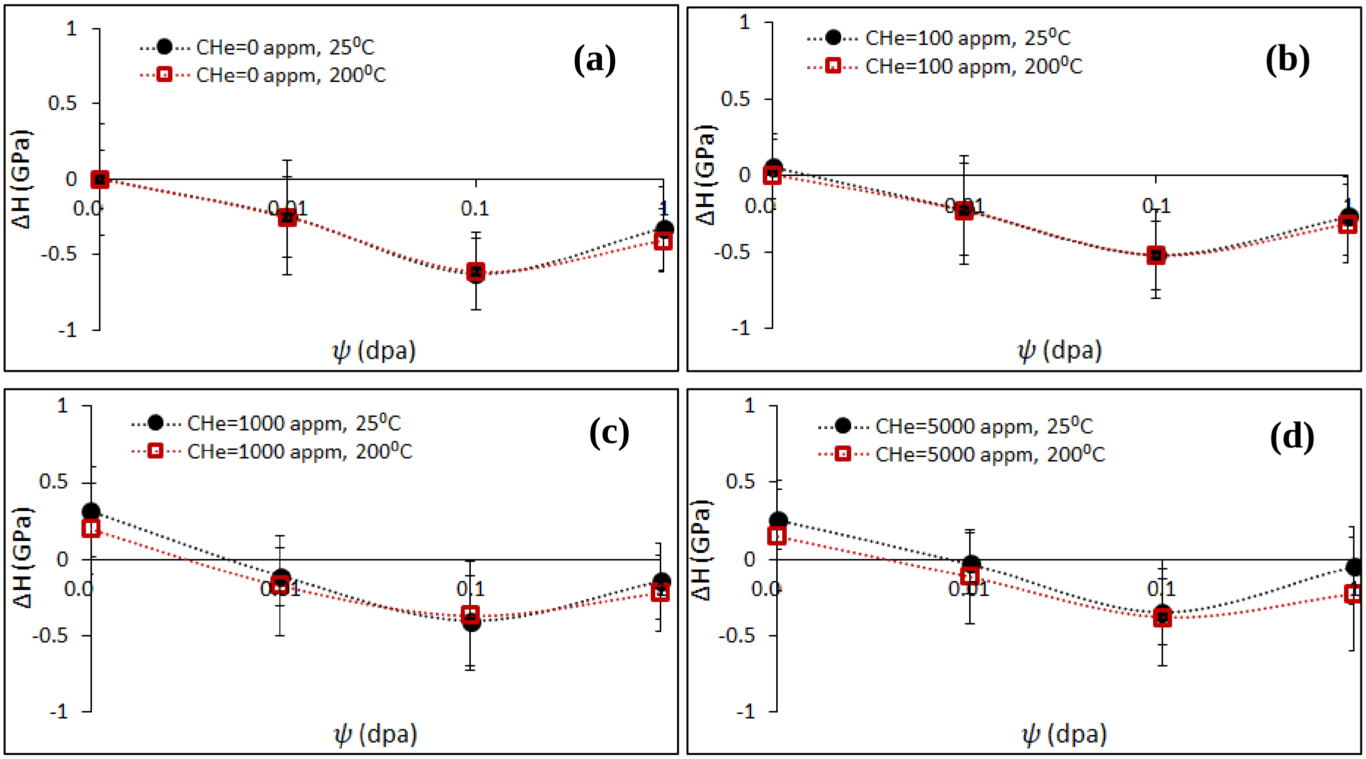

Figure 4.4: Change in hardness as a function of ψ (Ni$^+$ dose) and He$^+$ concentration at 25°C and 200°C (a) C_{He} = 0 appm (b) C_{He} = 100 appm (c) C_{He} = 1000 appm (d) C_{He} = 5000 appm.

4.3.3 Effect of C_{He} and ψ on the length-scale dependence of the indentation hardness

Figure 4.5 (a-c) show the average indentation hardness plotted versus indentation depth for typical non-implanted, sole Ni$^+$, and sole He$^+$ implanted X750 samples. For all test conditions, decreasing hardness with increasing indentation depth was observed. This is typical of the indentation size effect (ISE) displayed by most ductile metals [15]. We have used the popular Nix and Gao model to quantify the dependence of the ISE upon ψ *and* C_{He}. This model accounts for the ISE of the hardness by recognizing that shallow, sub micrometer depth, indentations invoke an increased strain gradient compared to deeper indentations and this necessitates an increased “geometrically necessary” dislocation density within their small plastic zone and, thus, increased hardness [16]. The Nix and Gao model expresses the indentation hardness H in terms of the indentation depth h as:

$$\frac{H}{H_0} = \sqrt{1 + \frac{h^*}{h}} \tag{4-1}$$

where H_0 is the hardness at large depth (i.e. the macroscopic hardness) and h* is the characteristic indentation depth which, for a given indenter shape, depends upon the microstructure of the indented material and reflects the ISE of the particular microstructure. By plotting H^2 versus 1/h, both H_0 and h* were calculated for the X750 samples implanted to each ψ *and* C_{He} level (Table 4-1).

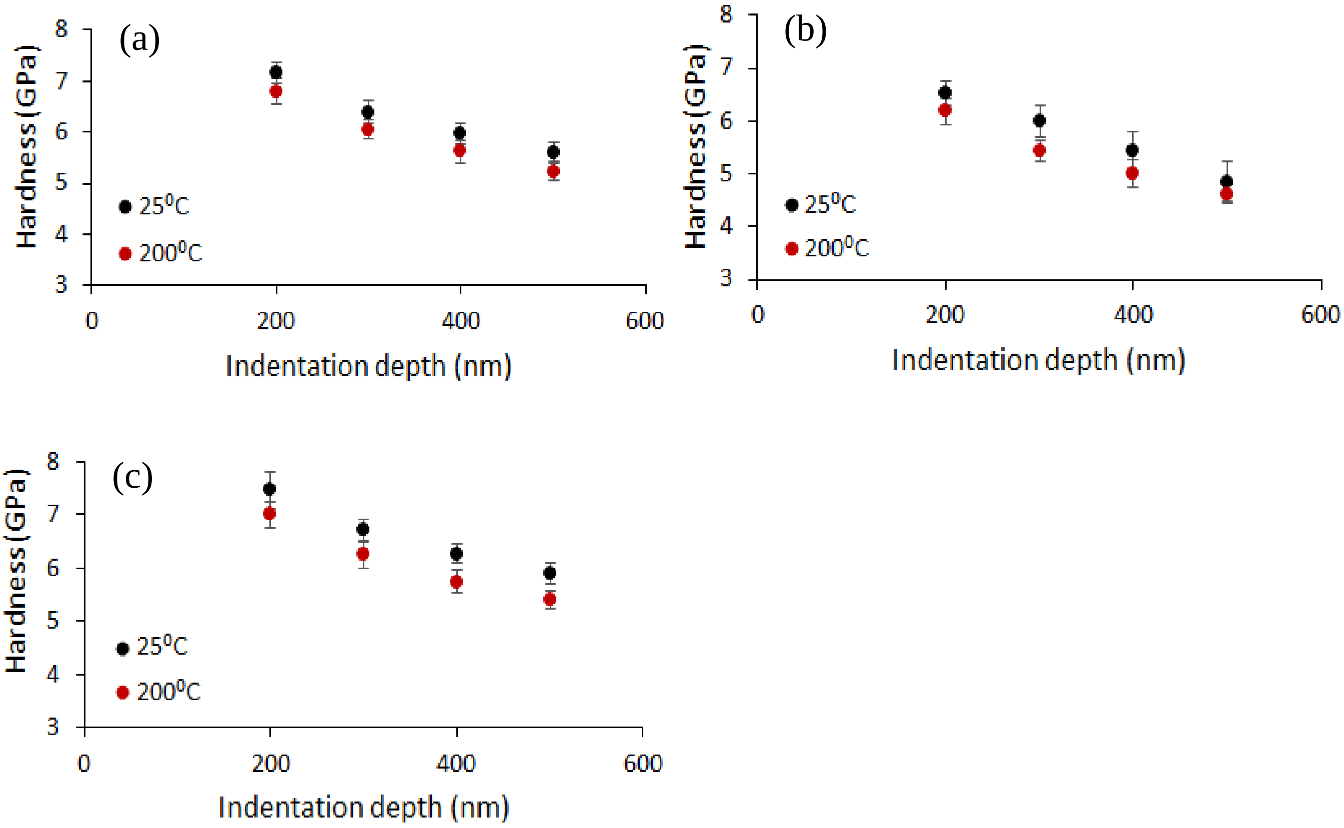

Figure 4.5: Shows indentation hardness as a function of indentation depth for (a) non-implanted samples, (b) sole Ni^+ implanted samples (ψ = 0.1 dpa), and (c) sole He^+ implanted samples (C_{He} =1000appm). Error bars represent the measurement of the amount of variation of hardness data.

Table 4-1: Characteristic indentation depth h* and infinite depth hardness H_o calculated by applying Eq.4-1 to the measured hardness data for sole Ni^+ and He^+ implanted samples of Inconel X750. The magnitude of h* indicates the ISE of the material.

		25ºC		200ºC	
		H_o (GPa)	h* (nm)	H_o (GPa)	h* (nm)
ψ (dpa)	0	4.35	348	3.96	393
	0.01	4.13	376	3.65	434
	0.1	3.7	442	3.23	513
	1	4	370	3.60	472
C_{He} (appm)	100	4.34	349	3.97	388
	1000	4.45	356	4.10	395
	5000	4.65	317	4.10	378

Figure 4.6-a presents the characteristic indentation depth h* as a function of ψ for the sole Ni^+ implanted samples. Nickel implantation results in a pronounced change in h*, and hence a change in the ISE, of the X750 material. h* increases by 21%, from h* = 348 nm to 442 nm, and by 23%, from h* = 393 nm to 513 nm, when Ni^+ implanted to ψ = 0.1 dpa but then decreases to h* = 370 nm and 472 nm, when Ni^+ implanted to ψ =1.0 dpa at 25ºC and 200°C respectively. In contrast, h* decreased with increasing C_{He} levels (Figure 4.6-b). For example, h* is decreased from h* = 348nm to 317nm, and from h* = 393nm to 378nm, when implanted to C_{He} = 5000 appm at 25°C and 200°C respectively. On the other hand, ISE for sequential implantation shows that the high levels of C_{He} are notably changing the ISE while the low level (C_{He} = 100 appm) does not (Figure 4.6, c-d). h* reduced by 23% and 34%, from h* = 442nm to 360 nm at sole ψ = 0.1dpa compared to from h* = 360nm to h* = 331nm at sequential (1000appm+0.1 dpa) and (5000appm+0.1dpa) respectively at 25°C. Similar results were obtained for 200°C where the h* reduced by 27% and 30% for (1000appm+0.1dpa) and (5000appm+0.1dpa) sequential implantation compared to sole ψ = 0.1dpa implantation.

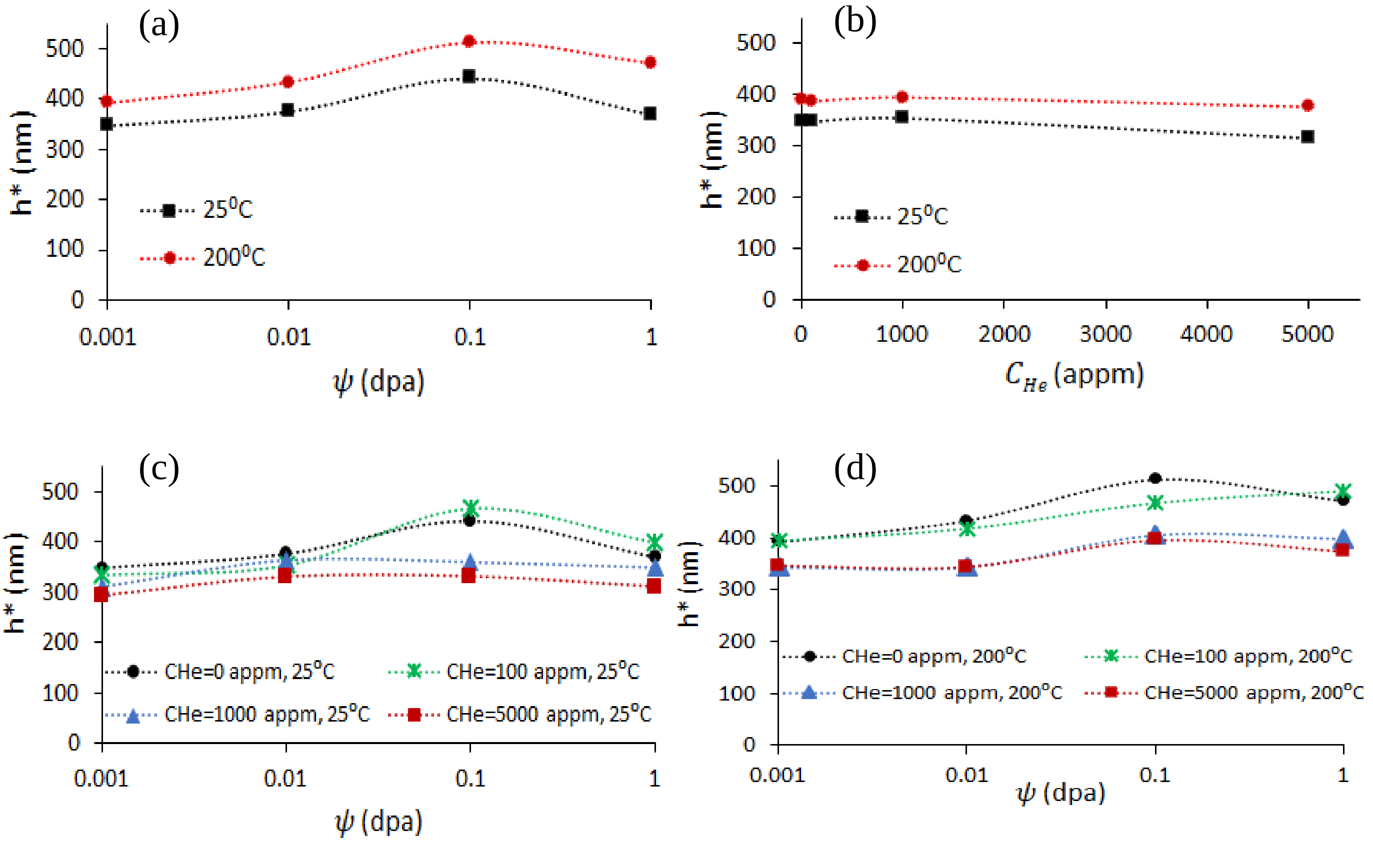

Figure 4.6: The characteristic indentation depth (h*) reflecting the ISE of the measured hardness versus ψ for sole Ni$^+$ implanted samples (a), versus C_{He} for sole He$^+$ implanted samples (b), and versus sequential He$^+$/ Ni$^+$ implantation at 25°C (c) and 200°C (d).

4.4 Discussion

The data from this study demonstrate how implantation helium and ion-induced crystal damage affect both the magnitude and the length scale dependence of the indentation hardness of heat-treated Inconel X750. While the indentation hardness H is a function of multiple parameters: T_{imp}, h, C_{He} and ψ, our findings from sequential He$^+$ and Ni$^+$ implantations (Figure 4.3-c) indicate that its dependence upon the parameters C_{He} and ψ can be accurately treated as independent and additive. We will demonstrate this hypothesis by applying accepted theories describing the dependence of H upon populations of nano-bubbles and crystal defects and upon ion-induced dissolution of coherent 2nd phase particles. The equations describing H resulting from each mechanism are then superimposed to predict the net change in hardness ΔH measured from the sequentially implanted He^+ and Ni^+ implantations.

4.4.1 Effect of helium Nano-bubbles on increasing the hardness (ΔH_{He})

The data from our sole He^+ implanted X750 samples indicate that H (h = 200nm) increases by about 0.4 GPa (4 %) as a result of helium implantation to a level of C_{He} = 5000 appm (Figure 4.3-b). Similar hardening trends were previously reported for Inconel X750 and other materials [5,17,18] and are typical of a mechanism whereby helium nano-bubbles act as weak obstacles to dislocation glide. The characteristic strength α of these obstacles can be expressed as [19]:

$$\alpha = \tau_y \lambda / \mu b \tag{4-2}$$

Where τ_y = 0.88 GPa, μ=76.5 GPa [20], and b=0.249 nm[13] are the yield stress in shear, elastic shear modulus, and Burgers vector of pure nickel respectively and are taken to be similar to those of our nickel-based Inconel X750 alloy. In Eq. (4-2) λ=0.6 nm is the average spacing between the helium bubbles measured from our TEM micrographs. Substituting these data into Eq. (4-2) yields a characteristic obstacle strength of α = 0.03 when C_{He} = 5000appm. This low value of characteristic obstacle strength suggests that the Friedel-Kroupa-Hirsch (FKH) dislocation-obstacle hardening rule is most applicable for describing the incremental hardening ΔH_{He} of Inconel X750 resulting from distributed helium nano-bubbles [17,21]:

$$\Delta H_{He} = 2.7 \Delta\sigma_{He} = 2.7\left(\frac{1}{8} M \mu b d N_{bubbles}^{\frac{2}{3}}\right) \tag{4-3}$$

In this expression M is the Taylor factor (3.06 for FCC and BCC metals) [17,18], and d =0.7 nm is the nano-bubble diameter (measured from TEM images Figure 3.8), and $N_{bubbles}$

is the number density of helium nano-bubbles. Table 2 lists values of $N_{bubbles}$ calculated, using the pressure - based method of Knapp et al. [5] (Appendix A).

Table 4-2: List of the calculated He bubbles density N_{He}, and incremental hardness ΔH_{He} resulting from the 25°C He^+ implantations performed in this study.

C_{He} (appm)	N (bubble/m^3)	ΔH_{He} (GPa)
100	2.05×10^{23}	0.05
1000	2.05×10^{24}	0.23
5000	1.02×10^{25}	0.36

By using Eq. (4-3) and assuming that the size of the helium nano-bubbles remains constant but $N_{bubbles}$ increases linearly with increasing C_{He} (Eq. A-4), ΔH_{He} can be calculated and is shown as a function of C_{He} in Table 4-3. The calculated ΔH_{He} increases linearly with C_{He} and displays reasonably good agreement with the experimentally measured values of ΔH_{He} (Figure 4.7-a). The minor differences between both cases are presumably due to the assumptions considered during the theoretical analysis. It should be noted that an irradiation damage equal to 0.01dpa was subtracted from the 5000appm helium implanted data, since at this point, the concentration of implanted helium is adding a radiation defects to the material equal to 0.01dpa (Figure 4.3-b) and causing a disordering in γ’ precipitates.

Table 4-3: list of irradiation-induced defect size and density measured directly from reference [12] and used to calculate hardening values (ΔH_{defect})

ψ (dpa)	ρ_d (m^{-2})	d_{SFT} (nm)	d_{loops} (nm)	ΔH_{defect} (GPa)
0.01	6×10^{14}	0.9	1.43	0.09
0.1	1.4×10^{15}	1.25	1.9	0.17
1	3×10^{15}	1.2	1.8	0.3

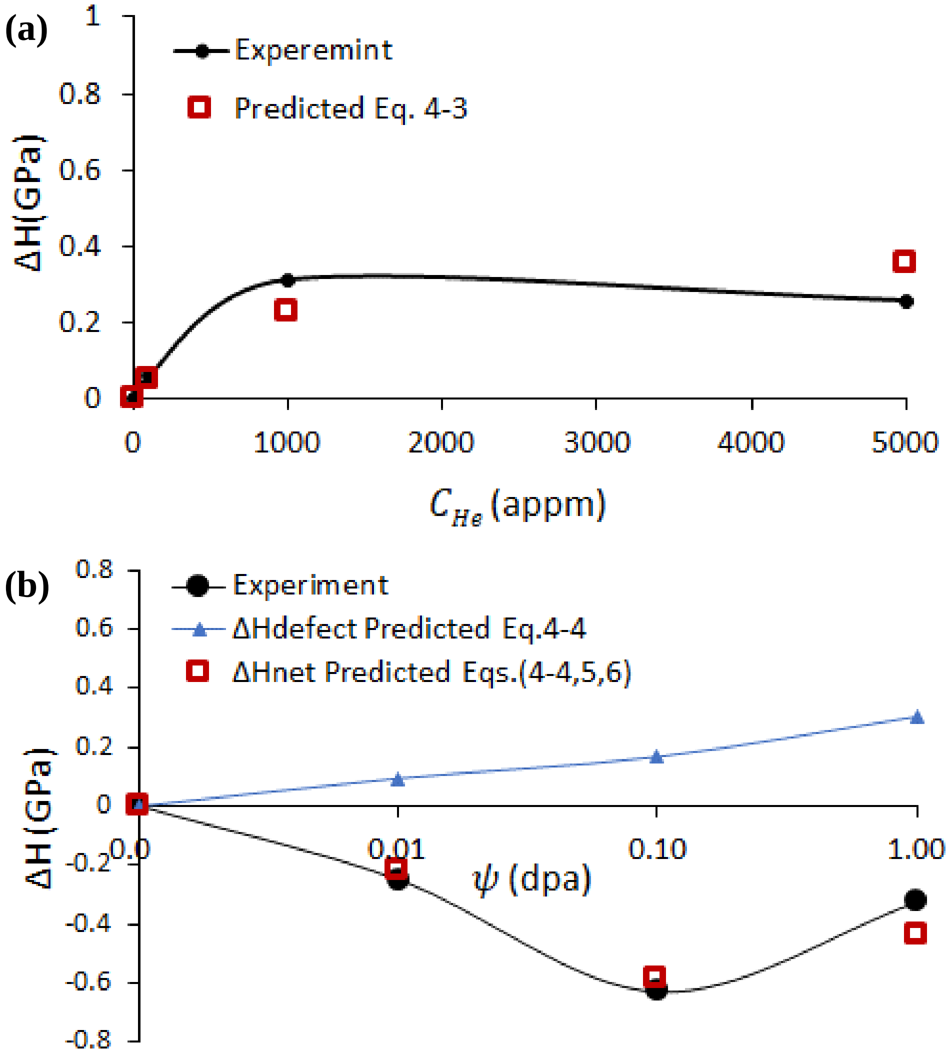

Figure 4.7: Measured and predicted (Eqs. 4-3,4,5,6) change in hardness ΔH of the sole Ni^+ / He^+ implanted Inconel X750 alloy as a function of: (a) implanted helium C_{He} (b) Ni^+ implantation damage ψ.

4.4.2 Effect of Ni$^+$-induced crystal defects on increasing the hardness (ΔH_{defect})

Nickel ion induced crystal defects, such as dislocation loops and stacking fault tetrahedra, are commonly observed in TEM studies of Ni$^+$ implanted Inconel X750 [12,13]. The size of these defects is small, typically between 1-2 nm, when the irradiation temperature is low however their population increases with increasing implantation dosage. Like helium nano-bubbles, ion-induced defects act as weak obstacles to dislocation glide [22]. The dispersed barrier hardening model (Eq. 4-4) is widely used to predict incremental stress $\Delta\sigma_{defect}$ required for an edge dislocation to bypass a periodic array of such obstacles, of characteristic strength α and inter-obstacle spacing l_ϕ Since the average hardness of a metal, when determined by pyramidal indentation, is H = 2.74σ [23,24], the dispersed barrier hardening model predicts the increase in hardness (ΔH_{defect}) resulting from the presence of ion-induced crystal defects to be [21,25]:

$$\Delta H_{defect} = 2.74\Delta\sigma_{defect} = \frac{2.74M\alpha\mu b}{l_\phi} = 2.74M\alpha\mu b\sqrt{\rho_d\, d} \qquad \text{(4-4)}$$

where ρ_d and d are the density and size of the defect clusters. The average size of the defects (i.e. dislocation loops and SFT) along with their densities, for each corresponding irradiated dose, were taken from previous TEM studies of Inconel X750 [12] and are listed in Table 4-3 along with our calculated values of ΔH_{defect} Figure 7-b (continuous blue line) shows ΔH_{defect} versus ψ. ΔH_{defect} is proportional to ψ and is of similar magnitude as previously reported ΔH values from studies of other ion-implanted nickel alloys [13,26].

4.4.3 Effect of Ni$^+$-induced γ' disordering on decreasing the hardness ($\Delta H_{\gamma'}$ and ΔH_{ε})

Heat-treated Inconel X750 is hardened by the presence of ordered coherent γ' precipitates. The incremental hardening resulting from obstacle strengthening that these precipitates provide can be expressed as [27]:

$$\mathrm{H}_{\gamma'} = 2.74\Delta\sigma_{\gamma'} = 2.74M\Delta\tau_{\gamma'} = 2.74M\frac{\gamma_{APB}}{2b}\left[\left(\frac{3\pi^2\gamma_{APB}\,\text{ʃ}l}{32T}\right)\frac{1}{2} - \text{ʃ}\right] \tag{4-5}$$

where γ_{APB} is the antiphase boundary energy γ_{APB}=0.2 J/m^2 for Inconel X750 [28], l is the average spacing and ʃ (ʃ = 0.26 for Inconel X750) is the volume fraction of the γ' precipitates, T is the dislocation line tension (T=μb^2/2 [21]) and M is the Taylor factor. Eqs. 4-5 was used to calculate $\Delta H_{\gamma'}$ for each ψ condition of the Ni$^+$ implanted samples by using values of l that were previously measured by TEM performed on heat-treated Inconel X750 samples that were ion-implanted to similar levels of ψ (Table 4-4).

Elastic coherency strain ε associated with γ' precipitates also contributes to the strengthening to heat-treated Inconel X750 by impeding dislocations motion. The incremental hardening resulting from the presence of ε can be calculated as [27]:

$$H_\varepsilon = 3.28M\text{ʃ}^{1/2}\left(\frac{T^3\mu\varepsilon}{b^3r^3}\right)^{\frac{1}{4}} \tag{4-6}$$

where ε =0.5% for heat-treated Inconel X750 [3,12] and r is the average radius of the γ' precipitates. Ion-induced disordering of the γ' precipitates has the effect of reducing ε and leads to a drop in hardness (Table 4-4).

Figure 4.7-b shows a plot of the net change in hardness, ΔH_{net}= ΔH_{defect} + $\Delta H_{\gamma'}$ +ΔH_ε versus ψ. Good agreement between the calculated ΔH_{net} and the experimental data indicates that the ion-induced hardening and softening mechanisms are quite accurately predicted by the additive application of Eqs. 4-4 to 4-6 for the sole Ni$^+$-implanted X750 samples.

Table 4-4: list of the data used in Eq. (4-5 and 4-6) to calculate the hardness drop results from γ' precipitate disordering, along with the obtained results

	γ' disordering		misfit strain	
ψ (dpa)	l (nm)[2][3]	$\Delta H_{\gamma'}$ (GPa)	r (nm)[2][3]	ΔH_{ε} (GPa)
0.01	13	-0.22	11.4	-0.10
0.1	8	-0.59	11.75	-0.16
1	10	-0.43	12.4	-0.31

4.4.4 Effect of sequential He$^+$ and Ni$^+$ implantation on the hardness

In this discussion we have considered the hardening resulting from implanted helium to be independent of the softening/hardening resulting from implanted Ni$^+$. We also assume that various hardening or softening effects of the various proposed mechanisms (Eqs. 4-3 to 4-6) operate independently and are additive. This assumption can be validated by plotting the total hardening increment as $\Delta H_{total} = \Delta H_{He} + \Delta H_{defect} + \Delta H_{\gamma'} + \Delta H_{\varepsilon}$ versus ψ for samples of X750 that were first implanted with He$^+$, to achieve a certain level of C_{He}, and then implanted with Ni$^+$ to achieve a certain level of ψ (Figure 4.8). Again, a good match between the calculated ΔH_{total} and the experimentally measured hardness data exist. This suggests that the hardening and softening mechanisms (Eqs. 4-3 to 4-6) are accurate in describing the operative deformation mechanisms and that the hardening effect of the various mechanisms is essentially additive.

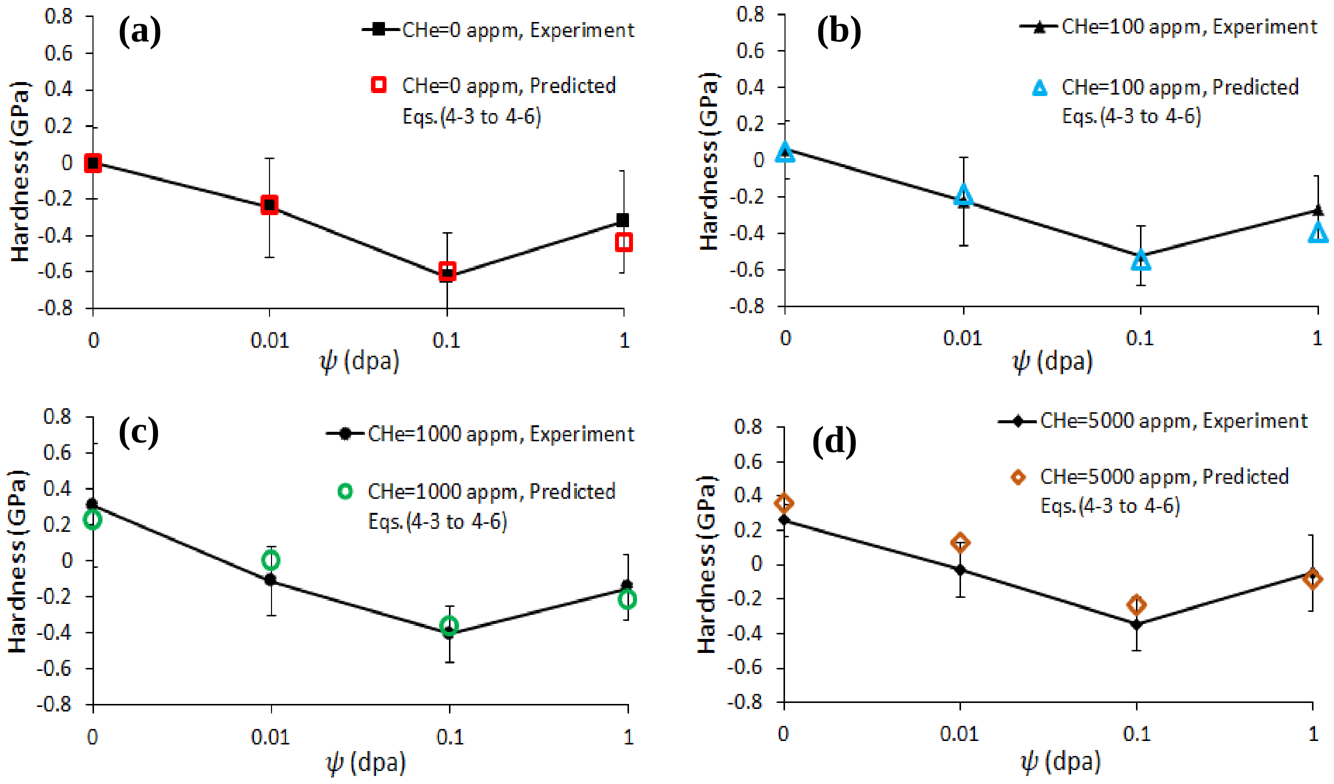

Figure 4.8: shows comparison between experimental and theoretical analysis of change in hardness as a function of ψ (dpa) and C_{He} (appm) for sequential He^+/ Ni^+ implanted Inconel X750 at: (a) C_{He} =0 appm. (b) C_{He} = 100appm, (c) C_{He} = 1000appm and (d) C_{He} = 5000appm. Error bars represent the measurement of the amount of variation of hardness data.

4.4.5 Effect of implantation temperature (T_{imp}) on the hardness

A previous TEM study of in-situ ion implanted Inconel X750 [12] has shown that implantation-induced defect density is not strongly dependent upon implantation temperature but rather strongly dependent upon ion implantation dose. Therefore, the low hardness values obtained at 200°C Ni^+ irradiation suggest that the increase in irradiation temperature results in higher defects mobility, and thus higher rate of mutual annihilation by the recombination of vacancy and interstitial. In other words, high temperature irradiation may lead to irradiation damage annealing, reducing the density of interstitial defect clusters and recovery of the dislocation network. This phenomena have been observed in several previous studies [29,30]. The similarity in the H versus ψ and C_{He} for samples implanted at 25^{o}C and 200^{o}C indicates that the operative hardening and softening mechanisms (Eqs. 4-3 to 4-6) are occurring at the same rate at both temperatures. This is in agreement with the findings of Zhang et al [2] who reported the γ' phase stability in X750 under in situ irradiation that the disordering process is existing at irradiation temperature ranging between (60^{o}C $\leq T_{imp} \leq$ 400^{o}C) but are stable at higher irradiation temperature. Similar temperature range for γ' disordering have been reported by Nelson et al [31] (25^{o}C $\leq T_{imp} \leq$ 300^{o}C) and Camus et al [32] (25^{o}C $\leq T_{imp} \leq$ 267^{o}C) for other Ni alloys. It is worth mentioning that, while the relatively low implantation temperature (i.e. $T_{imp} \leq$ 200^{o}C) effect on X750 microstructure evolution was studied, this is the first observation on the X750 nanoindentation hardness.

4.4.6 Indentation size effect

An outcome of the Nix and Gao model (Eq. 4-1) of the indentation size effect (ISE) of the hardness of metals is that prior plastic deformation, cold-work, should decrease the ISE, and result in a decreased characteristic dept h*, due to the increase in existing, statistically stored, dislocation density. Hosemann et al argued that radiation damage will have a similar effect on ISE since ion-induced crystal damage essentially increases the statistically stored dislocation density [33]. This was confirmed by studies performed on Fe^{9+} implanted 800H alloy [34] and He^{+} implanted steel [35]. ISE study was performed on sequentially implanted [13], solely implanted and non-implanted X750 [3]. In these studies, it was reported that implanted X750 displays a lower ISE effect than non-implanted samples. The study of Ref [13] included only one sample that was sequentially irradiated at 400^{o}C. This is contrary to what we have observed from our investigations of multiple sequentially and solely He^{+}/ Ni^{+} implanted samples. We attribute this to differences in the implantation temperature (400^{o}C compared to 200^{o}C) and indentation depth (h = 200 nm – 1000 nm compared to h = 200 - 500 nm).

Since concurrent He^{+}/ Ni^{+} implantation of heat-treated Inconel X750 can result in the unique situation of simultaneous crystal damage accumulation, helium accumulation, and precipitate dissolution, the ion-induced change in the ISE may be quite different than observed in previously reported ion-implantation cases.

The hardness data from our study indicate that, for the case of the sole He^+ implanted X750 samples, the characteristic indentation depth h* follows a decreasing trend with increasing accumulated helium from C_{He} = 100appm-5000appm (Table 4-1, Figure 4.6-b). This can be attributed to the fact that accumulated helium resides as nano-bubbles within the microstructure and act as statistically stored obstacles to dislocation movement.

In contrast, sole Ni^+ implantation displays increased h* compared to the non-implanted and the sole He^+ implanted X750 samples (Table 4-1, Figure 4.6-a). It is interesting to note that h* increases rapidly with small increases in ψ and appears to reach a maximum at about ψ = 0.1 dpa. This corresponds to the level of implantation damage where the indentation hardness of the aged Inconel X750 is minimum (Figure 4.3-a). Although the Ni^+-induced statistically stored defect density (i.e. dislocation loops and SFT) increase continuously with increasing ψ, the concurrent effect of Ni^+ induced γ' phase disordering, which occurs in this alloy at low values of ψ, will decrease the overall statistically stored dislocation density, particularly in the region of ψ = 0.1 dpa, and this has the effect of increasing h*. Sequential implantation interestingly seems to combine the effects of sole implantation on the ISE. That is, the increase in characteristic depth h* under the sole Ni^+ irradiation was reduced because of prior C_{He} implantation especially at the high ion implantation levels. In other words, the formation of helium nano-bubbles appears to compensate for the disordering of the γ' phase and result in hardening of the alloy, thus lowering h* for both implantation temperatures studied.

4.5 Conclusion

The influence of sole and sequential He^+ and Ni^+ implantation, at 25^{o}C and 200^{o}C, on the nanoindentation hardness of the aged Ni-based Inconel X750 alloy was investigated. The results can be summarized as follows:

- The indentation hardness (h = 200nm) and TEM investigation indicate that the γ' strengthening phase of this alloy becomes significantly disordered when subjected to very low levels of sole Ni^+ implantation corresponding to about ψ = 0.01dpa and high levels of He^+ implantation up to C_{He} =5000appm.

- The combined effect of ion-induced crystal defects, γ' phase disordering, and nano-bubble formation determines the indentation hardness of this X750 alloy, and their effect is found to be additive for both sole implanted and sequentially implanted samples.

- Sequential $He^+/\ Ni^+$ implantation was found to mitigate the softening behavior resulting from γ' phase disordering. And supports our finding that Ni^+-induced softening and He^+ -induced hardening mechanisms operate independently and are additive.

- Both Ni^+ implantation temperatures (25 and 200^{o}C) resulted in similar softening behavior which indicates that γ' disordering occurs throughout this implantation temperature range.

- The indentation size effect (ISE) is less pronounced in sole He^+ implanted samples compared to sole Ni^+ implanted samples. Sequential He^+/ Ni^+ implantation shows lower ISE compared to sole Ni^+ implantation and follows more closely the trend displayed by sole He^+ implanted samples. In all conditions, the ISE for samples implanted at 200^{o}C is more evident than for sampled implanted at 25^{o}C. This suggests that slight thermal annealing affects the configuration of ion-induced crystal damage when implantation is performed at 200^{o}C compared to 25^{o}C.

4.6 Acknowledgment

The authors wish to acknowledge the assistance of Mr. Jack Hendriks at the Tandetron Ion Accelerator facilities at the University of Western Ontario (London, Ontario, Canada) for his support with performing ion implantations of the Inconel X750 samples. The assistance of Dr. T. Simpson of the University of Western Ontario Nanofabrication Laboratory in preparing the TEM foils is gratefully acknowledged. The authors offer a special note of thanks to Dr. Carmen Andrei in Canadian Centre for Electron Microscopy- McMaster for her help with using TEM. The authors also gratefully acknowledge financial funding of the Natural Science and Engineering Research Council (NSERC) and University Network of Excellence in Nuclear Engineering (UNENE) for funding this study. M.N.T. acknowledges the financial support of the government of the province of Ontario, Canada through an Ontario Graduate Scholarship.

4.7 Appendix A: Calculation of the number density of helium bubbles

Here we describe our application of the pressure - based method of Knapp et al [5] to calculate the number density of helium bubbles ($N_{Bubbles}$) in the He$^+$ implanted Inconel X750 samples. We define N_{He} as:

$$N_{He} = V_{Bubble}/V_{molar} \quad \text{A-1}$$

The average volume of each nano-bubble is simply $V_{Bubble}=\pi d^3/6$ where d = 0.7 nm as obtained from TEM measurements on He$^+$ implanted Inconel X750. The molar volume V_{molar} of implanted helium is a function of the average helium pressure P within the nano-bubbles and was calculated as:

$$P = \frac{\gamma_{sur} + 2\mu b}{d} \quad \text{A-2}$$

Where γ_{sur} is the surface energy of nickel (2.28 J/m^2) [1]. The He pressure inside the bubble was calculated from this equation to be P = 67.5 GPa. The equation of state for helium (Eq. A-3) [36] was used to determine V_{molar} as a function of P and the He$^+$ implantation temperature (T = 298 K):

$$\begin{aligned} V_{molar} = &\left(22..575 + 0.0064655T - 7.2645T^{-\frac{1}{2}}\right)P^{-\frac{1}{3}} \\ &+ (-12.483 - 0.024549T)P^{-\frac{2}{3}} \\ &+ \left(1.0596 + 0.10604T - 19.641T^{-\frac{1}{2}} + 189.84T^{-1}\right)P^{-1} \end{aligned} \quad \text{A-3}$$

Assuming all the implanted helium atoms reside within spherical nano-bubbles of average diameter d = 0.70 nm, the average number of He atoms in each bubble was calculated found to be N_{He}=34. The density of He bubbles ($N_{Bubbles}$) can now be calculated as [37]:

$$N_{Bubbles} = C_{He}\frac{\rho_{X750}}{N_{He}} \quad \text{A-4}$$

Where C_{He} in this equation is given in units of atomic percent.

4.8 References

[1] M. Griffiths, “The Effect of Irradiation on Ni-Containing Components in CANDU ® Reactor Cores: A Review,” *AECL Nucl. Rev.*, vol. 2, no. 1, pp. 1–16, 2013.

[2] H. K. Zhang, Z. Yao, M. A. Kirk, and M. R. Daymond, “Stability of Ni3(Al, Ti) gamma prime precipitates in a nickel-based superalloy inconel X-750 under heavy ion irradiation,” *Metall. Mater. Trans. A Phys. Metall. Mater. Sci.*, vol. 45, no. 8, pp. 3422–3428, 2014.

[3] P. Changizian, C. Lu, Z. Yao, and L. M. Wang, “Indentation behaviour of ion-irradiated X-750 Ni- based superalloy,” *Philos. Mag. Lett.*, vol. 97, no. 3, pp. 101–109, 2017.

[4] M. Griffiths *et al.*, “Degradation of Ni-alloy Components in CANDU Reactor Cores,” in *16th Int. Conference on Environmental Degradation of Materials in Nuclear Power Systems – Water Reactors, Asheville, North Carolina, USA,August 11-15*, 2013.

[5] J. A. Knapp, D. M. Follstaedt, and S. M. Myers, “Hardening by bubbles in He-implanted Ni,” *J. Appl. Phys.*, vol. 103, p. 013518, 2008.

[6] N. Hashimoto, J. D. Hunn, T. S. Byun, and L. K. Mansur, “Microstructural analysis of ion-irradiation-induced hardening in inconel 718,” *J. Nucl. Mater.*, vol. 318, pp. 300–306, 2003.

[7] H. Zhang, Z. Yao, M. R. Daymond, and M. A. Kirk, “Cavity morphology in a Ni based superalloy under heavy ion irradiation with cold pre-injected helium. I,” *J. Appl. Phys.*, vol. 115, no. 10, p. 103509, 2014.

[8] P. Changizian, H. K. Zhang, and Z. Yao, “Effect of simultaneous helium implantation on the microstructure evolution of Inconel X-750 superalloy during dual-beam irradiation,” *Philos. Mag.*, vol. 95, no. 35, pp. 3933–3949, 2017.

[9] C. D. Judge *et al.*, “Intergranular fracture in irradiated Inconel X-750 containing very high concentrations of helium and hydrogen,” *J. Nucl. Mater.*, vol. 457, pp. 165–172, 2015.

[10] M. N. Tawfeeq and R. J. Klassen, “Effect of ion implantation on the grain boundary strength of heat treated Inconel X750,” *J. Nucl. Mater.*, vol. 516, pp. 255–263, 2019.

[11] C. D. Judge *et al.*, “The effects of proton irradiation on the microstructural and mechanical property evolution of inconel X-750 with high concentrations of helium,” *J. Nucl. Mater.*, vol. 492, pp. 213–226, 2017.

[12] H. Ken, Z. Yao, C. Judge, and M. Griffiths, "Microstructural evolution of CANDU spacer material Inconel X-750 under in situ ion irradiation," *J. Nucl. Mater.*, vol. 443, pp. 49–58, 2013.

[13] P. Changizian, A. Brooks, Z. Yao, and M. R. Daymond, "Nano-scale Mechanical Properties and Microstructure of Irradiated X-750 Ni-Based Superalloy," *Metall. Mater. Trans. A*, vol. 49, pp. 498–514, 2018.

[14] D. Kiener, A. M. Minor, O. Anderoglu, Y. Wang, S. A. Maloy, and P. Hosemann, "Application of small-scale testing for investigation of ion-beam-irradiated materials," *J. Mater. Res.*, vol. 27, no. 21, pp. 2724–2736, 2012.

[15] G. M. Pharr, E. G. Herbert, and Y. Gao, "The Indentation Size Effect : A Critical Examination of Experimental Observations and Mechanistic Interpretations," *Annu. Rev. Mater. Res.*, vol. 40, pp. 271–292, 2010.

[16] William D. Nix and Huajian Gao, "Indentation Size Effects in Crystalline Materials: A Law for Strain Gradient Plasticity," *J. Mech. Phys. Solids*, vol. 46, pp. 411–425, 1998.

[17] P. Landau, Q. Guo, P. Hosemann, Y. Wang, and J. R. Greer, "Materials Science & Engineering A Deformation of as-fabricated and helium implanted 100 nm-diameter iron nano-pillars," *Mater. Sci. Eng. A*, vol. 612, pp. 316–325, 2014.

[18] N. Li *et al.*, "He ion irradiation damage in Al/Nb multilayers," *J. Appl. PHYSIC*, vol. 105, p. 123522, 2009.

[19] Z. Wang, F. I. Allen, Z. Shan, and P. Hosemann, "Mechanical behavior of copper containing a gas-bubble superlattice," *Acta Mater.*, vol. 121, pp. 78–84, 2016.

[20] Metals Special Corporation, "INCONEL alloy X750," pp. 1–28, 2004.

[21] S. J. Zinkle and Y. Matsukawa, "Observation and analysis of defect cluster production and interactions with dislocations," *J. Nucl. Mater.*, vol. 333, no. 2004, pp. 88–96, 2008.

[22] T. S. Byun, K. Farrell, and M. Li, "Deformation in metals after low-temperature irradiation : Part II – Irradiation hardening , strain hardening , and stress ratios," *Acta Mater.*, vol. 56, pp. 1056–1064, 2008.

[23] J. T. Busby, M. C. Hash, and G. S. Was, "The relationship between hardness and yield stress in irradiated austenitic and ferritic steels," *J. Nucl. Mater.*, vol. 336, pp. 267–278, 2005.

[24] D. Tabor, "The physical meaning of indentation and scratch hardness," *Br. J. Appl. Phys.*, vol. 7, pp. 159–166, 1956.

[25] G. E. Lucas, “The evolution of mechanical property change in irradiated austenitic stainless steels,” *J. Nucl. Mater.*, vol. 206, pp. 287–305, 1993.

[26] C. Sun *et al.*, “Microstructure , chemistry and mechanical properties of Ni-based superalloy Rene N4 under irradiation at room temperature,” *Acta Mater.*, vol. 95, pp. 357–365, 2015.

[27] A. J. Ardell and L. Angeles, “Precipitation Hardening,” *Metall. Mater. Trans. A*, vol. 16A, pp. 2131–2165, 1985.

[28] J. A. de. Valle, A. C. Picasso, I. Alvarez, and R. Romero, “Age-Hardening Behavior of Inconel X-750 Superalloy,” *Scr. Mater.*, vol. 41, no. 3, pp. 237–243, 1999.

[29] A. F. Rowcliffe, L. K. Mansur, D. T. Hoelzer, and R. K. Nanstad, “Perspectives on radiation effects in nickel-base alloys for applications in advanced reactors,” *J. Nucl. Mater.*, vol. 392, no. 2, pp. 341–352, 2009.

[30] C. D. Hardie, C. A. Williams, S. Xu, and S. G. Roberts, “Effects of irradiation temperature and dose rate on the mechanical properties of self-ion implanted Fe and Fe – Cr alloys,” *J. Nucl. Mater.*, vol. 439, no. 1–3, pp. 33–40, 2013.

[31] R. S. Nelson, J. A. Hudson, and D. J. Mazey, “The stability of precipitates in an irradiation environment,” *J. Nucl. Mater.*, vol. 44, pp. 318–330, 1972.

[32] E. Camus, C. Abromeit, F. Bourdeau, N. Wanderka, and H. Wollenberger, “Evolution of long-range order and composition for radiation-induced precipitate dissolution,” *Phys. Rev. B*, vol. 54, no. 5, pp. 3142–3150, 1996.

[33] P. Hosemann, C. Shin, and D. Kiener, “Small scale mechanical testing of irradiated materials,” *J. Mater. Res.*, vol. 30, no. 9, pp. 1231–1245, 2015.

[34] A. Prasitthipayong, S. J. Vachhani, S. J. Tumey, A. M. Minor, and P. Hosemann, “Indentation size effect in unirradiated and ion-irradiated 800H steel at high temperatures,” *Acta Mater.*, vol. 144, pp. 896–904, 2018.

[35] Z. Y. Fu, P. P. Liu, F. R. Wan, and Q. Zhan, “Helium and hydrogen irradiation induced hardening in CLAM steel,” *Fusion Eng. Des.*, vol. 91, pp. 73–78, 2015.

Chapter 5

5 Effect of ion implantation on the grain boundary strength of heat-treated Inconel X750

In the previous chapters nanoindentation test were performed to assess the irradiation dose level and irradiation temperature on the microstructure and the indentation hardness of Inconel X750 grains. In the present chapter, the grain boundary strength was investigated before and after He^+ and Ni^+ ion implantation using micro-beam bending test.

5.1 Introduction

Annulus gas spacers in CANDU nuclear reactors are made from the heat-treated Inconel X750 Nickel-based alloy and are subjected to very high neutron fluence over their service life. They are thus susceptible to microstructural instability and mechanical property degradation with time. Studies of ex-service spacers have indicated that they display intergranular embrittlement and lower ultimate tensile strength, compared to nonirradiated Inconel X750 [1].

Recently, extensive investigations were undertaken to understand the microstructural evolution of heat-treated Inconel X750 when subjected to neutron irradiation (as simulated by high energy ion implantation). Electron microscopy studies demonstrated that the high energy ion implantation produce crystal defect clusters, stacking fault tetrahedral, and dislocation loops, that increase in size and distribution with increasing irradiation fluence. These defects lead to the observed irradiation hardening of the alloy [2].

Nickel-based alloys such as Inconel X750 are also subject to significant helium accumulation when exposed to thermal neutron radiation due primarily to $^{59}Ni(n,\alpha)^{56}Fe$ transmutation. The helium concentration within Inconel X750 annulus gas spacers can reach approximately 40,000 appm by the end of their service life in a CANDU nuclear reactor [1]. The effect of accumulated helium on promoting hardening of metals has been correlated to the formation of cavities/bubbles within grains and at grain boundaries [3,4]. Recent TEM studies of Inconel X750 have suggested that accumulation of helium bubbles along grain boundaries and matrix–precipitate interfaces may also be responsible for the onset of intergranular embrittlement [4]. Although the influence of irradiation-induced crystal defects and helium cavities/bubbles on the microstructure and bulk mechanical properties of heat treated Inconel X750 is now quite well documented, the role of grain boundary angular misorientation on irradiation-induced grain boundary embrittlement has received relatively little study despite the fact that grain boundary character is known to affect the strength, toughness and corrosion resistance of most metals [5-8].

The effect of grain boundaries is primarily expressed in terms of their crystallographic misorientation angle which influences the grain boundary energy. Also associated with the grain boundary energy is the tendency for defect and impurity accumulation at the boundary to minimize the boundary energy [9,10]. Radiation-induced diffusion and segregation of crystal point defects to grain boundaries has garnered extensive research with a number of studies examining factors related to this phenomenon in nickel alloys [11,12], austenitic stainless steel [13-15], and copper [9,16].

The research referred to above illustrates the important role that grain boundary misorientation and energy have on the microstructure of many alloys. In the case of heat-treated Inconel X750, it is important to understand the influence of grain boundary misorientation and energy on the mechanical strength of the alloy before and after neutron irradiation in order to correlate its effect on the onset of grain boundary embrittlement. Recent work has demonstrated that micron-scale notched cantilever beams manufactured by focused ion beam (FIB) machining and tested in bending can be used to measure a range of mechanical properties of a single grain boundary. Armstrong et al [17] used such micro-beams to perform bending tests to measure the fracture toughness of grain boundaries of a known angular misorientation in bismuth embrittled copper. The results indicated that grain boundaries of high angular misorientation displayed increased bismuth segregation and increased brittleness.

In this paper we report the findings of a study of grain boundary plasticity induced by bending of notched cantilever micro-beams of heat-treated Inconel X750 in the non-implanted condition and after implantation with high energy Ni^+ and He^+ ions. The objective is to determine the effect of the misorientation angle, irradiation-induced crystallographic damage, and accumulated helium on the strength of a grain boundary in heat treated Inconel X750.

5.2 Experimental procedure

5.2.1 Material

The chemical composition of the Inconel X750 alloy used in this study is given in Table 3-1. The alloy was annealed at 1010°C (30 minutes) followed by air cooling to room temperature, cold-working by 18%, and then ageing at 728°C (16 hours). The average grain size was found to be between 20-25μm. Three samples (6 x 6 x 3 mm) were cut from the aged X750 material. The samples were mechanically ground with successively finer grit SiC impregnated papers and then polished in an aqueous slurry of 0.02μm diameter colloidal SiO_2. This process created a surface free of polishing-induced plastic deformation as was evidence by the high quality electron backscatter diffraction (EBSD) patterns obtained.

5.2.2 Ion implantation

One polished Inconel X750 sample was implanted, at 25°C, with Ni^+ ions while another was implanted with He^+ ions using a high-current tandem ion accelerator located at the University of Western Ontario (http://isw.physics.uwo.ca/). The objective of the self-similar Ni^+ implantations was to generate a uniform irradiation-induced damaged microstructure corresponding to about one ion–induced displacement per atom (1 dpa) over a depth of about 3 μm into the sample. To accomplish this, multiple Ni^+ implantations were performed at different ion energy levels from 2.0 to 8.0 MeV. Similarly, another polished sample was exposed to multiple He^+ implantations at ion energy levels from 0.3 to 1.6 MeV to implant a uniform helium concentration, of about 5000 appm, over a depth of about 3 μm into the sample (Figure 5.1, a-b). The level of dpa and the appm helium concentration were determined using the SRIM 2013 software (http://srim.org/) incorporating the

Kinchin-Pease model for ion-atom displacement and using a 40 eV atom displacement threshold energy with 0 eV lattice binding energy [18]. A cross section plane, perpendicular to the ion implanted surface, was then prepared with a slow-speed diamond saw followed by mechanically polishing as described in Section 5.2.1.

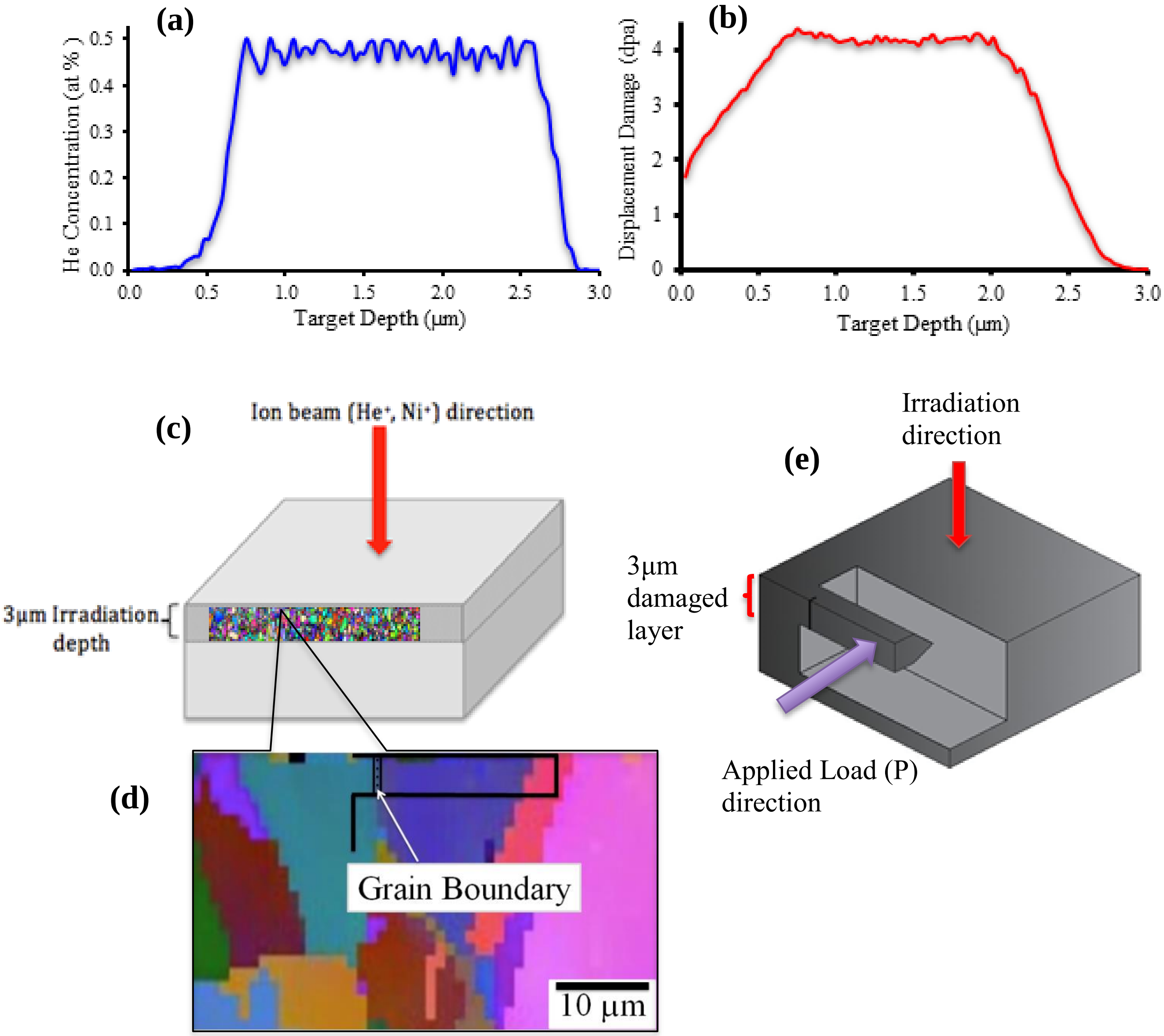

Figure 5.1: SRIM Calculated ion trajectory in Inconel X750 for: (a) Helium concentration profile for 5000appm and (b) Ni$^+$ ions damage profile for 1 dpa. (c) Schematic illustration of the irradiation direction and EBSD grain orientation map. (d) EBSD grain orientation map with the location of a micro-beam containing an indexed grain boundary. (e) Fabrication site of a notched cantilever micro-beam in relation to ion implanted surface of the tests sample.

5.2.3 Grain boundary characterization

Electron backscatter diffraction was used to index the grains on the polished surfaces of the non-implanted and the ion-implanted samples. A surface area of 1.2mm x 0.2 mm was analyzed on each sample using 3 µm analysis step size (Figure 5.1, c-d). From the EBSD data, the orientation of each grain was obtained in terms of Euler angles that were then converted to obtain the rotation matrix, $\mathbf{g_i}$**,** for each grain using Eq. 2-7. This allows for the determination of the misorientation rotation matrix, M_{ij}, between each grain and its neighbor (Eq. 2-8). The grain boundary misorientation angle (θ) along with the associated axis (UVW) of the rotation were then calculated using Eqs. 2-9 and 2-10.

Grain boundaries with θ =10º, 33º, 46º and 57º were selected from each sample. It should be noted that boundaries displaying θ =57º correspond to special Σ3 Coincident Site Lattice (CSL) boundaries. Only grain boundaries which were perpendicular to both the two perpendicular polished surfaces (Figure 5.1-d) were selected for fabrication of notched cantilever micro-beams.

5.2.4 Notched micro-beam fabrication

Focused ion beam milling was used to fabricate pentagonal cross-section notched cantilever micro-beams from the irradiated edge of the samples. The beams were milled such that the notch was made along a single grain boundary, orientated perpendicular to the two polished surfaces of the beam and located approximately 2 µm from the fixed end of the beam (Figure 5.1, d-e). The stages of the micro-beam fabrication were as follows: First, the shape of the beam was created by milling two parallel trenches, about 10µm deep, 20µm wide and spaced 10µm apart, using a 10 nA Ga^+ beam current. A third 10µm deep trench was then milled at one end to produce a beam of about 27µm length. These cuts formed the rough outline of the beam. Next, the trenches were re-milled using a lower, 1 nA, beam current to ensure that the sides were perfectly straight, and the bulk of the Ga^+-implanted metal was removed. The sample was then tilted 45° around the axial direction of the beam and further trenches were cut to complete the pentagonal cross-section. The minimum dimension of these micro-beams thickness was about 5μm and thus was sufficiently large that the measured mechanical properties are not significantly affected by length-scale dependence [20,21].

Finally, the micro-beams were notched along the grain boundary using a 50 pA Ga^+ beam current. The average depth of the notch was about 1.5 μm. Figure 5.2 depicts a finished micro-beam. Twelve notched cantilever micro-beams, four from each sample, were fabricated (Table 5-1).

Table 5-1: Grain boundary misorientation angle, coincident site lattice number (Σ), yield stress σ_y and estimated grain boundary energy γ_{GB} corresponding to each notched cantilever micro-beam tested.

Sample Condition	Beam ID	Angle (°)	$\sum$	σ_y (GPa)	γ_{GB} (J/m^2)
Non-Irradiated	1	10.5	1	0.86	0.8
	2	33.1	-	Failed micro-beam	
	3	46.2	-	0.68	1.15
	4	57.3	3	1	0.65
He^+ -5000appm	1	10.3	1	1.2	0.8
	2	33.4	-	1	1.3
	3	46.6	-	1.12	1.15
	4	57.5	3	1.4	0.65
Ni^+ -1dpa	1	10.1	1	0.92	0.8
	2	33.4	-	0.72	1.3
	3	46.1	-	0.8	1.15
	4	57.8	3	1.11	0.65

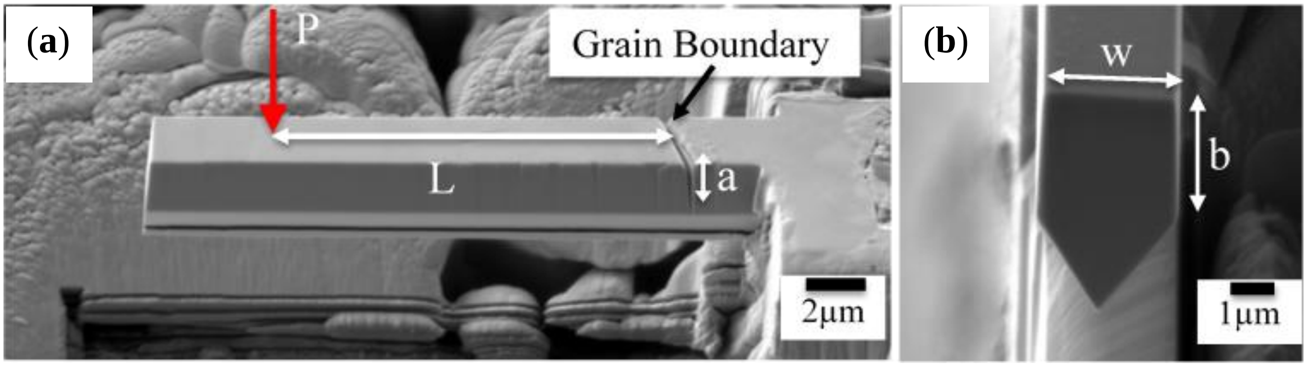

Figure 5.2: (a) SEM micrograph of a finished notched cantilever micro-beam. (b) Pentagonal cross section of the micro-beam.

5.2.5 Micro-beam testing

The cantilever micro-beams were tested in bending at 25°C using a Nano indentation-testing platform, made by Micro-Materials Ltd (Wrexham, UK), fitted with a 10 μm diameter flat-tip diamond indenter. An optical microscope, attached to the nano-indenter, was used to position the beam directly beneath the indenter. A vertical force P was then applied to the top surface of the beam at a distance L from the notched grain boundary (Figure 5.2-a). The micro-beams were tested at a loading rate of 0.05 mN/s while the load-line beam deflection δ was continuously recorded. SEM was used before and after each test to measure the cantilever dimensions, identify the exact position of the applied load, check if grain boundary cracking occurred during loading, and record the degree of dislocation slip steps generated in the region of the notched grain boundary.

Using elastic beam theory for a pentagonal cross-section cantilever beam, the elastic beam compliance S and normal stress $\sigma(y)$ were calculated as:

$$S = \frac{\delta}{P} = \frac{L^3}{3EI} \tag{5-1}$$

$$\sigma(y) = \frac{PLy}{I} \tag{5-2}$$

where δ is the cantilever displacement at the loading point, P is the applied bending load, L is the distance between the notch and the loading point, E is Young's modulus, I is the moment of inertia, and y is the distance from the neutral axis. For pentagonal cross-section beams, I and y were calculated similar to Di Maio [22]:

$$I = \frac{wb^3}{12} + \left(y - \frac{b}{2}\right)^2 bw + \frac{w^4}{288} + \left[\frac{b}{6} + (b - y)\right]^2 \frac{w^2}{4} \tag{5-3}$$

$$y = \frac{\frac{b^2w}{2} + \frac{w^2}{4}\left(b + \frac{w}{6}\right)}{bw + \frac{w^2}{4}} \tag{5-4}$$

where ***w*** and ***b*** are the micro-beam width and depth (Figure 5.2- b). It should be noted that the above equations apply to an un-notched cantilever beam. These equations were modified to include a notch of depth "a".

5.3 Results and discussion

5.3.1 Grain boundary analysis

Figure 5.3, a-b depict the typical variation in angular grain boundary misorientation typical of the Inconel X750 samples in this study. Figure 5.3-c shows a histogram of the calculated grain boundary misorientation angle obtained from this sample. About 53% of the measured grain boundaries are low angle, less than 10^o, or special $\Sigma 3$ CSL (57^o) boundaries. The remaining boundaries are high angle boundaries with angular misorientation ranging up to about 60^o. Table 5-1 lists the calculated misorientation angle of the adjoining grains of the twelve grain boundaries from which notched micro-beams were fabricated.

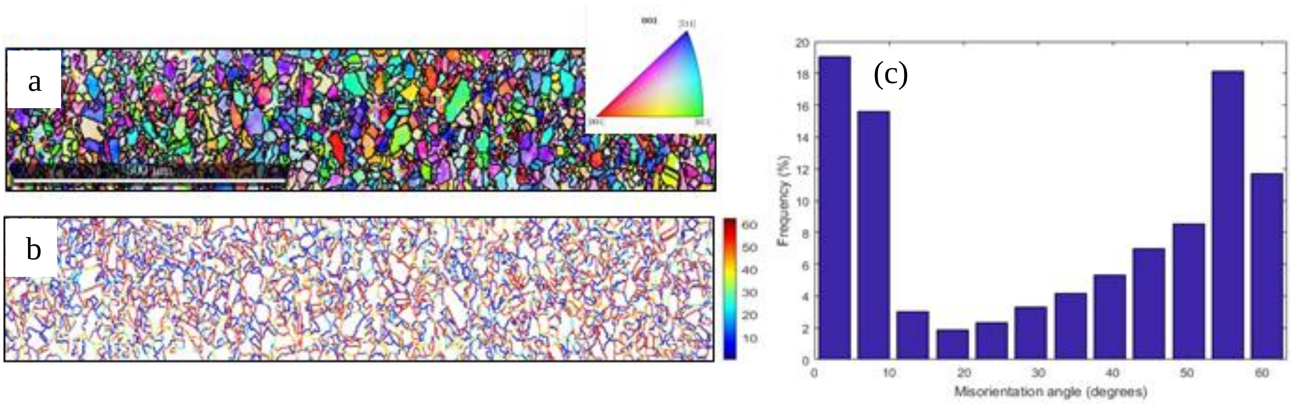

Figure 5.3: (a)EBSD orientation map for a typical heat treated Inconel X750 sample. The axes of the pole figure correspond to the orthogonal axes of the sample. (b) Map of the angular misorientation of the grain boundaries of the sample. (c) Histogram of the misorientation angle distribution for a typical Inconel X750 sample.

5.3.2 Plastic deformation of the micro-cantilever beams

Load versus load-line displacement curves of the non-implanted, He^+- and Ni^+- implanted micro-beams are shown in Figure 5.4, a-c. The load-displacement (P-δ) response, in all cases, displayed an initial linear elastic region followed by yielding and non-linear plastic deformation. Upon unloading the P-δ curve followed a similarly sloped linear response as during the initial elastic loading. Post-test SEM indicate that initial plastic deformation involved the formation of slip bands extending from the plane of the notched grain boundary to a nearby free surface (Figure 5.5). The plastic region of the Load-Displacement curve displays a serrated shape typical of plastic strain bursts occurring during load-controlled deformation [23]. These bursts indicate that initial plastic deformation occurs, in the region of the notched grain boundary, by the nucleation and motion of discrete dislocations or groups of dislocations. Such plastic deformation is characteristic of single crystalline slip as observed in nickel and many FCC micro- and nano-scale samples [23-26]. Previous studies have reported that the plastic strain displacement burst length depends upon the size and the ion-implantation state of the tested specimen with the bursts appearing to be finer and more frequent for ion-implanted specimens [23,27]. Our data support this qualitative observation in that the P-δ curves of the non-implanted notched micro-beams appear to be more serrated than those of the ion-implanted micro-beams (Figure 5.4).

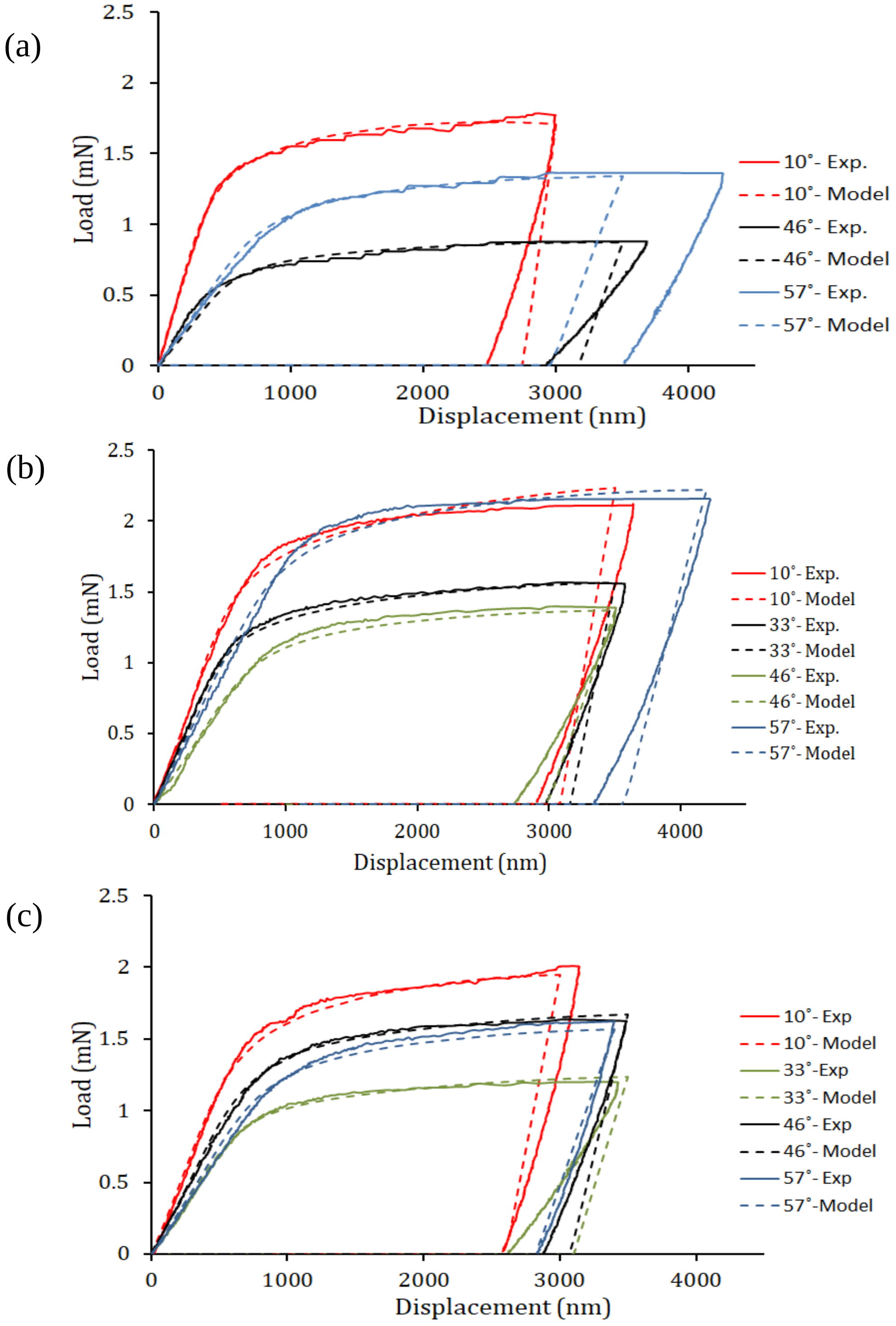

Figure 5.4: Experimental and modeling load displacement response for (a) non-Irradiated CLs, (b) He$^+$ Irradiated CLs, (c) Ni$^+$ Irradiated CLs.

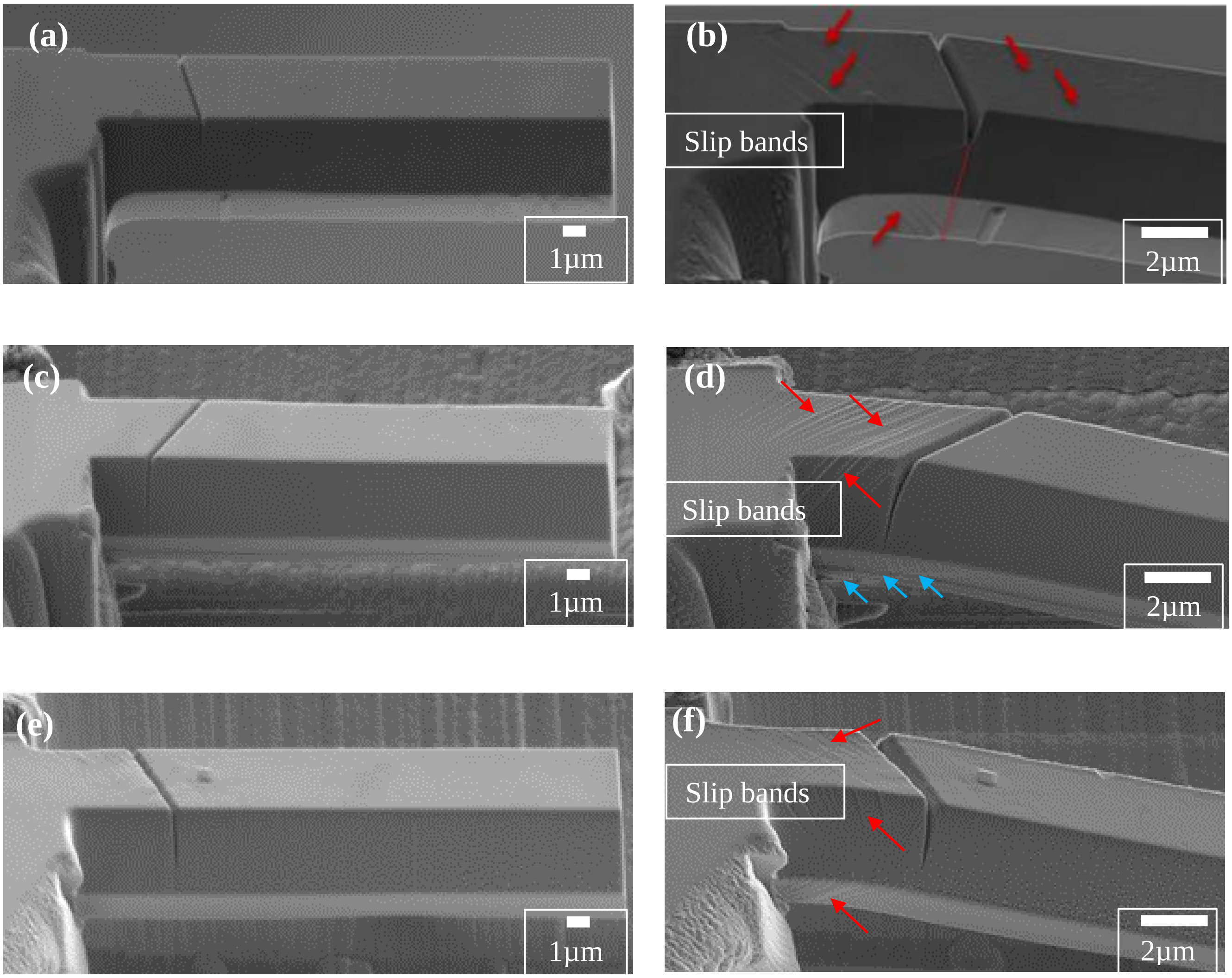

Figure 5.5: (a,b)non-irradiated notched cantilever micro-beam before and after testing,(c,d) Ni$^+$ irradiated notched cantilever micro-beam before and after test, (e,f) He$^+$ irradiated notched cantilever micro-beam before and after test. Arrows indicate the slip bands.

5.3.3 Effect of angular misorientation on grain boundary yield strength

The maximum normal stress on the plane of the notched grain boundary corresponding to the onset of yielding as identifies by the linear – non-linear transition of the P-δ curves was calculated using Eq. 5-2 and is referred to as $\sigma_{y_{GB}}$. A complex dependence of σ_y upon grain boundary misorientation angle is displayed by the test material in all implantation conditions (Figure 5.6). The magnitude of σ_y displayed by the non-implanted Inconel X750 micro-beams is similar in magnitude to previously reported values from tensile tests performed on alloys of similar composition [28,29]. For any misorientation angle, σ_y is higher for the ion-implanted than the non-implanted material. In particular, σ_y of the 5000 appm He^+ implanted material is consistently higher than that of the 1 dpa Ni^+ implanted material.

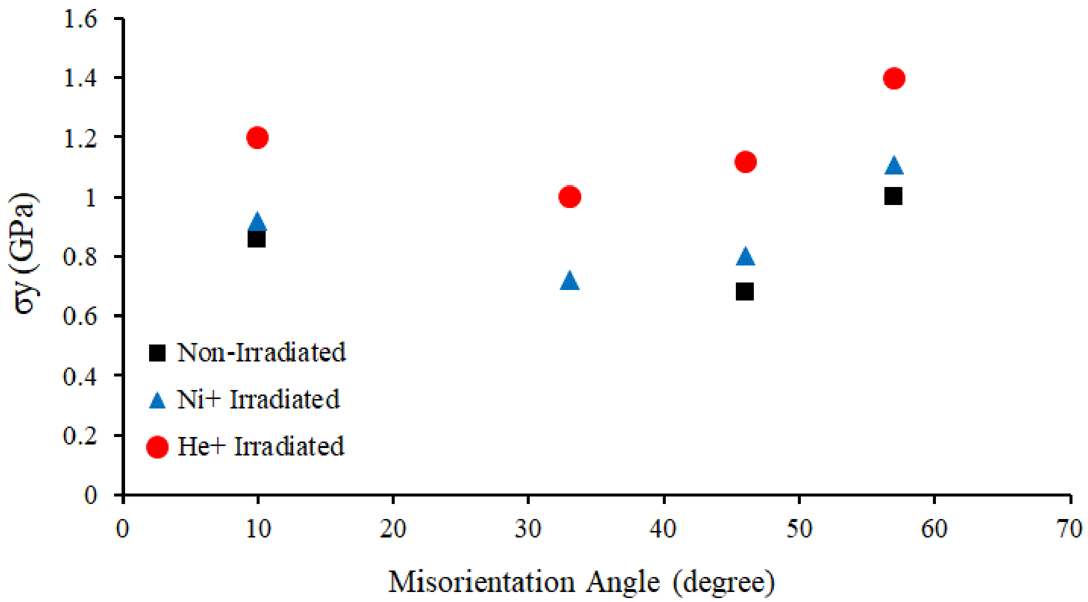

Figure 5.6: Measured yield stress as a function of grain boundary misorientation angle for heat treated Inconel X750 in all irradiation condition.

It is intuitively reasonable that the yield stress of a grain boundary is dependent upon the boundary energy. Olmsted et al [30] computed the energy of pure Ni grain boundaries and noted that while it is generally proportional to the misorientation angle of the boundary, and increases with increasing angle up to about 40º, it is particularly low for low angle boundaries and special high angle boundaries that correspond to low Σ CSL boundaries. Skidmore et al [31] reported similar results from experiments using thermal groove measurements performed on polycrystalline Inconel 600. The grain boundary energy that corresponds to the misorientation angle tested in this study were obtained directly from reference [30]. Figure 5.7 shows a plot of σ_y versus estimated grain boundary energy and depicts a continuously decreasing σ_y with increasing grain boundary energy. The fact that σ_y follow a continuous trend in Figure 5.7 rather than the scattered dependence shown in Figure 5.6 suggests that the grain boundary strength of the heat-treated Inconel X750 alloy, in all conditions tested, is related to the grain boundary energy and decreases as the energy increases. This relationship is intuitively correct since higher grain boundary energy motivates increased diffusion of crystal defects and impurity atoms, in our case helium atoms, to the grain boundary and thus weaken the boundary.

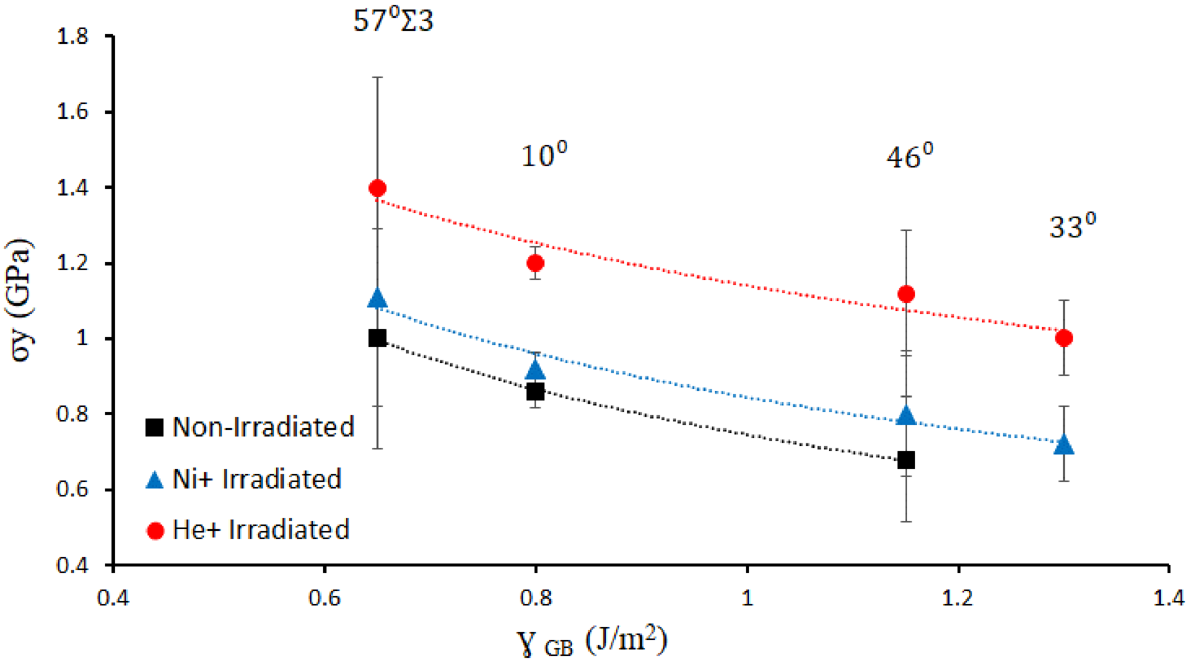

Figure 5.7: Measured grain boundary yield stress as a function of grain boundary energy for all misorientation angles.

Our results described above and shown in Figure 5.7, are in good agreement with those reported by others. Monzen et al [9] studied the effect of misorientation angle on the fracture stress in tensile loaded Cu–2.0 wt.% Sb bicrystals and reported that high angle boundaries fractured more easily than low Σ and low angle grain boundaries and this was attributed to increased segregation of Sb to the high energy boundaries. Armstrong et al

[17] reported similar finding when performing bending tests of notched cantilever micro-beam of Bi embrittled Cu where the beams fractured at low load because of Bi segregation to the high angle boundaries.

Both ion-induced crystal defects and implanted dissimilar ions, such as helium in the case of our study, will most likely affect the grain boundary energy. While direct calculation or atomistic simulation of the effect of crystal defects on the energy of a grain boundary has, to our knowledge, not been reported studies have been made of the effect of dissimilar segregant atoms on the energy and strength of Cu grain boundaries [32]. It was found that while the grain boundary energy decreased as a result of the segregation of dissimilar atoms to the boundary, the strength of the boundary was highly dependent upon the specific segregant atom; atoms such as C and B strengthened while He, H, and P weakened the Cu grain boundary [32,33]. Watanabe et al [13] evaluated the effect of grain boundary sink efficiency on radiation induced segregation in an Fe-Cr-Ni alloy after electron irradiation and found that the sink strength is much stronger in high angle grain boundaries compared to low angle and low Σ boundaries.

With these conflicting factors in mind, we report in the next section an analysis of our experimental data (Figure 5.7) that interprets the effect of both ion-induced crystal damage and accumulated helium on the strength of Inconel X750 grain boundaries of various misorientation angle in terms of their associated crystal defect size and density.

5.3.4 Effect of implanted He^+ and Ni^+ on grain boundary yield strength

Although all three sets of cantilevers notched micro-beams follow the same trend of decreasing σ_y with increasing grain boundary energy, He^+ (5000 appm) implanted beams displayed higher σ_y than the Ni^+ (1dpa) implanted beams. This is an indication of the effectiveness of helium cavities/bubbles accumulated at a grain boundary in strengthening the boundary. The increase in the grain boundary yield strength can be interpreted in terms of a dispersed barrier hardening model [25] which predicts that the incremental flow stress $\Delta\sigma y$ resulting from a periodic array of obstacles to dislocation glide as:

$$\Delta\sigma y = \alpha M\mu b\sqrt{\rho_d\, d} \qquad (5\text{-}5)$$

where α is the obstacle strength factor (α_{Ni} = 0.2 for weak obstacles [25]), M is the Tyler factor (M_{Ni} =3.07 [34]), μ is the shear modulus (μ=76.5GPa for Inconel X750 [35]), b is Burgers vector (b=0.249nm for Ni [25]), ρ_d is the mean defect density and d is the mean defect size. It is clear from the above equation that $\Delta\sigma_y$ is influenced by both the size and the density of defects. However, the grain boundary misorientation angle effect is not considered. Therefore, in the analysis of our data (Table 5-1) we calculate the average grain boundary yield stress $\bar{\sigma}_y$ for all micro-beams in each implantation condition and use these data to determine, from Equation (5-5), that the average $\rho_d\ d$ equals $1.22\text{x}10^{13}\ m^{-2}$ and $8.14\text{x}10^{14}\ m^{-2}$ for the Ni^+ (1 dpa) and the He^+ (5000 appm) implanted samples.

To put these values of $\rho_d d$ into perspective we can refer to previously reported assessments of ρ_d and d for Ni-based alloys exposed to either Kr^{2+} or He^+ ion implantation. Zhang et al [2] performed Kr^{2+} implantations, to levels of 2.7 dpa at 60°C, on heat treated Inconel X750 and reported generation of small dislocation loop and stacking fault tetrahedra of measured number density $\rho_d = 5\text{x}10^{22}\ m^{-3}$ and average size (d_{ave}= 1.3 nm) distributed throughout the grains. The resulting value of $\rho_d d = 6.5\text{x}10^{13}\ m^{-2}$ is similar in magnitude to the value $\rho_d d = 1.22\text{x}10^{13}\ m^{-2}$ that we have calculated for our 1 dpa Ni^+ implanted Inconel X750. The difference between these two values can be attributed to the different level of implantation damage, 2.7 dpa compared to 1 dpa, and to the fact that our values of $\rho_d d$ are determined, by applying the measured grain boundary yield stress (in Eq. 5-5), and thus, correspond to the state of the defects at the grain boundary rather than in the interior of the grains.

Knap et al [3] implanted pure nickel with 10000 appm He^+ at room temperature, and determined that the resulting helium bubbles had a number density of about $\rho_d = 6.3\text{x}10^{24}$

m^{-3} and an average size of about $d = 1.1\ nm$. This results in $\rho_d d = 6.93\text{x}10^{15}\ m^{-2}$. This value is, again, similar in magnitude to the $\rho_d d = 8.14\text{x}10^{14}\ m^{-2}$ that we calculated for the 5000 appm He^+ implanted Inconel X750 samples in our study with the difference attributed to differences in the accumulated helium concentration and the implanted material of the two studies. These findings reveal two facts: (a) the density and/or size of the helium bubbles/cavities produced from 5000 appm He^+ implantation at 25°C is significantly higher than what is produced by 1 dpa crystal damage associated with self-similar Ni^+ implanted at 25°C. (b) Since $\bar{\sigma}_y$ measured in this study reflects grain boundary strength, the helium bubbles accumulate with higher population in grain boundaries than do the Ni^+ irradiation-induced defects.

The findings described above also support previous studies, performed by micro compression, which report that radiation-induced defects can be removed during the plastic deformation, through interaction with mobile dislocations whereas helium bubbles keep their character when interacting with dislocations and thus represent more effective obstacles to dislocation glide and thus increased $\Delta\sigma y$ [36,38].

5.3.5 Effect of grain boundary orientation and ion implantation on the elastic modulus

Elastic modulus calculated using Eq. 5-1 from the loading and unloading linear portions of the load – deflection curves from each cantilever micro-beam bending test are listed in Table 5-2. The elastic modulus derived from the loading portion of the curves was lower than that from the unloading portion. This is likely due to the effect of the indenter penetrating the surface of the cantilever during the loading stage [39]. The difference in the elastic modulus between notched micro-beams with differently oriented grain boundaries is likely due to the elastic anisotropy of nickel and nickel-based alloys such as Inconel X750. The anisotropic elastic modulus of pure nickel is $E_{(111)}$ = 303 GPa and $E_{(100)}$=128GPa [23] while for a nickel-based superalloy $E_{(100)}$= 156GPa and $E_{(110)}$= 225GPa [40] . The average elastic modulus measured from all tested micro-cantilever beams is equal to 208GPa which is very close to the bulk value of 213GPa [35,41].

No change in the elastic modulus was observed due to He^+ or Ni^+ ion implantation. This observation is similar to what was previously reported for non-implanted and Fe^+ implanted Fe12%Cr micro-beams [27].

Table 5-2: Elastic modulus for each notched cantilever micro-beam tested.

Sample Condition	Beam ID	Angle (degree)	Average E-Loading (GPa)	Average E-Unloading (GPa)	Difference (%)
Non-Irradiated	1	10	177.91	187.415	5
	2	33	failed beam	failed beam	failed beam
	3	46	188.045	194.285	3
	4	57	202.5	214.85	6
He^+-5000appm	1	10	221.355	233.36	5
	2	33	207.395	219.7	6
	3	46	189.96	198.76	5
	4	57	217.73	221.335	2
Ni^+-1 dpa	1	10	209.71	213.86	2
	2	33	180.55	187.59	4
	3	46	204.35	216.6	6
	4	57	208.515	215.165	3

5.3.6 Modelling the deformation of the notched micro-beams

The stress analysis performed above does not account for local multi-axial stress concentration in the vicinity of the notch. A three-dimensional elastic/plastic finite element model was therefore constructed of the notched micro-beam to determine the magnitude of the Von-Mises equivalent stress in the region of the notch (Figure 5.8). The model was of the same geometry and loading arrangement as the experimental micro-beams and incorporated isotropic elastic properties (E = 213 GPa [41], ν= 0.29 [35]) along with isotropic power-law strain hardening typical of bulk heat treated Inconel X750 [29]. The effect of on the material response was incorporated by adjusting the equivalent power-law strain hardening to reflect the increase in yield strength as calculated from pyramidal indentation hardness measurements ($\sigma_y = H/3$) performed Ni^+ and He^+ implanted Inconel X750. The resulting load-displacement response obtained from the finite element simulation closely matched the experimentally obtained P-δ response curves for the non-implanted and the ion-implanted samples (Figure 5.4, a-c). As expected, at the very beginning of the bending test, the local Von Mises equivalent stress was of highest value at the crack tip (Figure 5.8). Figure 5.9 shows a plot of maximum local von-Mises equivalent tensile stress on the grain boundary at the notch tip, $\sigma_{y_{GB_{VM}}}$ at the point of yielding as a function of grain boundary energy. This plot depicts a continuously decreasing $\sigma_{y_{GB_{VM}}}$ with increasing grain boundary energy and indicates most clearly how the grain boundary yield strength is affected by grain boundary energy, implantation-induced crystal damage and accumulated helium.

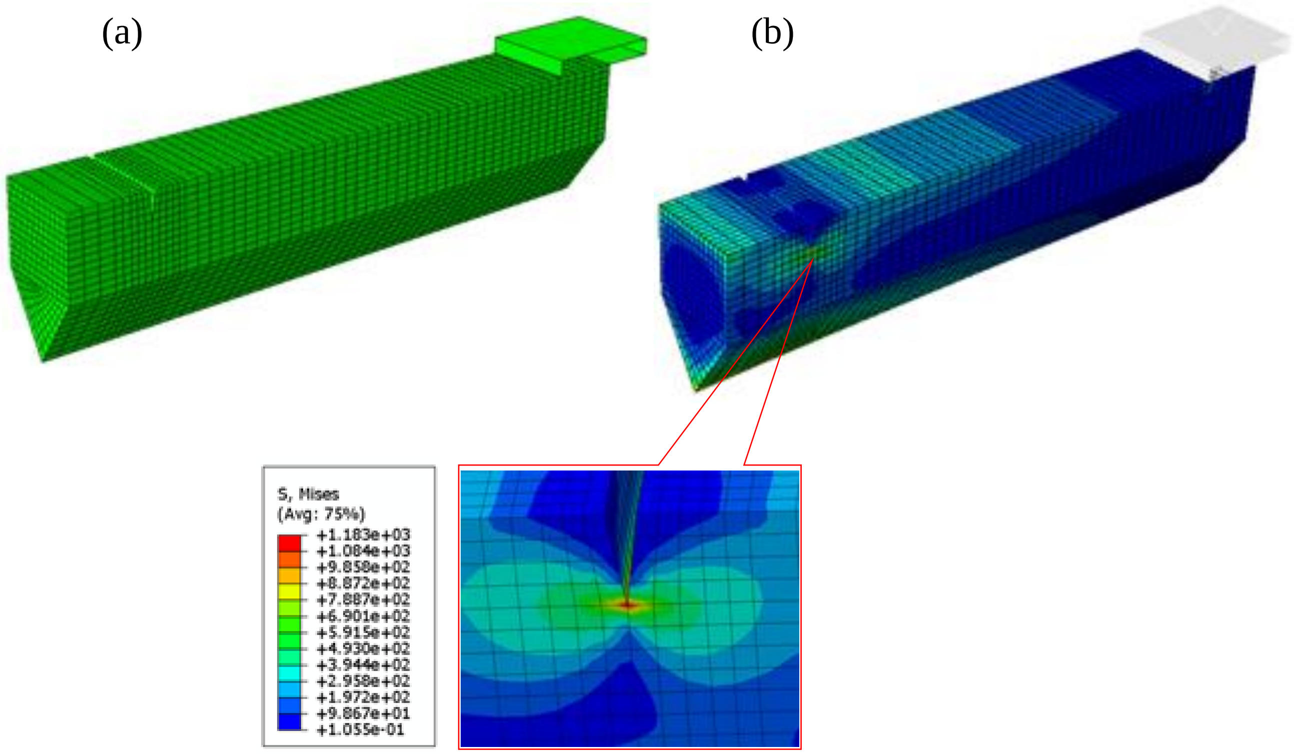

Figure 5.8: (a) Finite element model for the tested notched cantilever micro-beam. (b) Deformed model with the Von Mises equivalent stress concentrated at the notch tip.

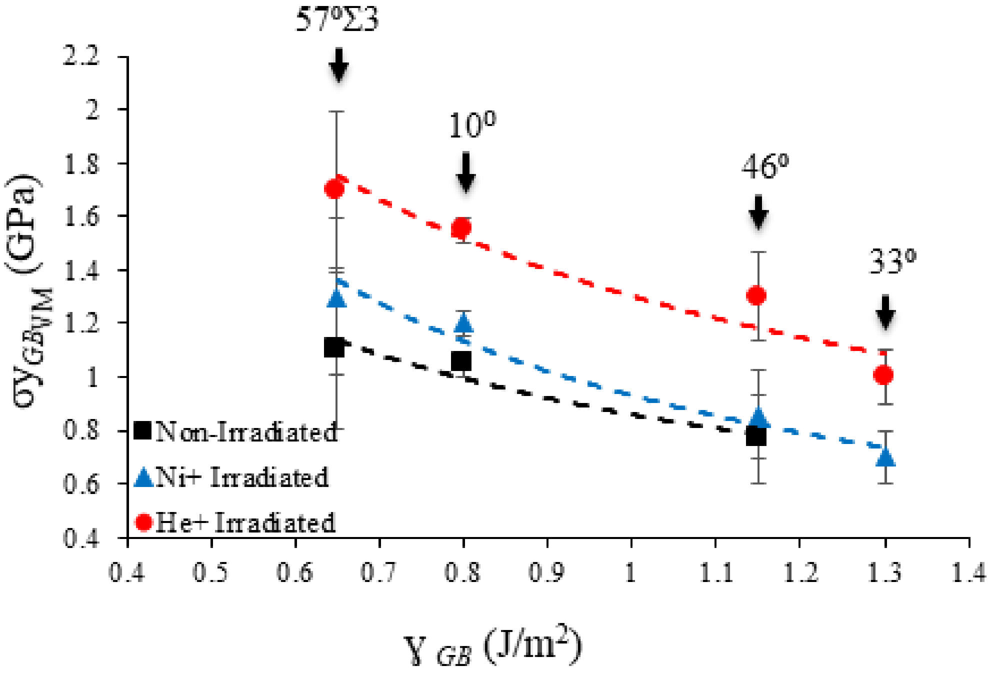

Figure 5.9: Local Von-Mises equivalent notch-tip grain boundary tensile stress corresponding to initiation of plastic yielding as a function of grain boundary energy for all misorientation angles.

5.4 Conclusion

The purpose of this study was to use notched cantilever micro-beam bending to determine experimentally the effect of the misorientation angle on the yield strength of an Inconel X750 grain boundary when subjected to irradiation-induced crystallographic damage and accumulated helium.

Whereas the local grain boundary yield stress follows a complex nonlinear dependence upon grain boundary misorientation angle up to about 60°, it shows a simpler continuous decreasing dependence upon grain boundary energy. This suggests that the grain boundary strength of the heat treated Inconel X750 alloy, in all conditions tested, is related to the grain boundary energy and decreases as the energy increases.

Both Ni^+ and He^+ ion implantation increased the local grain boundary yield stress over the complete range of boundary misorientation investigated. We attribute this to the strengthening effect resulting from segregation of ion-induced crystal defects and helium bubbles/cavities to the grain boundaries. Our data suggest that the strengthening effect from 5000 appm He^+, implanted at 25°C, is significantly higher than what is produced by 1 dpa crystal damage associated with Ni^+ implantation at 25°C. Analysis of these findings in terms of a dispersed barrier hardening model illustrate that accumulated helium is more effective than irradiation-induced crystal defects, such as stacking faults tetrahedra and small dislocation loops, at preventing dislocation nucleation and/or movement from grain boundaries in the heat treated Inconel X750 alloy.

To our knowledge, this study has presented the first quantitative assessment of the effect of angular misorientation on the grain boundary yield strength of ion-implanted heat-treated Inconel X750. Our findings provide important new insights on the effects of neutron irradiation exposure on the mechanical properties of grain boundaries in this alloy and point to necessary further characterization of grain boundary yield stress over the complete range of ion-induced crystal damage (dpa) and accumulated (appm) helium concentration.

5.5 Acknowledgment

The authors wish to acknowledge the assistance of Mr. Jack Hendriks at the Tandetron Ion Accelerator facilities at the University of Western Ontario (London, Ontario, Canada) for his support with performing ion implantations of the Inconel X750 samples. The assistance of Dr. Ariful Islam for his support in constructing the finite element model of the cantilever micro-beam is also acknowledged. The authors also gratefully acknowledge financial funding of the Natural Science and Engineering Research Council (NSERC) and University Network of Excellence in Nuclear Engineering (UNENE) for funding this study. M.N.T. acknowledges the financial support of the government of the province of Ontario, Canada through an Ontario Graduate Scholarship.

5.6 References

[1] M. Griffiths, “The Effect of Irradiatoin on Ni-containing Components in CANDU Reactor Cores: A Review,” *AECL Nucl. Rev.*, vol. 2, no. 1, pp. 1–16, 2013.

[2] H. K. Zhang, Z. Yao, C. Judge, and M. Griffiths, “Microstructural evolution of CANDU spacer material Inconel X-750 under in situ ion irradiation,” *J. Nucl. Mater.*, vol. 443, no. 1–3, pp. 49–58, 2013.

[3] J. A. Knapp, D. M. Follstaedt, and S. M. Myers, “Hardening by bubbles in He-implanted Ni,” *J. Appl. Phys.*, vol. 103, no. 1, 2008.

[4] C. D. Judge *et al.*, “Intergranular fracture in irradiated Inconel X-750 containing very high concentrations of helium and hydrogen,” *J. Nucl. Mater.*, vol. 457, pp. 165–172, 2015.

[5] M. D. Sangid, H. Sehitoglu, H. J. Maier, and T. Niendorf, “Grain boundary characterization and energetics of superalloys,” *Mater. Sci. Eng. A*, vol. 527, no. 26, pp. 7115–7125, 2010.

[6] C. Lim, “Cracking Large Strain Fatigue,” vol. 35, no. 7, pp. 1653–1662, 1987.

[7] Y. Pan, B. L. Adams, T. Olson, and N. Panayotou, “Grain-boundary structure effects on intergranular stress corrosion cracking of Alloy X-750,” *Acta Mater.*, vol. 44, no. 12, pp. 4685–4695, 1996.

[8] S. Kobayashi, T. Maruyama, S. Saito, S. Tsurekawa, and T. Watanabe, “In situ observations of crack propagation and role of grain boundary microstructure in nickel embrittled by sulfur,” *J. Mater. Sci.*, vol. 49, no. 11, pp. 4007–4017, 2014.

[9] R. Monzen, O. Matsuda, and H. Miura, “Misorientation dependence of intergranular embrittlement of Cu-2.0 wt.% Sb bicrystals,” *Mater. Sci. Eng. A*, vol. 387–389, no. 1-2 SPEC. ISS., pp. 424–427, 2004.

[10] P. Lejček, *Grain Boundary Segregation in Metals*. 2010.

[11] C. M. Barr *et al.*, “Grain boundary character dependence of radiation-induced segregation in a model Ni-Cr alloy,” *J. Mater. Res.*, vol. 30, no. 9, pp. 1290–1299, 2015.

[12] A. F. Rowcliffe, L. K. Mansur, D. T. Hoelzer, and R. K. Nanstad, “Perspectives on radiation effects in nickel-base alloys for applications in advanced reactors,” *J. Nucl. Mater.*, vol. 392, no. 2, pp. 341–352, 2009.

[13] S. Watanabe, Y. Takamatsu, N. Sakaguchi, and H. Takahashi, “Sink effect of grain boundary on radiation-induced segregation in austenitic stainless steel,” *J. Nucl.*

Mater., vol. 287, pp. 152–156, 2000.

[14] J. J. Kai, F. R. Chen, and T. S. Duh, "Effects of Grain Boundary Misorientation on Radiation-Induced Solute Segregation in Proton Irradiated 304 Stainless Steels," *Materials Transactions*, vol. 45, no. 1. pp. 40–50, 2004.

[15] M. Tomozawa, Y. Miyahara, and K. Kako, "Solute segregation on σ3 and random grain boundaries in type 316L stainless steel," *Materials Science and Engineering A*, vol. 578. pp. 167–173, 2013.

[16] W. Z. Han, M. J. Demkowicz, E. G. Fu, Y. Q. Wang, and A. Misra, "Effect of grain boundary character on sink efficiency," *Acta Mater.*, vol. 60, pp. 6341–6351, 2012.

[17] D. E. J. Armstrong, A. J. Wilkinson, and S. G. Roberts, "Micro-mechanical measurements of fracture toughness of bismuth embrittled copper grain boundaries," *Philos. Mag. Lett.*, vol. 91, no. 6, pp. 394–400, 2011.

[18] R. E. Stoller, M. B. Toloczko, G. S. Was, A. G. Certain, S. Dwaraknath, and F. A. Garner, "On the use of SRIM for computing radiation damage exposure," *Nucl. Instruments Methods Phys. Res. Sect. B*, vol. 310, pp. 75–80, 2013.

[19] O. Engler and V. Randle, *Introduction to Texture Analysis*. 2010.

[20] C. Motz, T. Schöberl, and R. Pippan, "Mechanical properties of micro-sized copper bending beams machined by the focused ion beam technique," *Acta Mater.*, vol. 53, no. 15, pp. 4269–4279, 2005.

[21] E. Husser and S. Bargmann, "The role of geometrically necessary dislocations in cantilever beam bending experiments of single crystals," *Materials (Basel).*, vol. 10, no. 3, pp. 1–24, 2017.

[22] D. Di Maio and S. G. Roberts, "Measuring fracture toughness of coatings using focused-ion-beam-machined microbeams," *J. Mater. Res.*, vol. 20, no. 2, pp. 299–302, 2005.

[23] C. P. Frick, B. G. Clark, S. Orso, A. S. Schneider, and E. Arzt, "Size effect on strength and strain hardening of small-scale [1 1 1] nickel compression pillars," *Mater. Sci. Eng. A*, vol. 489, no. 1–2, pp. 319–329, 2008.

[24] F. F. Csikor *et al.*, "Dislocation Avalanches , Strain Bursts , and the Problem of Plastic Forming at the Micrometer Scale Linked references are available on JSTOR for this article : Dislocation Avalanches , Strain Bursts , and the Problem of Plastic Forming at the Micrometer S," vol. 318, no. 5848, pp. 251–254, 2018.

[25] X. Zhao *et al.*, "In situ measurements of a homogeneous to heterogeneous transition in the plastic response of ion-irradiated 〈111〉 Ni microspecimens," *Acta Materialia*, vol. 88. pp. 121–135, 2015.

[26] A. Stratulat, D. E. J. Armstrong, and S. G. Roberts, "micro mechanical measurment of fracture behaviour of individual grain boundaries in Bi alloy 600 exposed to a pressurized water reactor enviroment," *Corros. Sci.*, vol. 104, pp. 9–16, 2016.

[27] D. E. J. Armstrong, C. D. Hardie, J. S. K. L. Gibson, A. J. Bushby, P. D. Edmondson, and S. G. Roberts, "Small-scale characterisation of irradiated nuclear materials: Part II nanoindentation and micro-cantilever testing of ion irradiated nuclear materials," *J. Nucl. Mater.*, vol. 462, pp. 374–381, 2015.

[28] W. J. Mills, "The deformation and fracture characteristics of inconel X-750 at room temperature and elevated temperatures," *Metall. Trans. A*, vol. 11, no. 6, pp. 1039–1047, 1980.

[29] C. Marsh and D. Kaoumi, "Serrated tensile flow in inconel X750 sheets: Effect of heat treatment," *Mater. Sci. Eng. A*, vol. 707, no. May, pp. 136–147, 2017.

[30] D. L. Olmsted, S. M. Foiles, and E. A. Holm, "Survey of computed grain boundary properties in face-centered cubic metals: I. Grain boundary energy," *Acta Mater.*, vol. 57, no. 13, pp. 3694–3703, 2009.

[31] T. Skidmore, R. G. Buchheit, and M. C. Juhas, "Grain boundary energy vs. misorientation in Inconel® 600 alloy as measured by thermal groove and OIM analysis correlation," *Scr. Mater.*, vol. 50, no. 6, pp. 873–877, 2004.

[32] Z. Huang, F. Chen, Q. Shen, L. Zhang, and T. J. Rupert, "Uncovering the influence of common nonmetallic impurities on the stability and strength of a Σ5 (310) grain boundary in Cu," *Acta Materialia*, vol. 148. pp. 110–122, 2018.

[33] M. Rajagopalan, M. A. Tschopp, and K. N. Solanki, "Grain boundary segregation of interstitial and substitutional impurity atoms in alpha-iron," *Jom*, vol. 66, no. 1, pp. 129–138, 2014.

[34] William F. Hosford, *Mechanical behavior of materials*, vol. 12, no. 3. 2009.

[35] Special Metals, "INCONEL Alloy X-750," *Spec. Met.*, pp. 1–28, 2004.

[36] P. Hosemann, "Small-scale mechanical testing on nuclear materials: bridging the experimental length-scale gap," *Scr. Mater.*, vol. 143, pp. 161–168, 2018.

[37] Q. Guo, P. Landau, P. Hosemann, Y. Wang, and J. R. Greer, "Helium implantation

effects on the compressive response of Cu nanopillars," *Small*, vol. 9, no. 5, pp. 691–696, 2013.

[38] D. Kiener, P. Hosemann, S. A. Maloy, and A. M. Minor, "In situ nanocompression testing of irradiated copper," *Nat. Mater.*, vol. 10, no. 8, pp. 608–613, 2011.

[39] D. E. J. Armstrong, A. J. Wilkinson, and S. G. Roberts, "Measuring anisotropy in Young's modulus of copper using microcantilever testing," *J. Mater. Res.*, vol. 24, no. 11, pp. 3268–3276, 2009.

[40] H. Takagi, M. Fujiwara, and K. Kakehi, "Measuring Young's modulus of Ni-based superalloy single crystals at elevated temperatures through microindentation," *Mater. Sci. Eng. A*, vol. 387–389, no. 1-2 SPEC. ISS., pp. 348–351, 2004.

[41] C. D. Judge *et al.*, "The effects of proton irradiation on the microstructural and mechanical property evolution of inconel X-750 with high concentrations of helium," *J. Nucl. Mater.*, vol. 492, pp. 213–226, 2017.

Chapter 6

6 Conclusions and Future Scope

6.1 Conclusions

Inconel X750 garter spring spacer have been studied over the recent years, despite this, extensive experimentally-based knowledge on the mechanisms by which this material undergoes radiation-induced degradation and grain boundary embrittlement when it's in the non-irradiated and the neutron irradiated conditions has not been thoroughly studied. This dissertation has attempted to overcome this scarcity of data by providing a series of fundamental investigations, involving the use of novel micro-beam bending test, nanoindentation test, along with TEM techniques, to understanding the mechanisms led to mechanical property degradation of Inconel X750 CANDU spacer material in the non-irradiated and the Ni^+/He^+ irradiated conditions over the temperature range that is characteristic of the operating temperature window of a spacer in a CANDU nuclear reactor.

In the first study (Chapter 3) Ni^+ and He^+ implantation-induced hardening of HT and SA Inconel X750 was studied using nano-indentation hardness testing along with SEM/TEM microstructural analysis. The X750 in the SA condition showed a systematic hardening as a function of crystal damage ψ. Conversely, the X750 in the HT condition exhibited a softening between ψ = 0.1 and 0.5 dpa. TEM analysis indicated that this softening was associated with disordering and dissolution of the γ' strengthening phase. The hardening behavior observed at higher implantation damage (ψ =1 dpa*)* resulted in re-formation of incoherent Al/Ti rich regions (precipitates) within the microstructure phase.

He^+ implantation resulted in generally increasing hardness with increasing accumulated helium however the heat-treated samples implanted with high helium content (C_{He} = 5000appm) showed a slight decrease in the hardness relative to the H vs C_{He} trend displayed by the other samples. This is attributed to the atomic displacements associated with this He^+ implantation (ψ = 0.012 dpa) being sufficient to disorder the coherent γ' phase.

Therefore, it is concluded that the γ' state in heat-treated Inconel X750 changes as a result of high energy ion implantation and the state, whether ordered, disordered or dissolved, is determined by the level of ψ resulting from the particular ion implantation process. The mechanism by which this occurs is dictated by the mechanism of ion-induced mixing and is strongly dependent upon the localized thermal spike induced by the implantation process.

In the subsequent study (Chapter 4), sequential He^+ and Ni^+ implantations were performed at 25°C and 200°C to investigate their combined effect on the indentation hardness of heat-treated Inconel X750 alloy. The microstructure of the ion-implanted region was also characterized with TEM. At both implantation temperature, the X750 alloy displayed a pronounced softening with very low Ni^+ implantation levels, $\psi = 0.01 - 1.0$ dpa, however it showed a clear increase in hardness when solely implanted with He^+ up to $C_{He} = 5000$ appm. Samples subjected to sequential He^+ and Ni^+ implantations displayed hardness values between those presented by sole He^+ or Ni^+ implantation suggesting that the effects of ion-induced microstructural damage and helium accumulation on the hardness of this alloy can be considered as independent and additive over the range of conditions studied. This observation is in contradiction to previously reported TEM-based studies which suggest that accumulated helium slows the dissolution/disordering of the γ’ hardening phase in this alloy. In present study established theories, considering the anti-phase boundary and coherency strengthening mechanisms, were applied to assess the contribution of ion-induced defect clustering, γ’ precipitate disordering, and helium bubble accumulation to the hardness of the X750 alloy. It was observed that generation of ion-induced defect clusters and the formation of helium bubbles increased the indentation hardness slightly while the disordering of γ’ precipitates resulted in a dramatic decrease in the total hardness. The results of this mathematical approach support the experimental results; that is the Ni^+-induced softening and He^+-induced hardening mechanisms operate independently and are additive. Ni^+ and He^+ implantation also had different effects on the depth dependence of the indentation hardness (ISE). The ISE was pronounced in the samples subjected to only Ni^+ implantation while it was almost absent in samples subjected to only He^+ implantation. Sequential He^+/ Ni^+ implantation shows lower ISE compared to sole Ni^+ implantation and follows more closely the trend displayed by sole He^+. In all conditions, the ISE for samples implanted at 200°C is more evident than for sampled implanted at 25°C. This suggests that slight thermal annealing affects the configuration of ion-induced crystal damage when implantation is performed at 200°C compared to 25°C.

The purpose of this final investigation (Chapter 5) was to provide new insights into understanding the mechanisms led to grain boundary embrittlement in Inconel X-750 due to irradiation. Novel notched cantilever micro-beams made from the heat-treated X750 in the non-implanted, self-similar Ni^+ implanted (1 dpa at 25ºC), and He^+ implanted (5000 appm at 25ºC) conditions was fabricated. The cantilever micro-beams were notched along indexed grain boundaries with different misorientation angles (θ = 10º, 33º, 46º and 57º), and the bending test performed to determine experimentally the effect of the misorientation angle on the yield strength of an Inconel X750 grain boundary when subjected to irradiation-induced crystallographic damage and accumulated helium. Whereas the local grain boundary yield stress follows a complex nonlinear dependence upon grain boundary misorientation angle up to about 60º, it shows a simpler continuous decreasing dependence upon grain boundary energy. Similar results were obtained from a three-dimensional elastic/plastic finite element model which constructed of the notched micro-beam to determine the magnitude of the Von-Mises equivalent stress in the region of the notch. This suggests that the grain boundary strength of the heat-treated Inconel X750 alloy, in all conditions tested, is related to the grain boundary energy and decreases as the energy increases. Both Ni^+ and He^+ ion implantation increased the local grain boundary yield stress over the complete range of boundary misorientation investigated. We attribute this to the strengthening effect resulting from segregation of ion-induced crystal defects and helium bubbles/cavities to the grain boundaries. Our data suggest that the strengthening effect from 5000 appm He^+, implanted at 25˚C, is significantly higher than what is produced by 1 dpa crystal damage associated with Ni^+ implantation at 25˚C. Analysis of these findings in terms of a dispersed barrier hardening model illustrate that accumulated helium is more effective than irradiation-induced crystal defects, such as stacking faults tetrahedra and small dislocation loops, at preventing dislocation nucleation and/or movement from grain boundaries in the heat treated Inconel X750 alloy. To our knowledge, this study has presented the first quantitative assessment of the effect of angular misorientation on the grain boundary yield strength of ion-implanted heat-treated Inconel X750. Our findings provide important new insights on the effects of neutron irradiation exposure on the mechanical properties of grain boundaries in this alloy and point to necessary further characterization of grain boundary yield stress over the complete range of ion-induced crystal damage (dpa) and accumulated (appm) helium concentration.

Although many necessary subjects that lead to better understanding of the irradiation damage on X750 in CANDU reactor was covers in this thesis, there are some limitation in our experimental approach that need to be highlighted; such as simulate the neutron damages and the transmutation reaction's product by using heavy ion irradiation (Ni^+) and He^+ implantation respectively. In addition, we used a finite energy range of ions to simulate irradiation damage, and this energy range is not the same as the neutron energy range in CANDU reactor core. Furthermore, 25 ºC and 200 ºC temperature (for Ni^+ only) was used for ion implantation which is much different than the thermal conditions in a CANDU core.

6.2 Scope for Future Work

The mechanical properties, microstructure, and grain boundary strength of Inconel X-750 implanted by different levels of sole ions (Ni^+, He^+) or sequential implantation of ions (He^+/Ni^+) have been investigated for the first time. As a result, there are many remaining, open ended questions, which warrant continued research to help explain. The work presented in this dissertation is only a small part of a large, ongoing, industrial research program. There are some recommendations which are introduced here as future works:

1. In the current investigation nano-indentation hardness test have been carried at room temperature. For future work, high temperature indentation test, simulating the X750 spacer operating temperature in reactor core (100°C-400°C), can be performed to have a complete understanding on the deformation behavior at higher temperature and their direct effect on the mechanical properties of X750 before and after irradiation.

2. In our study, we used two mechanical testing techniques (nanoindentation and bi-crystal micro-beam bending) to assess the X750 hardness and the yield stress before and after irradiation. In future work, it will be useful to the nuclear research community if a known oriented single crystal micropillars compression test can be used to gain the uniaxial stress state across the whole sample in irradiated and nonirradiated condition with eliminating the orientation effect, since the stress state during indentation testing is complex because of its triaxial nature. This method delivers a stress-strain curve and offer the possibility for in situ observation of the sample deformation, and thus allowing for a direct determination of the deformation mechanisms.

3. Helium injection was achieved at room temperature in the current study, and it was found that high concentration of He^+ (5000appm) was disordering the X750 strengthening phase γ'. High temperature helium implantation (similar to X750 spacer operating temperature) is suggested with higher helium concentration to be performed with TEM examination to have a complete and clear understanding on the effect of sole helium implantation temperature and dose on γ' stability.

4. The segregation of ion-induced crystal defects and helium bubbles/cavities to the grain boundaries and their embrittlement effect with respect to misorientation angle and grain boundary energy was studied in chapter 5. Radiation-induced segregation of chromium (Cr), in addition to significant amount of hydrogen (H) production during transmutation reaction within the X-750 alloy during service into the CANDU reactor, have been reported earlier, which could potentially weaken the grain boundaries and subsequently cause degradation of mechanical properties Therefore, future work may focus on the grain boundary character dependence of radiation-induced segregation of Cr and H in to the grain boundary and their embrittlement effects on X750.

Curriculum Vitae

Name:	Maisaa N. Tawfeeq
Post-secondary Education and Degrees:	University of Technology Baghdad, Iraq 1994-1998 B. Sc. in Mechanical Engineering
	University of Technology Baghdad, Iraq 2002-2005 ME. Sc. in Mechanical Engineering
	The University of Western Ontario London, Ontario, Canada 2014-2019 Ph.D. in Mechanical and Materials Engineering
Honours and Awards:	Western Engineering Scholarship 2014-2018
	Province of Ontario Graduate Scholarship 2016-2017, 2017-2018
	Julie Lassonde Scholarship 2019
Related Work Experience	Teaching Assistant The University of Western Ontario 2014-2018
	Teaching Assistant University of Technology 2002-2003

Publications:

1. Maisaa N. Tawfeeq, Robert J. Klassen, “Effect of ion implantation on the grain boundary strength of heat treated Inconel X750”, Journal of Nuclear Materials, Vol. 516, pp255-263, 2019.

2. Maisaa N. Tawfeeq, Robert J. Klassen,” Effect of sequential helium and nickel ion implantation on the nano-indentation hardness of Inconel X750”, Journal of Nuclear Engineering and Radiation Science (submitted August 2019).

3. Maisaa N. Tawfeeq, Robert J. Klassen “Ion Implantation Effect on the Mechanical Properties of Inconel X750”, Journal of Nuclear Engineering and Radiation Science (submitted August 2019).

Conference Presentations

1. Maisaa N. Tawfeeq, Robert J. Klassen, “Effect of Nickel and Helium Implantation on the Indentation Hardness of Inconel X750”, AccApp ’17, 13th International Topical Meeting on Nuclear Applications of Accelerators, July 31-August 4, 2017- Hilton Québec- Québec City, Québec, Canada.

2. Maisaa N. Tawfeeq, Robert J. Klassen, “Investigation of the Effect of Self-Similar Ion Irradiation and Helium Implantation on the Nano-indentation Hardness of Heat-Treated Inconel X750”, 28th Canadian Materials Science Conference, June7-10, 2016- McMaster University, Hamilton, Ontario, Canada.

Posters

1. Maisaa N. Tawfeeq, Robert J. Klassen, Poster presentation in “The Nuclear Materials Conference, 14-18 October 2018, Seattle, WA, USA” conference.

2. Maisaa N. Tawfeeq, Lobat Kavan, Robert J. Klassen, Poster presentation in “12th CANDU owners Group Fuel Channel Seminar-May 30-31st, 2017-Ajax Convention Centre” conference.

3. Maisaa Tawfeeq, Aria Khalili, Feifei Nai, Robert Klassen, Poster presentation in “UNENE R&d Workshop December 15-16, Toronto, Ontario, Canada” conference.